



A. D. 1308
unipg
DEPARTMENT
OF PHARMACEUTICAL SCIENCES



ugr | Universidad
de **Granada**

UNIVERSITA' DEGLI STUDI DI PERUGIA

A. A. 2022-2023

DOTTORATO DI RICERCA IN *SCIENZE FARMACEUTICHE* CICLO XXXVI
settore scientifico disciplinare CHIM/09

DOCTORATE IN *PHARMACEUTICAL SCIENCES* XXXVI CYCLE
scientific area CHIM/09

**STUDY AND DEVELOPMENT OF BIOADHESIVE
PATCHES FOR WOUND TREATMENT
BY 3D PRINTING**

Carmen Laura Pérez Gutiérrez

SUPERVISORS:

Prof. Luana Perioli

COORDINATOR:

Prof. Oriana Tabarrini

Prof. César Viseras Iborra

Editor: Universidad de Granada. Tesis Doctorales
Autor: Carmen Laura Pérez Gutiérrez
ISBN: 978-84-1195-448-8
URI: <https://hdl.handle.net/10481/95003>



UGR | Universidad
de Granada



A.D. 1308
unipg
DEPARTMENT
OF PHARMACEUTICAL SCIENCES

UNIVERSIDAD DE GRANADA
A. A. 2022-2023

PROGRAMA DE DOCTORADO EN FARMACIA (B15.56.1) EN COTUTELA

Escuela de Doctorado de Ciencias de la Salud

Departamento de Farmacia y Tecnología Farmacéutica

**ESTUDIO Y DESARROLLO DE PARCHES
BIOADHESIVOS IMPRESOS EN 3D PARA EL
TRATAMIENTO DE HERIDAS**

Carmen Laura Pérez Gutiérrez

DIRECTORES DE TESIS:

Prof. Luana Perioli

COORDINADOR:

Prof Oriana Tabarrini

Prof. César Viseras Iborra

Hay almas a las que una tiene ganas de asomarse, como a una ventana llena de sol.

Federico García Lorca

(Fuente Vaqueros, Granada, 5 de junio de 1898)

TABLE OF CONTENTS

Abbreviations and terms	IV
Overview	VI
Resumen	VIII
1. Introduction	1
1.1. Wounds	3
1.1.1. Phases of wound healing process	5
1.1.2. Complications and infections	7
1.1.3. Social and financial impact	9
1.2. Formulations for wound treatment	10
1.3. Techniques for patches production	14
1.3.1. Solvent casting	14
1.3.2. Electrospinning	15
1.3.3. 3D printing	16
1.3.3.1. <i>PAM technique</i>	18
1.3.3.2. <i>FDM technique</i>	19
1.3.3.3. <i>3D printing and personalized medicine</i>	21
1.3.3.4. <i>Regulatory aspects in 3D printing</i>	22
1.3.3.5. <i>3D printing and sustainability</i>	23
1.3.3.6. <i>3D printing technology in Europe</i>	25
2. Objectives	27
3. Pressure Assisted Microsyringe 3D Printing	31
3.1. Pressure Assisted Microsyringe (PAM) 3D Printing	33
3.2. Materials	37
3.3. Methods	38
3.3.1. Hydrogels formulations	38
3.3.2. Rheological measurements	41
3.3.3. Patches preparation	42
3.3.3.1. <i>Selection of printing parameters and design</i>	42
3.3.3.2. <i>Backing layer preparation</i>	44
3.3.4. Patches characterization	45

3.3.5. Biological activity	47
3.4. Results and discussion	50
3.4.1. Rheology of hydrogels	51
3.4.2. Patches preparation	55
3.4.2.1. <i>Selection of printing parameters and digital design</i>	55
3.4.3. Patches characterization	65
3.4.4. Biological properties	79
4. TPS filaments optimization suitable for FDM printing	83
4.1. TPS filaments optimization suitable for FDM printing	85
4.2. Materials	89
4.3. Methods	89
4.3.1. TPS filaments preparation	89
4.3.2. TPS filaments characterization	91
4.3.3. Biological properties	93
4.3.4. Prototypes patches preparation	94
4.3.4.1. <i>Selection of printing parameters and digital design</i>	94
4.4. Results and discussion	97
4.4.1. TPS filaments characterization	98
4.4.2. Biological properties	111
4.4.3. Prototypes patches preparation	114
4.4.3.1. <i>Selection of printing parameters and digital design</i>	114
5. Conclusions	117
5.1. Conclusiones	122
References	125
Acknowledgments	140

Abbreviations and terms

3D Three-dimensional

A

ABS Acrylonitrile Butadiene Styrene

Alg Sodium Alginate

AM Additive Manufacturing

API Active Pharmaceutical Ingredient

B

BHI Brain Heart Infusion

βglu β-glucan

C

CA Citric acid

CaCl₂ Calcium chloride

CAD Computer Aided Design

CEC Cation Exchange Capacity

CIJ Continuous Inkjet Printing

CS Corn starch

CTR Untreated Cells

D

DS Dissolution capacity

DSC Differential Scanning Calorimetry

DSMO Dimethyl Sulfoxide

DTS_t Dynamic Temperature Step Test

E

ECM Extracellular matrix

EHT Electron High Tension

EMA European Medicines Agency

Eq. Equation

EtOH Ethanol

F

F Filament

FDA Food and Drug Administration

FDM Fused Deposition Modelling

FFF Fused Filaments Fabrication

FT-IR Fourier Transform Infrared

FU Farmacopea Ufficiale Italiana

G

G.R.A.S. Generally recognized as safe

GDPs Good Documentation Practices

GLPs Good Laboratory Practices

Gly Glycerol

GMPs Good Manufacturing Practices

H

HAL Halloysite

HIPS High-Impact Polystyrene

HME Hot Melt Extrusion

HMW High molecular weigh

HPC Hydroxypropyl Cellulose

HPMC HydroxyPropyl Methylcellulose

HPU High Power Ultrasound

I

IR Infrared

L

LMW Low molecular weigh

M

MER Material Extrusion Rate

MgSt Magnesium stearate

MHA Mueller-Hinton Agar

MHAB Mueller-Hinton Agar 5 % defibrinated sheep blood

MMPs Matrix metalloproteinases

MMT Montmorillonite

MRSA Methicillin Resistant

Staphylococcus aureus

MSM Methyl sulfonyl methane

N

NaHy sodium hyaluronate

P

PAM Pressure-Assisted Microsyringe

PCL Polycaprolactone

PEG Poly (Ethylene Glycol)

PET plastic

PET-G Polyethylene Terephthalate
Glycol-modified

Phr Parts per hundred resin

PLA Polylactic Acid

PTFE Teflon

PVA Poly (Vinyl Alcohol)

PVP Polyvinylpyrrolidone

R

R.T. Room temperature

RH Relative humidity

ROS Reactive oxygen species

RST Dynamic Rate Sweep Test

S

.stl Standard Triangulation Language

SEM Scanning Electron Microscopy

SLA Stereolithography

SPARC Secreted protein, acid and rich in
cysteine

SRT Transient Step Rate Test

SSE Semi-solid extrusion

SWF Simulated Wound Fluid

T

TEM Transmission Electron Microscopy

T_g Glass transition temperature

TGA Thermogravimetric Analysis

TIMPs Tissue Inhibitor
Metalloproteinases

TPS Thermoplastic starch-based

V

VEGF Vascular endothelial growth
factor

VFR Volumetric flow rate

W

WHO World Health Organization

WSH Water Holding Studies

X

XRDP X-ray Powder Diffraction

Overview

A wound can be defined as a damage or rupture of a biological tissue with the consequent loss of protective function. Wound treatment represents a serious health and socioeconomic problem. The implementation of wound treatments is necessary to improve patient's quality of life and reduce healthcare costs through innovative *ad hoc* formulations, capable of both promoting and accelerating the healing process. A further challenge is to do it with the utmost respect and safety, minimizing risk to humans and environment by using eco-friendly raw materials and green production methods. The aim of this thesis was to develop bio-sustainable corn starch (CS)-based patches for wound treatment. Studies involve the development and characterization of compositions (semisolid and solid) suitable to be processed by 3D printing. In particular the attention was focused on Pressure-Assisted Microsyringe (PAM) and Fused Deposition Modelling (FDM) techniques. In the first part of the research, starch-based hydrogel compositions, suitable for PAM 3D printing, were developed and characterized. Starch was combined to the plasticizing agent glycerol (Gly) and an aqueous suspension of β glucan (β glu) (soluble and insoluble fraction), obtained from barley, as filler (G4- β glu). Another hydrogel (NaHy-H2) was prepared, adding sodium hyaluronate (NaHy) to the previous composition. Then, 3D printing parameters were optimized (nozzle size 0.8 mm, layer height 0.2 mm, 100% infill density, volumetric flow rate 3.02 mm³/s and printing speed 15 mm/s). As the object must be dried after printing, post-printing drying conditions (T°C and time) were evaluated and the most suitable fixed at 37°C for 24 h. The obtained patches (G4- β glu and NaHy-H2) presented low mechanical strength thus, in order to improve this property, it was decided to perform their printing on an alginate-based (Alg) support which will be the backing layer of the final formulation. Thus, patches named Alg_ β glu and Alg_NaHy were produced and deeply characterized in terms of mechanical properties, wettability, swelling ability, morphology. The Alg_NaHy patch showed better results than the Alg_ β glu patch in terms of compactness, tensile strength, elasticity, bioadhesiveness, ease of handling, and ease of patch application and removal. The biological activity (safety and wound healing capacity) of the soluble fraction of β glu was evaluated in vitro on keratinocytes (cell line representative of epidermidis).

In the second part of the research, starch based thermoplastic filaments suitable for FDM 3D printing were optimized. Filaments based on biopolymers are not currently available on the market due to their limited thermal stability (influencing the extrusion process by FDM). For this reason, starch is generally combined to synthetic polymers in order to improve its processability. The aim of this work was to produce eco-friendly filaments by using starch as polymer combined to additives as clays (MMT, HAL), citric

acid (CA), magnesium stearate (MgSt) in order to improve the physicochemical and biological properties of TPS filaments. The filaments were characterized in terms of: morphology (SEM), thermal profile (DSC-TGA), chemical interactions (FT-IR) swellability, processability by FDM. The introduction of the clay MMT, as well as CA and MgSt, allowed to obtain filaments with suitable processability (F3b and F4 filaments). F4 filament showed good thermal properties during the 3D printing process and also, less diameter changes at the time of printing than the other filaments, allowing a stable printing. Thus, by using the selected filaments, prototypes patches were prepared by FDM (Patches A and B). For this purpose, the optimization of the 3D printing parameters (nozzle diameter 0.6 mm; printing temperature and build plate temperature 210 and 80°C, respectively; layer height 0.3 mm; top/bottom layer thickness 0.3mm; flow rate 97%; fan speed 30%; print speed 60 mm/s; and infill density 100%) was carried out. Patch B presented a more homogeneous appearance than patch A, being potentially useful as a wound dressing, although future studies in greater depth will be necessary.

Resumen

Una herida puede definirse como un daño o rotura de un tejido biológico con la consiguiente pérdida de su función protectora. El tratamiento de heridas representa un grave problema sanitario y socioeconómico. La aplicación de tratamientos para heridas es necesaria para mejorar la calidad de vida de los pacientes y reducir los costes sanitarios mediante formulaciones innovadoras ad hoc, capaces tanto de promover como de acelerar el proceso de cicatrización. Otro reto es hacerlo con el mayor respeto y seguridad posible, minimizando los riesgos hacia las personas y el medio ambiente, utilizando materias primas ecológicas y métodos de producción ecológicos. El objetivo de esta tesis era desarrollar parches biosostenibles a base de almidón de maíz (CS) para el tratamiento de heridas. Los estudios incluyen el desarrollo y la caracterización de composiciones (semisólidas y sólidas) adecuadas para ser procesadas mediante impresión 3D. En particular, la atención se centró en las técnicas de microinyección asistida por presión (PAM) y de modelado por deposición fundida (FDM). En la primera parte de la investigación, se desarrollaron y caracterizaron composiciones de hidrogel a base de almidón, adecuadas para la impresión 3D PAM. El almidón se combinó con el agente plastificante glicerol (Gly) y una suspensión acuosa de β glucano (β glu) (fracción soluble e insoluble), obtenido de la cebada, como relleno (G4- β glu). Se preparó otro hidrogel (NaHy-H2), añadiendo hialuronato sódico (NaHy) a la composición anterior. A continuación, se optimizaron los parámetros de impresión 3D (tamaño de boquilla 0,8 mm, altura de capa 0,2 mm, densidad de relleno del 100%, caudal volumétrico 3,02 mm³/s y velocidad de impresión 15 mm/s). Dado que el objeto debe secarse tras la impresión, se evaluaron las condiciones de secado post-impresión (T°C y tiempo) y se fijó la más adecuada en 37°C durante 24 h. Los parches obtenidos (G4- β glu y NaHy-H2) presentaron una baja resistencia mecánica por lo que, para mejorar esta propiedad, se decidió realizar su impresión sobre un soporte a base de alginato (Alg) que será la capa de soporte de la formulación final. Así, se produjeron los parches denominados Alg_ β glu y Alg_NaHy, que se caracterizaron en profundidad en términos de propiedades mecánicas, humectabilidad, capacidad de hinchamiento y morfología. El parche Alg_NaHy mostró mejores resultados que el parche Alg_ β glu en cuanto a compacidad, resistencia a la tracción, elasticidad, bioadhesividad, facilidad de manipulación y facilidad de aplicación y retirada del parche. La actividad biológica (seguridad y capacidad de cicatrización de heridas) de la fracción soluble de β glu se evaluó in vitro en queratinocitos (línea celular representativa de epidermidis).

En la segunda parte de la investigación, se optimizaron los filamentos termoplásticos a base de almidón adecuados para la impresión 3D FDM. Los filamentos

basados en biopolímeros no están disponibles actualmente en el mercado debido a su limitada estabilidad térmica (que influye en el proceso de extrusión por FDM). Por este motivo, el almidón se suele combinar con polímeros sintéticos para mejorar su procesabilidad. El objetivo de este trabajo fue producir filamentos ecológicos utilizando almidón como polímero combinado con aditivos como arcillas (MMT, HAL), ácido cítrico (CA), estearato de magnesio (MgSt) con el fin de mejorar las propiedades fisicoquímicas y biológicas de los filamentos de TPS. Los filamentos se caracterizaron en términos de: morfología (SEM), perfil térmico (DSC-TGA), interacciones químicas (FT-IR) hinchabilidad, procesabilidad por FDM. La introducción de la arcilla MMT, así como de CA y MgSt, permitió obtener filamentos con una procesabilidad adecuada (filamentos F3b y F4). El filamento F4 mostró buenas propiedades térmicas durante el proceso de impresión 3D y además, menor cambio de diámetro en el momento de impresión que el resto de filamentos, permitiendo una impresión estable. Así, utilizando los filamentos seleccionados, se prepararon prototipos de parches por FDM (parches A y B). Para ello, se llevó a cabo la optimización de los parámetros de impresión 3D (diámetro de la boquilla 0,6 mm; temperatura de impresión y temperatura de la placa de impresión 210 y 80°C, respectivamente; altura de la capa 0,3 mm; grosor de la capa superior/inferior 0,3 mm; tasa de flujo 97%; velocidad del ventilador 30%; velocidad de impresión 60 mm/s; y densidad de relleno 100%). El parche B presentó un aspecto más homogéneo que el parche A, siendo potencialmente útil como apósito para heridas, aunque serán necesarios futuros estudios en mayor profundidad.

1. INTRODUCTION

1.1. Wounds

A wound can be defined as a damage or breakdown of a biological tissue involving the loss of the protective function of the skin and the continuity of the epithelium and underlying tissues as a result of a mechanical trauma, chemical injury, extreme temperature, and pathological conditions (1). Wounds can be classified in different ways, one of them as based on the nature of the repair process and the healing time wounds can be classified as acute or chronic wounds (1) (**Figure 1.1**).

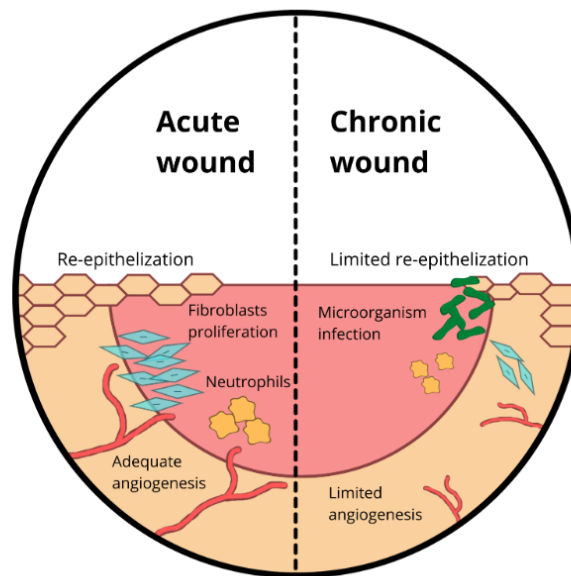


Figure 1.1. Pathological activities that occur in an acute and chronic wound (2).

Acute wounds are usually injuries that undergo a reparative process that can be easily divided into a series of orderly and well-known steps; this results in the rapid restoration of the anatomical and functional integrity of the damaged skin. They are tissue injuries that heal completely, with minimal scarring and have a maximum healing time frame of 8-12 weeks, depending on size and depth in epidermis or dermis layer. Primary causes of acute wounds are mechanical damages, as in the case of abrasion, penetrating and surgical injuries. Another category of acute wounds is represented by burns and chemical injuries caused by thermal sources, electricity and radiations (3). Example of acute wounds are shown in **Figure 1.2**.



Figure 1.2. Examples of acute wounds: abrasions (A, B), burn (C) and cut (D).

Chronic wounds heal slowly or incompletely and often reoccur, because of a failure in the repair process due to either further tissue insult or pathological conditions such as diabetes, persistent or inadequately treated infections, and ulcers (**Figure 1.3**). These wounds require long healing time (more than 12 weeks) or do not heal. Chronic wounds include decubitus ulcers, vascular ulcers, diabetic foot, etc. (1,3). Due to non-healing, these wounds are very susceptible to bacterial colonization of both Gram-positive and Gram-negative bacteria, including *Staphylococci*, *Enterococci*, *Enterobacteriaceae*, *Pseudomonas* and *Finegoldia* (4).



Figure 1.3. Examples of chronic wounds.

1.1.1. Phases of wound healing process

The wound healing process is represented by complex cellular and molecular orchestrated events that lead to tissues repair and skin physiological functions restoration. It required the activity of multiple cell types and microenvironments (5) such as blood cells, inflammatory mediators, immune system cells, epithelial and connective tissue cells, coagulation factors, growth factors and cytokines (6). This process is composed of four integrated and overlapping phases as shown in **Figure 1.4**.

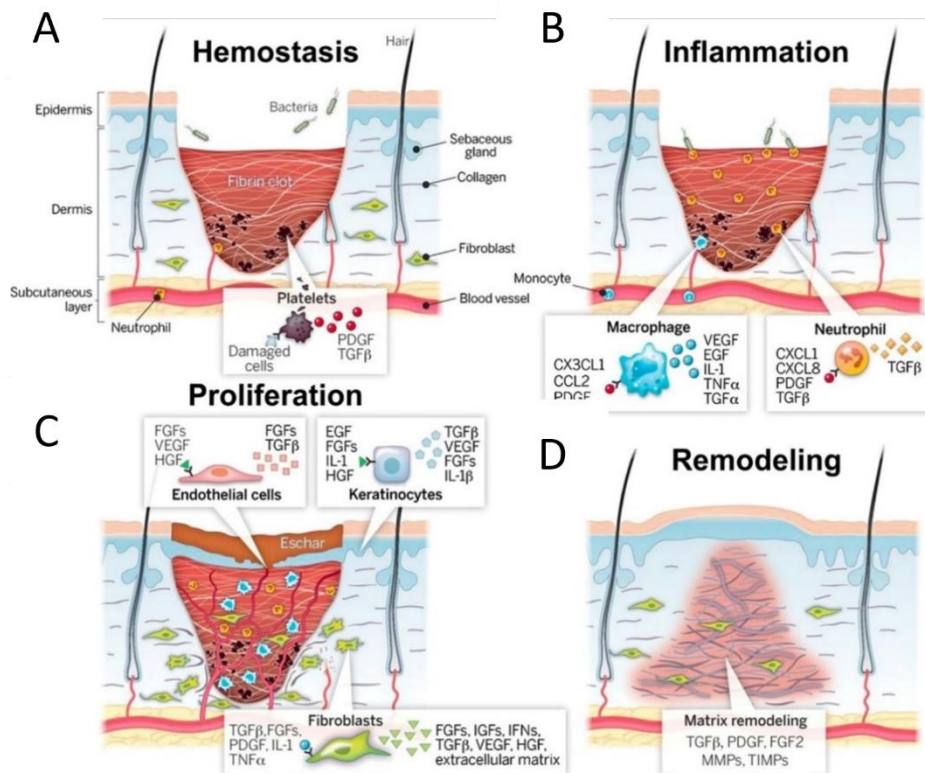


Figure 1.4. Stages of wound repair and their major cellular components (7).

Haemostasis: this phase begins immediately after injury and lasts only 5-10 minutes. It is characterized by vascular constriction and platelet activation by thrombin encountering the vascular subendothelial matrix. Platelet aggregation creates a fibrin insoluble clot at the wound site, reducing blood leakage from the damaged vessels. This temporary shield contains many important factors like fibronectin, SPARC (Secreted protein, acid and rich in cysteine), thrombospondin, vitronectin and growth factors (TGF- β , PDGF, FGF, EGF, IGF-1) that bind to cells (for example fibroblasts and keratinocytes)

and to other extra-cellular matrix (ECM) proteins conditioning the next healing phase (6,8).

Inflammation: it is characterized by vasodilation, increase of vessel permeability and white blood cells migration to the damaged site. Neutrophils, macrophages and lymphocytes are attracted by a complex interplay of cytokines and chemokines promoting this phase. Neutrophils arrive first and have the function of phagocyte microbes and cellular debris, degrade matrix protein, attract other neutrophils and macrophages and also produce proteases, reactive oxygen species (ROS) and antimicrobial peptides. In the absence of infection, neutrophil infiltration decreases in few days. At the same time, circulating monocytes get into the wound tissue and differentiate into macrophages in the first 24 h from the injury. They are master effectors of the healing process with an important phagocytic activity toward dead microbes, wound debris and apoptotic neutrophils. In addition, macrophages stimulate granulation tissue formation and angiogenesis for the next phase by releasing PDGF, VEGF, TGF- β , FGF, IL-1, IL-6, and TNF- α . The inflammatory step starts within 24 h and lasts for about 3 days (3,6,8).

Proliferation: it begins within 24 h from the injury and occurs between 4 and 21 days; this phase is characterized by re – epithelialization, ECM formation and angiogenesis (5) as well as by the secretion of growth factors and cytokines. Macrophages help solving inflammation by their phagocytotic activity. In addition, they have a stimulatory action towards fibroblasts, keratinocytes and angiogenesis (6). New blood vessels are created by the release of vascular endothelial growth factor (VEGF) that leads to microvascular endothelial cells proliferation with consequent vascular network formation. Fibroblasts are the main responsible for substituting the fibrin-rich matrix with granulation tissue producing collagen, ECM proteins, elastin and matrix metalloproteinases (MMPs) that degrades the provisional matrix. This granulation tissue acts as a structure that supports migrated and differentiated cells as well as angiogenesis and new ECM deposition (6). Moreover, stimulated keratinocytes migrate from the wound edge and slide over each other with a typical ‘leapfrogging’ movement to reform the epidermal layer (re-epithelialization) (6,7). These new keratinocytes release MMPs facilitating their migration and also produce ECM proteins and proteases-like plasmin to recreate a new basement membrane. Plasmin is essential to the breakdown of fibrin clot and to establish a thin epithelial layer during the long healing phase (6). Collagen is maximally secreted between 5 to 7 post-injury days, type 3 (fetal collagen) is initially more representative. At the same time, glycosaminoglycans (hyaluronan, chondroitin

sulfate/dermatan sulfate, heparan sulfate/heparin and keratan sulfate) and proteoglycans (versican, perlecan, neurocan, aggrecan and fibromodulin) get involved in the composition of the extracellular matrix conferring strength and support (3). According to all of these biochemical processes, there is the formation of a connective structure called scar.

Remodeling: it follows the proliferative phase and lasts from 3 weeks to years (5). Wound contraction begins by day 5 because of the phenotypic change of fibroblasts. The new tissue has 80% similarity compared to the original one (3).

Referring to chronic wounds, the wound healing process arrests in the inflammatory phase. Patients often show vascular impairment that takes to a compromised immune response and vulnerability to infections. In this case, the level of neutrophils and macrophages rises and creates a pro-inflammatory environment that cannot provide to eradication of infection. Other important factors that characterize chronic wounds are the decrease of angiogenic mediators, a dysregulated cytokine/growth factor expression, the high ROS level, the poor re-epithelialization due to the decreased proliferation and migration of keratinocytes and also the integrity of ECM affected by excessive degradation for an altered equilibrium of MMPs and tissue inhibitor metalloproteinases (TIMPs) (9). Collectively, these molecular and cellular abnormalities severely prevent the correct ECM deposition and granulation tissue formation, leading to a chronic wound (10).

1.1.2. Complications and infections

The complications of wounds are responsible for a reduced quality of patient life and include infections (gangrene, sepsis, abscess formation), malignant transformations, severe functional limitations (lower-extremity amputations) and hemorrhages (11). Infections are the leading cause of non-healing and are responsible for the persistence of the inflammatory events. Numerous bacteria responsible for wounds infection belong to skin microbiota and under healthy conditions are useful for the barrier properties maintenance. However, these bacteria can cause serious infections in case of wounds. It has been demonstrated that a low level of bacteria facilitates the healing process due to their ability to produce proteolytic enzymes (hyaluronidase) that helps wound debridement and also, stimulate neutrophils to release proteases, important for speeding up tissue regeneration (12). It has been proposed a maximum reference value of 10^5 CFU/g of tissue of bacterial load that is considered to impede regular healing process.

This threshold is correlated to the host immune system conditions (diabetes, malnutrition, obesity, advanced age etc.), to the type and number of bacterial species in the wound and also, to the local environment (13). Therefore, it is necessary to differentiate between wound contamination, colonization, critical colonization and infection. The ‘contamination’ is the presence of non-replicating micro-organisms due to the hostile environment of human tissue; ‘colonization’ is the presence of replicating bacteria without causing a marked host response (physiological status) that is different from ‘critical colonization’ where the increased bacterial burden causes a non-healing stage with chronic inflammation (wound friability, atrophy and deterioration of granulation tissue, increased exudate). With the increase of bacterial burden, that overcomes the host immune response, the colonized wound aims to transform into a covert infection that could proceed to a compromised infection or a systemic dissemination (sepsis). Infections are often characterized by pyrexia, local pain, purulence, erythema, swelling, and oedema (12,13). Infected chronic wounds do not exhibit all these typical clinical signs of infection due to problems of oxygenation, poor perfusion, immunodepression, comorbidity, advanced patient age and other factors that reduce the classic host response and its symptoms. To identify chronic wound infection, literature data describes increased wound size, lymphangitis, extension of the wound to bone, fragile granulation tissue, serous exudate, and foul odor (12–14).

The role of microorganisms in chronic wounds has been extensively studied and is well-established that these wounds have a colonizing flora that changes over time. In the first acute phase, normal skin flora are the predominant organisms: Gram-positives such as *S. Aureus*, coagulase-negatives staphylococci (*S. Epidermidis*) and beta-hemolytic streptococci are the most common isolated bacteria. Over the time of about 4 weeks, a chronic wound usually becomes colonized by facultative anaerobic Gram-negative species such as *Proteus*, *E. coli*, and *Klebsiella*. According to the low tissue oxygen level typical of chronic wounds, anaerobic flora growth is facilitated (*Prevotella sp.*, *Bacteroides*, *Peptostreptococcus sp.*) and becomes a significant component of the local microbial population when the level of wound deterioration increases and involves deeper structures. Other species, including *Enterobacter cloacae*, *Enterococcus sp.*, *Pseudomonas sp.*, and fungi, have also been reported. As time passes, wounds of month life contain an increasing number of pathogens. Furthermore, conditions like hospitalization, prolonged use of broad-spectrum antibiotics and surgical procedures

make patients exposed to resistant organisms like Methicillin Resistant *Staphylococcus aureus* (MRSA) or vancomycin-resistant *Enterococci* (13,14).

1.1.3. Social and financial impact

Wounds treatment is an acknowledged and serious healthcare and socioeconomic problem. Whatever the cause, wounds have a severe but frequently unrecognized effect both on the quality of patient and on the health care system. For this reason, wound have been defined as a "silent epidemic" in last few decades. Chronic wounds are a common cause of morbidity and mortality that affect patients physical, mental and social wellness. Chronic wounds frequently result in ongoing pain, discomfort, and limited mobility. These physical symptoms can negatively impact on the capacity to engage in social activities, work, and personal relationships, which in turn can negatively influence the mental health of the patient. According to a recent World Health Organization (WHO) survey, more than 305 million people worldwide are affected by wounds, both acute and chronic (15). Besides, between 20 and 60 million people are anticipated to experience chronic injuries by 2026 (9). About 2 million people in Europe and 7 million people in the US suffer from chronic wounds, according to statistics. In addition, it should be highlighted that the number of people with chronic wound is significantly rising due to an increase in life expectancy and the prevalence of comorbid conditions. According to estimates, 1% to 2% of people worldwide will experience chronic wounds at some point in their lives (16). Furthermore, the cost of treating these wounds is a significant health and socioeconomic issue (17) since in most cases, it is required: long-term medical care and specialized treatments such as bandages and medicines (18).

The costs associated with these treatments can become an important economic burden for the patients themselves and/or their families, but also for the healthcare system. It has been estimated that wound treatment reaches 3% of all health spending in the UK, approximately £5 billion annually. In the US, it is estimated that more than \$25 billion is spent on chronic wound treatment. In Europe, considering only people affected by DFUs (diabetic foot ulcers), the expenditure amounts to about 6 billion of year (18). For all types of wounds, costs range between \$28,100 and \$96,8 billion, and the wound medicine business is expected to exceed \$16,5 billion by 2024 (19).

Addressing this social impact clearly suggests the importance and need to develop new strategies to overcome the limitations of current medicines, promote the wound

healing process and prevent its complications, especially in the case of chronic wounds, improving the quality of life of patients and reducing healthcare costs (20).

1.2. Formulations for wound treatment

The healing process of both acute and chronic wounds can be promoted and accelerated by the use of specific dressings having different characteristics and functionalities, depending on the wound type. Typically, wound dressings are designed to promote the healing processes by inhibiting infections as well as helping the repair processes activating physiological mechanisms involved. The ideal wound dressing should have long-term stability, provide appropriate moisture conditions so that the wound is neither too moist (which promotes bacterial proliferation and delays healing) nor too dry, promote tissue regeneration, not cause pain during the removal and have appropriate mechanical and adhesion properties (21). Another important aspect to consider is represented also by the biocompatibility and sustainability of the wound dressing. It is very important to dispose of a product totally eco-friendly in order to decrease the environmental impact during the production and after the use (waste).

Wound dressings can be classified according to their function in the wound (e.g. antibacterial, occlusive), type of material employed (e.g. hydrocolloid, alginate, collagen) and the physical form of the wound dressing (e.g. foam, film, gel) (1).

Hydrocolloids (**Figure 1.5A**) are among the most frequently used dressings as they can be applied to both moist and dry wounds. They consist in cross – linked polymeric matrices, such as starch, cellulose, gelatin, pectin, and guar gum integrated with adhesives in order to adhere to skin. In contact with wound exudates, hydrocolloids absorb water forming gels. The dressing is self-adhesive, waterproof and does not require an additional dressing, making it easy to use. These dressings are useful for superficial skin disruption such as pressure ulcers, abrasions, superficial burns or post – operative wounds, and should be changed every 2 to 4 days. A limit could be represented by the difficulty to check the wound due to the opaque nature of the dressing (22).

Alginates (**Figure 1.5B**) derive from brown algae and are polymers constituted by the two monomers (1-4)-linked, D-mannuronate and L-guluronate, interacting with calcium ions, that provides absorptive capacity. Calcium ions exchange with sodium ions in wound exudate forming an alginate gel. The gel is highly absorbent, making this dressing the best choice for highly exudative wounds; in fact, these dressings can absorb

up to 20 times their weight in exudates. Alginate dressings are employed for deep pressure ulcers, pyoderma gangrenosum, and exudative ulcers on the lower extremity. If not changed at least once per week, alginates dressings can dry and adhere to the wound, leading to pain in removal from the patient (5,23)

Hydrogels (Figure 1.5C) are networks formed by cross-linked polymers composed of up to 96% water. They are the most common treatment for dry wounds due to their excellent ability to hydrate and maintain a moist environment. In addition, they are refreshing and pain-relieving. They are available in different physical states: sheets, amorphous gels (dry or premixed) and impregnated gauzes. Because of their high-water content, hydrogels have a limited absorption capacity and therefore, they are not suitable for exudative wounds. Hydrogels are not provided for adhesion capacity thus once applied on skin require an additional dressing to remain in the application site. Dressings should be changed at least every 1-3 days, depending on the hydration requirements of the wound (22).

Foams (Figure 1.5D) are typically represented by polyurethane or silicone foam with a semi-occlusive outer layer. The outer layer is permeable to water vapor and protects against the penetration or leakage of bacteria, while the polyurethane core consists of a hydrophilic surface that will take contact with the wound with absorption capacity and a hydrophobic backing. Foams are particularly suitable for bony prominences or within exudative cavities and must be changed every time the dressing becomes soaked with exudate, which can range from one day to once or twice a week (22,23).

Hydrofibers (Figure 1.5E.) consist of carboxymethylcellulose that forms gels interacting with wound exudates and can be three times more absorbent than alginates. In addition to their absorbent capabilities, these dressings can be left in place for several days, reducing dressing changes and costs. They have a lower wicking capacity than alginates and can cause less maceration. However, the fibrin material that is formed may adhere to the underlying wound bed, necessitating the use of saline to facilitate removal (5).

Traditional patches (Figure 1.5F) (24) represent an interesting wound treatment formulation. This kind of dressings could overcome some limitations of the most used dressings above described. One of the problems is the use of non-biocompatible and painful materials to promote the adhesion to the skin. This can lead to reduced patient compliance (reduced adherence to the therapy), as the removal is traumatic and painful with high possibility of damage of the new-formed tissue.

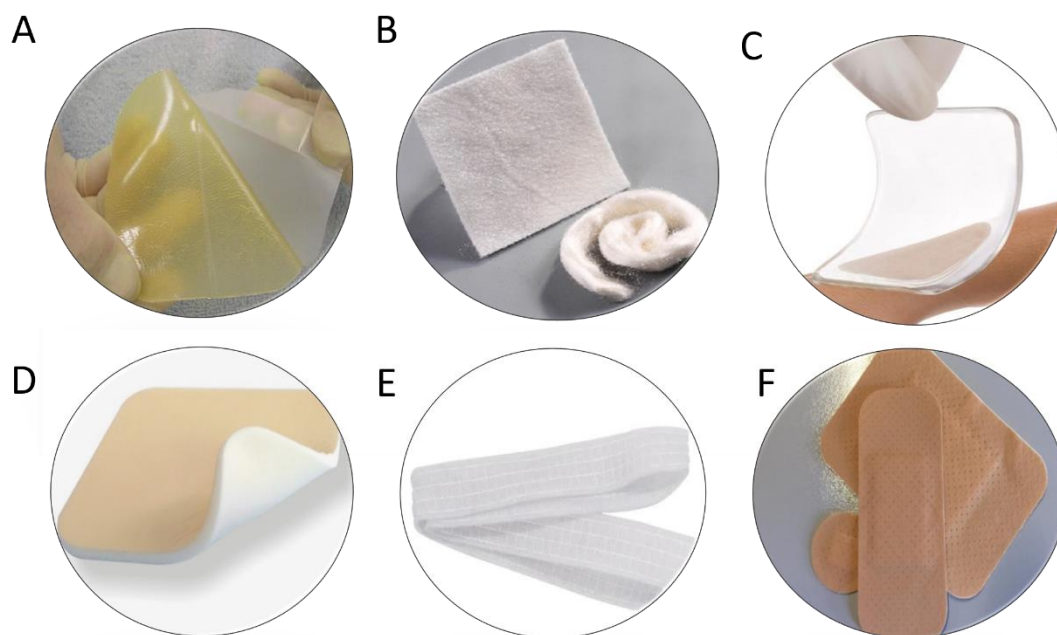


Figure 1.5. Formulations for wound treatment: hydrocolloids (A), alginate (B), hydrogel (C), foams (D), hydrofibers (E) and traditional patches (F).

An ideal patch should be safe and self-adhesive, as well as biocompatible and eco-sustainable. In order to satisfy these requirements, bioadhesive and biocompatible polymers can be used, avoiding the use of synthetic adhesives. A suitable patch should also be able to adhere to the skin surface and wound bed, to have a high residence time at the application site, to be easily removable (e.g. by washing), to release the active ingredient, to protect the damaged skin, to be permeable to oxygen and water (transpiration), to promote healing as well as to possess adequate mechanical properties (resistance to solicitations during production, application and use) (21,24).

The development of these patches requires the use of polymers having both filming and bioadhesive properties. These patches can be developed either with biopolymers or with synthetic or semi-synthetic polymers. Certainly, the use of biopolymers allows to obtain a sustainable and thus eco-friendly formulation, and for this reason most preferable. Some of the most widely used natural polymers are cellulose, alginates, hyaluronic acid, collagen, starch and acacia gum. The advantages of these materials are their non-toxicity, non-antigenicity, inertness, biocompatibility, biodegradability, bioadhesivity and antimicrobial properties. However, compared to synthetic polymers (e.g., poly (vinyl pyrrolidone) (PVP), poly (vinyl alcohol) (PVA),

polyurethanes), they have limited mechanical properties that could limit their application in this field (25). This issue could be easily solved by combining, for instance, natural additives that could function as fillers.

This problem is often overcome by the use of natural fillers as cationic clays. They are natural inorganic ingredients, such as clays (e.g. montmorillonite (MMT)), that act as multitasking agents able to improve physical (mechanical resistance and water vapor transmission), chemical (release of drugs, hemostasis and/or adsorption of exudates and moisture) and biological (antimicrobial effects and improvement of healing) properties of wound dressings (26). Lamellar inorganic clays are interesting materials largely used in many fields such as health (27). Clay minerals are divided in cationic and anionic and both can be easily found in nature (28); however, cationic clays are the most commonly available. Among these materials, the phyllosilicates are very interesting showing a high surface reactivity (high adsorption, cation exchange, colloidal or swelling capacity), good rheological behaviour, high acid-adsorption capacity, and high water dispersibility. For these reasons they are interesting material to be used in medical and biomedical applications (29). In the family of cationic clays, bentonite is the most popular and used in many health products as excipient with different functions as rheological, filler, gelling, adsorbent agent, etc (30,31).

Cationic clays are in general widely used as fillers for topical formulation as lipogels, emulsions, suspensions and patches and they are very interesting especially in the case of polymeric formulations. Especially in the case of polymeric patches, the final performances of the formulations (mechanical properties, adhesion capability, etc.), depend on interactions between the clay and the polymer (32–34). There are three possibilities when a clay filler and a polymer interact: 1) macrocomposite or conventional composite, 2) interlayer and 3) exfoliated nanocomposite (35) (**Figure 1.6**). In the case of the macrocomposite, the clay filler stacking is maintained due to the inability of the polymer chains to squeeze between the clay galleries. The clay exists as aggregates and there is little or no interaction between the clay and the polymer. In the interbedded structure, swelling of the clay occurs because the polymer chains are able to squeeze between the clay galleries. This is characterized by increased interlayer separation of the clay layered structure. When the clay platelets are completely detached from the original stacking and are well dispersed and randomly oriented in a continuous polymer matrix, an exfoliated structure is achieved. The exfoliated structure is believed to produce the maximum improvement in physical properties (35).

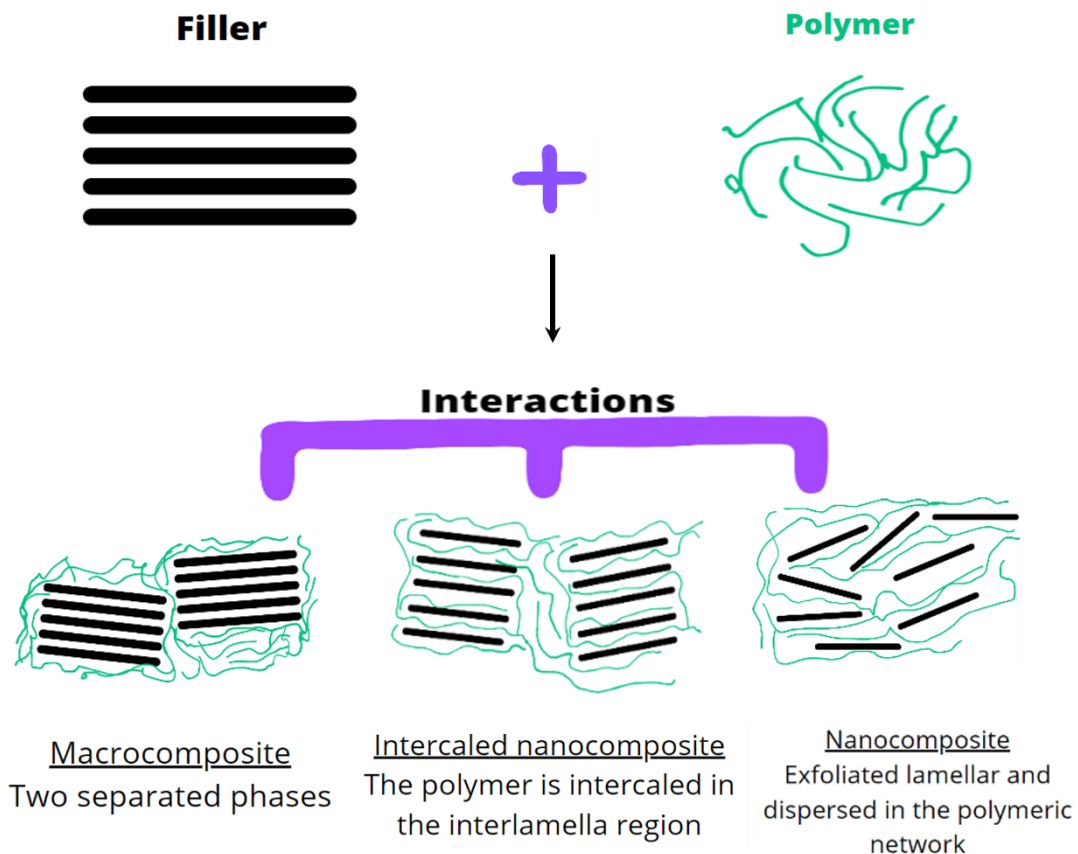


Figure 1.6. Three types of filler-polymer interaction.

1.3. Techniques for patches production

The most common methods used for bioadhesive patch preparation are the solvent casting (36), electrospinning (37,38) and three-dimensional (3D) printing (39).

1.3.1. Solvent casting

Solvent casting is based on the separation of macromolecules from a solvent phase, usually by evaporation of the solvent (**Figure 1.7**). This method has three steps: a) dissolving polymer in solvent, b) casting the solution into a mold and, c) evaporation of the solvent. Wet processes generally consist of casting a previously homogenized and vacuum degassed film forming dispersion (containing at least a biopolymer matrix, a solvent and usually a plasticizer) on a suitable base material (from which the film can be easily removed) and later drying to a moisture content which is optimal for peeling the film away. Film formation usually involves inter- and intramolecular associations or cross-linking of polymer chains forming a network that entraps and immobilizes the solvent. The degree of cohesion depends on the polymer structure, solvent used,

temperature and the presence of other molecules such as plasticizers or reinforcements. Solvent casting is a simple method that can be applied to a wide range of pharmaceuticals products using different materials. However, this method has some limitations: it may require long preparation (drying and storage times). Moreover, films stability depends on the materials used and organic solvents are often used, which must be removed to avoid any probable damage to the skin cells (36,40).

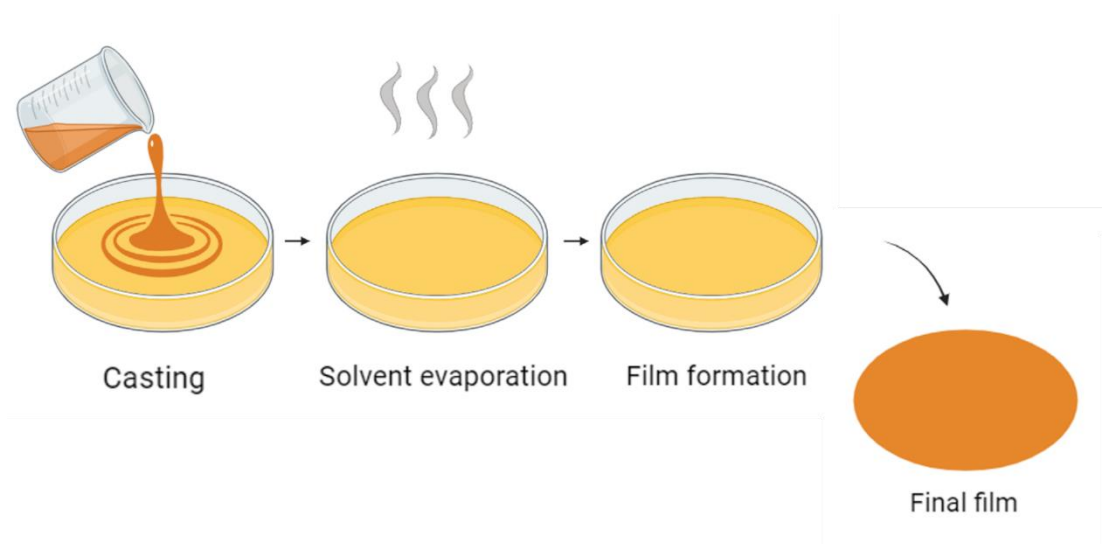


Figure 1.7. Solvent casting technique.

1.3.2. Electrospinning

Electrospinning is a simple and versatile fiber synthesis technique in which a high-voltage electric field (usually greater than 5 kV) is applied to a stream of polymer solution, thereby forming continuous micro/nanofiber (**Figure 1.8**). These nanofibers are mainly due to the size of the fibers, of the order of magnitude of the nanometer. Through adjusting the spinning parameters, it is possible to control some structural properties of the dressing to be carried out, such as porosity and specific surface area. The pore size depends on the filtering capacity of the formulation towards microorganisms, oxygen and water, thus affecting the protective, healing and moisturizing role of the formulation (41–43). The formulation, which does not involve excessive economic burden nor particular manufacturing difficulties, is also very flexible and manipulable.

Despite of several advantages and success of electrospinning, there are some critical limitations to this process, such as small pore size and lack of adequate cellular infiltration inside the fibers (44).

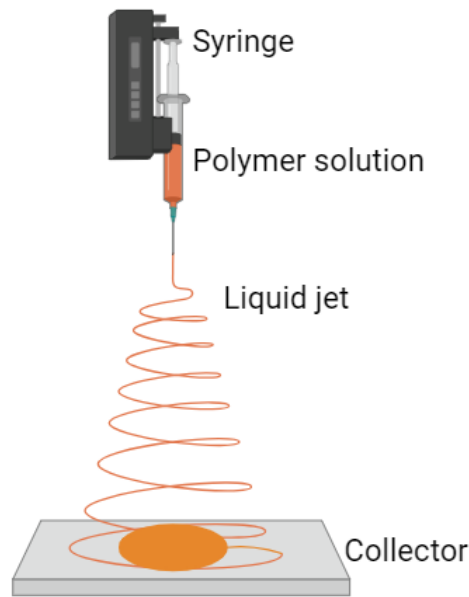


Figure 1.8. Electrospinning technique.

1.3.3. 3D printing

3D printing is a technology available since the 1980s and it was invented by Charles W. Hull. The first method of 3D printing was stereolithography (SLA) technology. SLA uses a laser to solidify photosensitive resins in a layer-by-layer process, thus creating a three-dimensional object. This invention was the basis for the subsequent development of 3D printing (45). 3D printing became a fast-growing technology due to its versatility and its huge range of applications among different fields from automotive and aerospace, electronics, consumer goods, military industry and biomedical and pharmaceutical manufacturing (46). 3D printing is an additive manufacturing (AM) technology based on the principle of layer-by-layer deposition of material in order to fabricate a specific 3D structure (printed object). In contrast, traditional manufacturing techniques, solvent casting or electrospinning, are based on the removal of material to achieve items, resulting in the production of large amounts of waste materials (39).

3D printing is previously planned through computer-aided design (CAD) software, dedicated to the creation of the 3D digital structure to be printed. Some examples of software useful for this purpose are Onshape®, Autocad® and Fusion 360®. The designed structure is then exported as a Standard Triangulation Language (STL) file

and converted into a “.gcode” using a slicer software such as Ultimaker Cura® or Slic3r® (47). It is possible to quickly print a great variety of objects with different shapes and sizes, with a higher or lower degree of resolution and employing different materials, transforming the CAD file into its physical form (**Figure 1.9**) (48).

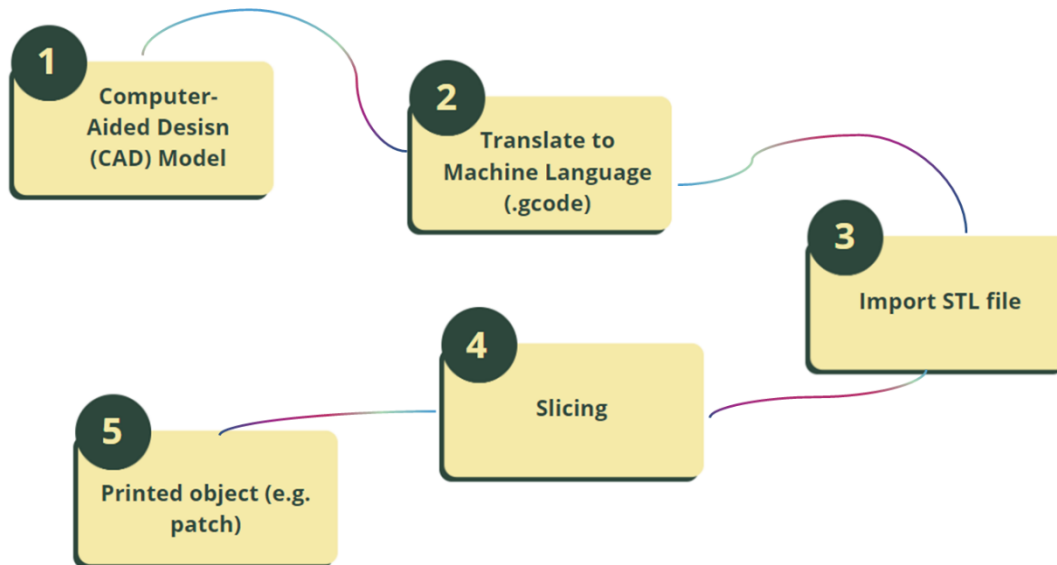


Figure 1.9. Workflow diagram for extrusion-based 3D printing process.

In addition, AM has some advantages over traditional techniques:

- greater freedom in more complex geometries. Parts that previously required assembly can be produced as individual units, which results in greater strength and durability;
- timesaving. 3D printing allows to modify the printing process, sometimes even the CAD file, without virtually interrupting the process (49);
- customisable products, as for example, it is possible to rapidly design and develop individualized dosage forms made *ad hoc* for the patient. This is especially interesting in the pharmaceutical and biomedical fields as it allows to perform personalized therapies according to the patients’ needs (50).

In the pharmaceutical industry, 3D printing has been employed for the fabrication of a wide variety of medical devices and dosage forms varying in shape, release profile and drug combination (controlled release tablets, polypills, orodispersible films, microneedles, transdermal patches etc.) (51–53).

Several 3D printing techniques have been developed and widely explored for drug delivery and pharmaceutical applications, including inkjet-based (such as Continuous Inkjet Printing (CIJ)), laser-based writing (such as SLA), extrusion-based deposition

systems (such as Pressure-Assisted Microsyringe (PAM), and Fused Deposition Modelling (FDM)). The most promising and most widely used techniques in the pharmaceutical field are those based on extrusion (54).

1.3.3.1. PAM technique

PAM or semisolid extrusion (SSE) technique involves a syringe-based head fed with a semisolid material which is continuously extruded from a tip or nozzle of suitable size as shown in **Figure 1.10**. The extrusion consists of a mechanical, solenoid, or pneumatic (pressure-air) piston. The semisolid materials composition (gels or pastes) consists of an appropriate mixture of polymer, solvent, and other additives (e.g. functional excipients), if necessary, to obtain a material suitable for PAM 3D printing (39,55).

For an adequate 3D print, it is necessary to optimize the printing parameters. The infill type (concentric, honeycomb, rectilinear, etc.) affect the uniformity of surface and mechanical strength of the printed structure. Other printing parameters including material flow rate, printing temperature, pressure, and printing speed must also be optimal and carefully controlled to achieve an appropriate finished product with good mechanical properties and resolution.

Some of the advantages of this technology that allow it to emerge quickly in the pharmaceutical field include:

- the possibility to work at room temperature (R.T.): this is helpful when working with drugs, since a wide selection of these molecules are thermo-sensitive (i.e. antimicrobial, anti-inflammatory, etc). PAM 3D printing allows them to maintain their properties unaltered (56);
- rapid fabrication time: allows the direct use of semisolid materials that are not subjected to the stress of a great system as in the FDM process (see below) and;
- high resolution.

However, PAM technique has also some limitations because the extrusion process strongly depends on the rheological properties of the semisolid materials. It is well-known that the printability of semisolids depends mainly on their viscosity. Highly viscous materials are responsible for the nozzle clogging, while low viscous materials are easily extruded, however they are responsible for 3D printed object collapse just after deposition. Moreover, post-processing phase is necessary. Depending on the composition and the final scope of the printed structure it often requires drying and/or cooling after printing, a critical step in the manufacturing of the final product. This inevitable step can

lead to deformation or shrinking of the printed object and to the formation of irregular and non-uniform regions in the final structure (57). Finally, a major drawback in PAM could be the use of solvents for semisolid preparation that may lead to lack of stability during the manufacturing phase and the last drying step.

Among the main synthetic polymers used to date Carbopol®, PVP and Poly (Ethylene Glycol) (PEG) can be mentioned. However, few are the natural polymers used for this technique (Hydroxypropyl Cellulose (HPC) and its semi-synthetic derivative, Hydroxy Propyl Methylcellulosa (HPMC)) (52).

PAM technique has been used in the design of controlled-release pharmaceutical bilayer tablets (58), immediate and sustained release fixed-drug combinations (polypill) (59), hydroxypropyl- β -cyclodextrin-based rapid-dissolving carbamazepine forms (60); and drug-loaded pastes for modified-release tablets (55).

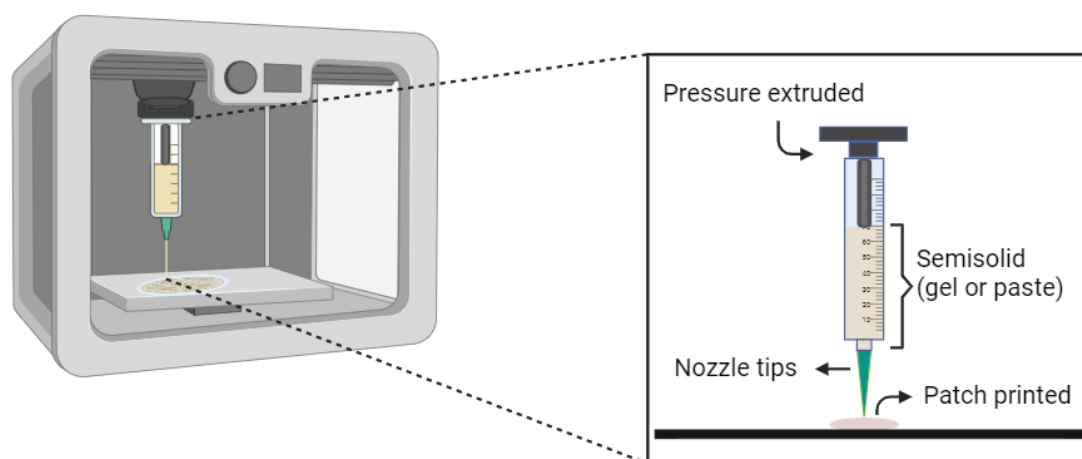


Figure 1.10. Schematic representation of PAM 3D printing technique.

1.3.3.2. FDM technique

FDM or fused filament fabrication (FFF) is based on the extrusion of a molten filament previously prepared with thermoplastic materials (61). The FDM 3D printer typically consists of a printhead and a build platform on which the object is printed. The printhead consists of a heated nozzle where the filament is melted and builds objects layer-by-layer on the platform in agreement with the 3D CAD model, as shown in **Figure 1.11** (62).

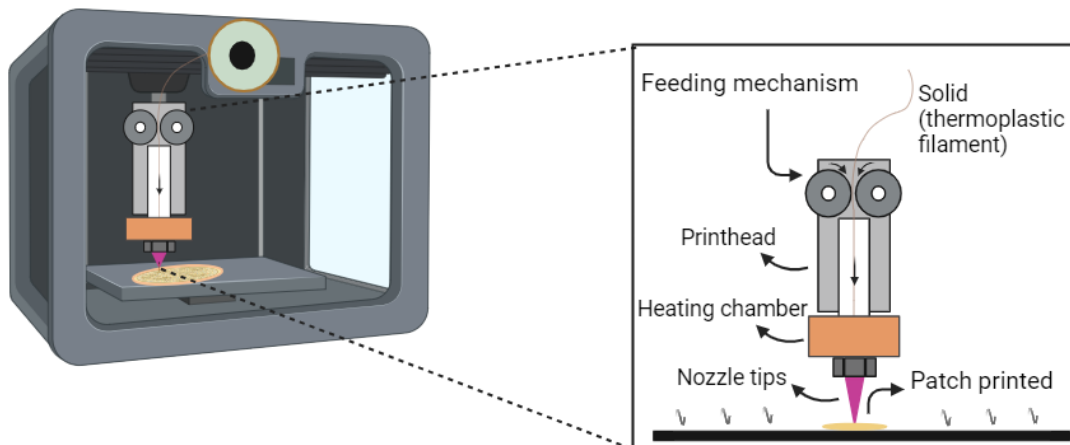


Figure 1.11. Schematic representation of FDM 3D printing technique.

The filaments used for FDM are mainly carried out by Hot Melt Extrusion (HME) process. HME is a process in which a powder mixture (such as polymer, plasticizer and other additives) is melted or softened at high temperatures and pressures. Then, the material is extruded through a screw-based extrusion system with different temperatures zones depending on the material used. Finally, the obtained filaments need to be appropriately conditioned prior to use in the FDM 3D printer (**Figure 1.12**).

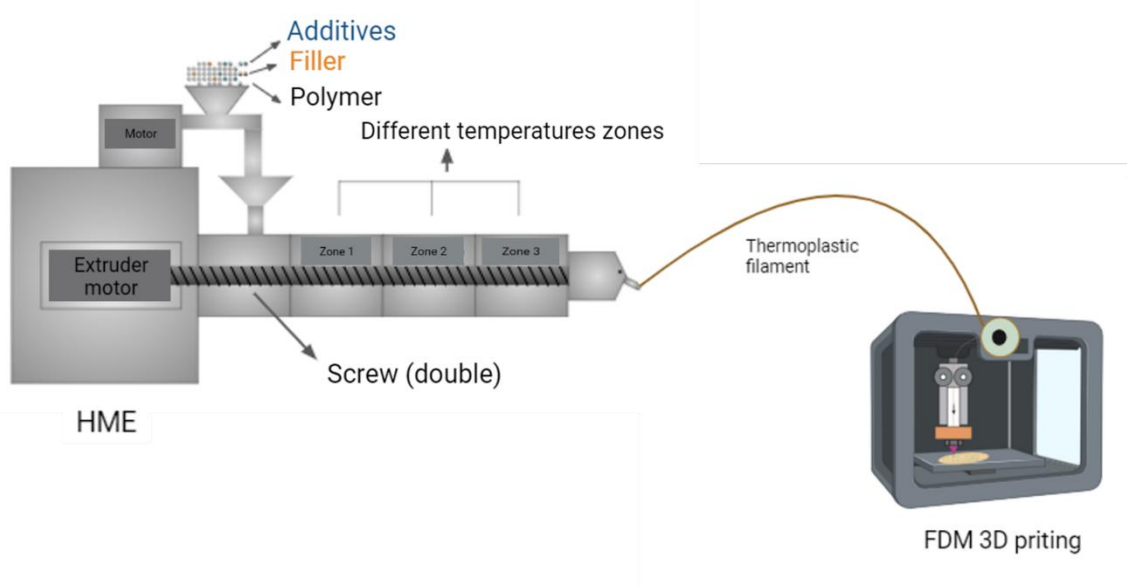


Figure 1.12. Schematic representation of HME process.

FDM technique is widely used as it has several advantages such as ease of use, scalability and affordability. It is a solvent-free 3D printing technique, which results in greater stability of the preparation and reduces any problems related to the use of solvents. In addition, due to the high working temperature prevent microbiological contamination. However, this high working temperature can also be envisaged as its main drawback, since it limits its application to heat-resistant materials (63). Also, 3D printed objects could be inaccurate and have lesser resolution than other 3D technologies. This can influence the fine details and smoothness of printed surfaces and can vary from model to model. Finally, a post-processing for printed goods could be necessary, such as more support removal or sanding to create a smoother surface. Despite all the disadvantages, this technology is in full growth in the field of pharmaceutical technology.

Commercially available filaments are made from thermoplastic polymers such as acrylonitrile butadiene styrene (ABS), high-impact polystyrene (HIPS), polyethylene terephthalate glycol-modified polyethylene (PET-G), and nylon (57). The use of FDM technique in the pharmaceutical field requires the use of pharmaceutical grade polymers, generally recognized as safe (G.R.A.S.). The most used ones in this group are PVP, PVA, polylactic acid (PLA), polycaprolactone (PCL), cellulose derivatives and polymethacrylates, polyurethanes (57,62). Addition of plasticizing agents and other coadjutants, to improve thermal and mechanical resistance is frequently required (64).

Examples of pharmaceutical systems prepared with this technique include the design of swellable/erodible capsules for oral pulsatile release (65), tablets able to disintegrate without the addition of classical disintegrants (66), and zero-order drug release floating tablets (67).

1.3.3.3. 3D printing and personalized medicine

3D printing is a good option in the field of personalized medicine (68,69). Traditional scale-focused manufacturing is based on the “one size fits all” concept where all patients receive the same drugs at the same doses and frequencies as others (53,70). However, it should be emphasized that due to interindividual variability (genetic factors, weight, age, lifestyle, and treatment history) there may be differences between subjects receiving the same therapy (53,69). Having the ability to control the dose via 3D printing is a vital tool in the goal to create personalized medicines. This involves performing a thorough diagnosis of the patient before creating the suitable formulations for them. As a

result, this technology could have a significant impact on hospitals and pharmacies wishing to offer personalized pharmaceutical formulations (**Figure 1.13**) (71). This approach is particularly interesting in pediatric patients (72), as well as in those patients with potential low adherence to the treatment (73). Taste masking is possible using some 3D printing techniques.

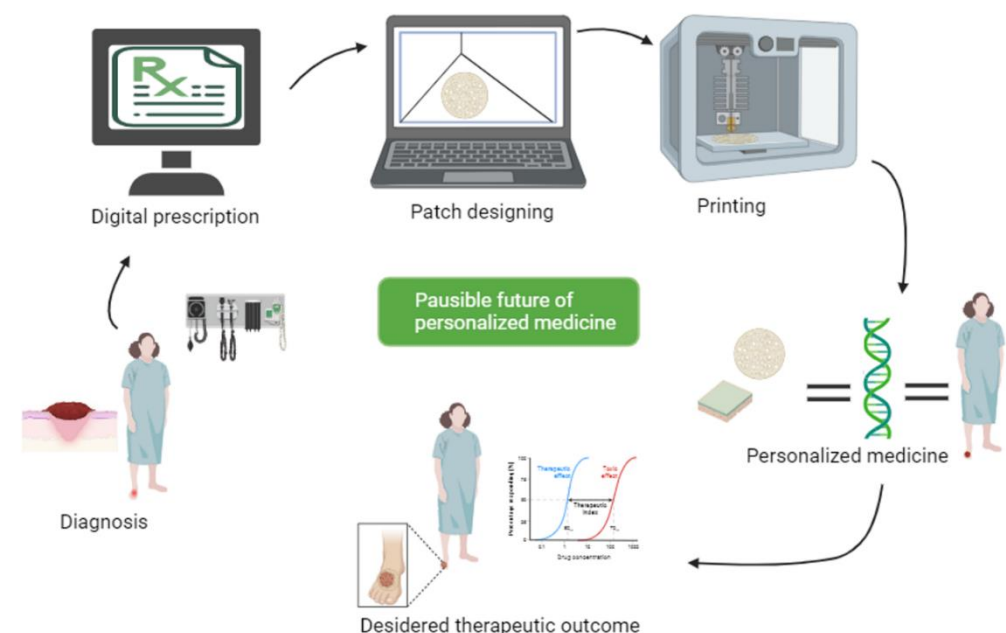


Figure 1.13. Schematic representation of personalized medicine 3D printing. Adapted from (71).

1.3.3.4. Regulatory aspects in 3D printing

In general, pharmaceutical products must meet stringent quality and safety standards. Regulatory bodies typically require manufacturers to comply with *Good Manufacturing Practices* (GMPs), *Good Documentation Practices* (GDP) and *Good Laboratory Practices* (GLP) (74) to ensure the consistency and reliability of the products (54).

Therefore, appropriate regulatory guidelines should be designed considering the manufacture and distribution of 3D printing pharmaceutical formulations. Regulatory authorities, such as Food and Drug Administration (FDA) and the European Medicines Agency (EMA), continuously adapt their guidelines and regulations to keep up with technological advancements.

In Europe, 3D printers also called as *AM machinery* or *harmonized products* fall under the Directive 2006/42/EC. Manufacturers are required to guarantee that 3D printers comply with the necessary health and safety requirements of the Machinery Directive. They must also create a technical file and affix the CE marking before placing them on the EU internal market (75). Besides the Machinery Directive, other EU legislative acts may apply to 3D printers; i.e. the Electromagnetic Compatibility Directive 2014/30/EC, and EU legislation on chemicals, WEEE 2012/19/EU, RoHS II Directive 2011/65/EU and Directive (EU) 2017/2102, and REACH 1907/2006/EU (75).

As regards to the 3D printed medical devices, they fall within the scope of specific EU product legislation, in particular the Medical Devices Directive 93/42/EEC. Therefore, manufacturers of such medical devices must ensure that 3D printed products comply with the requirements of the applicable EU legislation (75).

In USA, the FDA released guidelines in 2017 outlining the legal requirements for producing medical devices (76). For example, acceptance activities are an integral part of process control. Many AM technologies can produce more than one device or component simultaneously in different manufacturing volumes. Each of these devices or components may be a copy of a single design or different designs. This makes it more difficult to ensure repeatability and consistency within a manufacturing cycle and between batches. Therefore, it is uncertain whether regulatory approval will be required for the finished product and the rules that control every step of product design and production (76,77) It is important to carry out substantial clinical trials that guarantee the safety of the patient.

Currently, there is only one 3D printing drug in the market with FDA approval (SPRITAM®). SPRITAM® is an orally disintegrating tablet form of levetiracetam, primarily used for the treatment of epilepsy, manufactured by *Aprecia Pharmaceuticals Company* (USA) (70).

Finally, it is important to note that the regulatory landscape for 3D printing in pharmaceutical applications may vary from country to country. On balance, the lack of a regulatory body is a major barrier in using this technology to create pharmaceutical formulations.

1.3.3.5. 3D printing and sustainability

In recent years, the issue of sustainability has become a focus in international debate, following growing evidence of how human activity is increasingly impacting the environment, availability of energy resources and raw materials, and how they are used.

Sustainability is also becoming a focal point for the pharmaceutical industry, to improve the longevity and social perception of the industry (78). In this scenario, by analyzing the current major industrial production techniques in the manufacturing industry, it is clear that 3D printing could represent a new approach for the increased sustainability in pharmaceutical production as well as in other areas of manufacturing (79). Since the design is determined before printing (78) and the technique focus on creating it layer-by-layer, minimizing the material used, the 3D printing technique produces a negligible amount of waste material compared to traditional ones (80,81). Furthermore, 3D printers allow it to print hollow structures with great mechanical resistance, avoiding the use of excess material. However, printing failure, which can be caused by an inadequate design of the object to be printed or the wrong selection of materials, can lead to defective or unsuitable object.

On the other hand, as mentioned in *Section 1.3.3.1.*, 3D printing allows the development of personalized medicines, where drugs can be tailored to individual patient needs. This can lead to more effective treatments, reducing the overuse of medications and minimizing adverse effects. In addition, it should be noted that this technique can produce medicines on-demand, helping pharmaceutical companies to produce as needed, reducing the need for an excessive inventory that might expire or go to waste. Another of their many advantages is that 3D printers are very efficient and allow shorter production times, producing more in less time and, in turn, using fewer energy resources (81). Some 3D printing techniques, such as PAM, enable the direct use of the starting material to print a certain pharmaceutical form, avoiding the handling that is usually carried out in traditional pharmaceutical techniques. It is also important because of the possibility of reducing the use of solvents, particularly organic solvents, which represent between 80 % and 90 % of all materials used in manufacturing processes and they are considered among the products with the greatest impact on the environment (78).

While 3D printing offers several sustainability advantages, there are still challenges to address. For instance, the environmental impact of the materials used in 3D printing, such as some polymers or resins, needs to be evaluated. In the various applications of 3D printing, non-biodegradable materials are very often used, as they provide better mechanical properties to the printed objects and greater inertness which allows for long-lasting prints. Unfortunately, these materials are not eco-friendly, hence the need to investigate how materials of natural origin and biocompatible materials can be employed in 3D printing more successfully (82). According to the focus on

sustainability, the exploring of natural-derived and renewable biopolymers (e.g. cellulose, lignin, starch, alginate and derivatives) for products fabrication by 3D printing has gained extraordinary attention. Its use not only represents a fundamental step towards sustainability, but reduces the limitations associated with synthetic polymers (83).

As the technology continues to evolve and as regulations and best practices in sustainable manufacturing develop, 3D printing is likely to play an increasingly significant role in sustainability in the pharmaceutical industry. Adopting these practices can lead to more efficient, patient-centric, and eco-friendly pharmaceutical manufacturing.

1.3.3.6. 3D printing technology in Europe

The global market for 3D-printed medical devices is expected to reach 1469.4 million USD by 2026, with plastic being the most used material for AM in medical devices. Biomaterial inks are forecasted to grow substantially in the next decades, reaching up to 20% in total market share by 2026. Inkjet and polyjet technologies are expected to peak in the next 9 to 10 years (84).

Europe has a leading position on the medical devices market, followed by North America, accounting for over 40% of the global market share in 2016. The European industry for medical devices is an important employer in the region, with 25,000 companies employing 575,000 people in 2010.

Large-scale manufacturing using 3D printing technology has not yet been fully developed in Europe. The main constraints identified are the lack of information about upstream and downstream processes, their impact on the final product, and the mechanisms to assure the necessary quality control processes. Europe has all the necessary assets and key players to take on large production volumes, including a strong and stable R&D environment, highly specialized companies, and educational institutions and required skills availability (84).

The European Union (EU) is focusing on enabling its industry to move to the higher end of the value chain and position itself on a competitive path that rests on more innovative and complex products. This involves focusing on integrated technologies with the potential to connect several Key Enabling Technologies (KETs). The KETs Observatory aims to identify and describe promising KETs-based products and their value chains and recommend specific policy actions to help the EU industry stay ahead of global competition (84).

The value chain for 3D-printed medical devices is a hybrid structure that involves actors from various sectors, including software and 3D printer developers, metal and plastic industries, hospitals, and medical practitioners. The value chain is particularly complex due to critical production aspects and the multitude of professionals involved, such as medical practitioners, bioengineers, radiologists, designers, legal representatives, and health insurance. Europe has an emerging value chain for 3D-printed devices, which should be further developed and synchronized by accelerating the supply chain and setting up cross-regional partnerships working on networks of demonstrators. However, some constraints must be taken into account in the development of the value chain, among them: i) need for connection between value chain actors, ii) product development driven predominantly by technological advancements, iii) absence of large-scale manufacturing, iv) quality control processes and increasing importance for cybersecurity in AM medical devices. The demand for 3D printed medical devices is expected to grow substantially if we bear in mind the myriad of advantages that it offers to the geriatric population, a predominant age group. Moreover, the increasing prevalence of accidents by modernization and fast-paced machines in combination with the frequent occurrence of chronic diseases are also likely to boost the market for 3D printed solutions in medical devices.

Europe can be seen as one of the most important players in the field of 3D-printing in medical devices. Taking into consideration the expected growth in production, a positive impact on the competitiveness of European SMEs and employment could be envisaged. Although it is hard to predict the precise developments in the future, stakeholders are confident that Europe will continue to play an important role in the large-scale manufacturing of 3D-printed devices. These expectations are backed up by market research, suggesting that Europe will double its production by 2025-2030 (85).

2. OBJECTIVES

The aim of the thesis was the design and development of biocompatible starch-based patches for wound treatment. The selection of natural materials allowed to solve issues derived from synthetic materials (toxicity, biocompatibility, contamination). The project involves the production of the planned formulations using 3D printing, enabling the production of customizable patches, ease to manage and minimal expense, and for that purpose, the attention was focused on the two techniques Pressure Assisted Microsyringe (PAM) and Fused Deposition Modeling (FDM). The work has been divided in two parts, as described below.

Pressure Assisted Microsyringe (PAM) 3D Printing.

- Selection, of the raw materials;
- optimization of the hydrogel composition suitable for 3D printing and characterization;
- optimization of PAM 3D printing parameters suitable for the developed hydrogel;
- production and characterization of the printed patches.

TPS filaments optimization suitable for FDM printing.

- Selection of the most suitable composition for FDM 3D printing;
- production of the filaments by hot melt extrusion;
- characterization of the filaments;
- optimization of 3D printing parameters;
- production of some patch prototypes by FDM.

3. Pressure Assisted Microsyringe 3D Printing

3.1. Pressure Assisted Microsyringe (PAM) 3D Printing.

The selection of the most suitable polymers for patch production was performed among the natural polymers useful in health field in order to prepare a formulation safe for both people and environment according to one-health concept. Considering this, starch, β -glucan (β glu) and sodium hyaluronate (NaHy) were selected. The characteristics and properties of these fundamental components used for the development of films are briefly gathered below.

Starch is a natural biopolymer composed of two glucose polymers, a 20-30% amylose (water soluble part) and a 70-80% amylopectin (water insoluble part). Amylose is a linear polymer, with three-dimensional helical structure, where basic units are linked by α -D-(1 \rightarrow 4) glycosidic bonds (**Figure 3.1**). It can form inclusion complex with a wide range of polar and nonpolar linear compounds. Amylopectin is a highly branched polymer composed of 2000 to 200,000 glucose units linked α -(1 \rightarrow 4) and α -(1 \rightarrow 6) glycosidic bonds. Branching in amylopectin leads to the formation of spongy reticular structure (86,87), as shown in **Figure 3.1**.

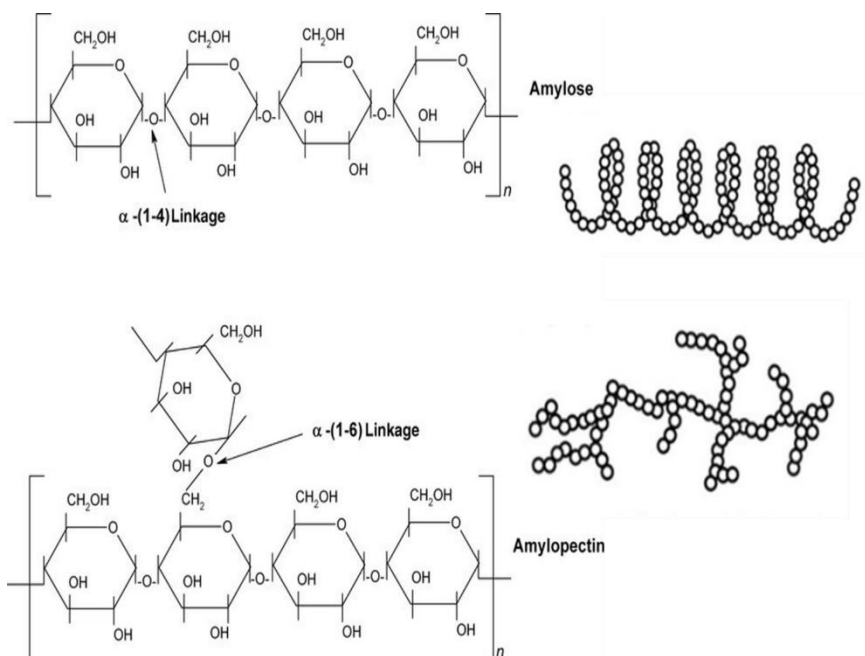


Figure 3.1. Starch structure. This figure was modified from Visakh P.M (88).

Starch is a raw material derived from an extensive variety of plants: cereals (corn, wheat, rice and barley), legume seeds (peas and pulses) and tuberculous sources (potato,

3. Pressure Assisted Microsyringe 3D printing

sweet potato, and vegetables). It is also found in many wastes and by-products deriving from food industry (89,90). Starch polymer has a wide range of properties, which can be tailored to meet specific needs through chemical and physical modifications. Starch is biodegradable, non-toxic, affordable product and possess many properties as good film-forming, adhesive, and thickening. Furthermore, it is already used in health products for many applications (i.e. excipients) as it is classified as generally recognized as safe G.R.A.S. substance by Food and Drugs Administration (FDA).

Starch-based products may exhibit several drawbacks, including poor mechanical characteristics and limited water resistance. Moreover, patches manufactured from this polysaccharide, in the absence of additives, may exhibit brittleness, which limit its use. However, it is possible to improve the mechanical properties and strength of starch-based products in several ways as:

- i) using modified starch derivatives;
- ii) adding plasticizers such as Glycerol (Gly) to improve strength;
- iii) using fillers to obtain composites with enhanced mechanical properties.

To this end, mixtures of starch with other raw materials can be considered.

Cornstarch (CS) (**Figure 3.2**) was chosen among different types of starch, because of its elevated amylose content (28%) and its suitability to create a well-organized and uniform gel. CS is a white, odorless, and tasteless powder useful in the manufacturing of paper, industrial adhesives, food processing and a variety of pharmaceutical products (91).



Figure 3.2. Image of corn plant (left) and CS powder (right).

Barley (*Hordeum vulgare L.*) (**Figure 3.3**) is an important cereal crop ranking fourth among the total cereal production but very little of this grain is used as human food. It is currently gaining popularity as a “functional grain” because it contains high amounts of bioactive compounds, including β glu among others. β glu is acknowledged as a functional and bioactive food ingredient due to its biological activities, like (92–94). In this context, β glu was considered as a potential filler to improve the mechanical properties of CS.

β glu is a polysaccharide composed of *D*-glucose units that are polymerized primarily via the β -(1 \rightarrow 3) glycosidic bonds, in addition to the β -(1 \rightarrow 4) and/or β -(1 \rightarrow 6) bonds. It is widely present in cereals (as barley and oat), yeast, some bacteria, mushrooms and algae. Barley β glu includes a mixture of β -(1 \rightarrow 3) and β -(1 \rightarrow 4) glycosidic bonds without β -(1 \rightarrow 6) branching (**Figure 3.3**).

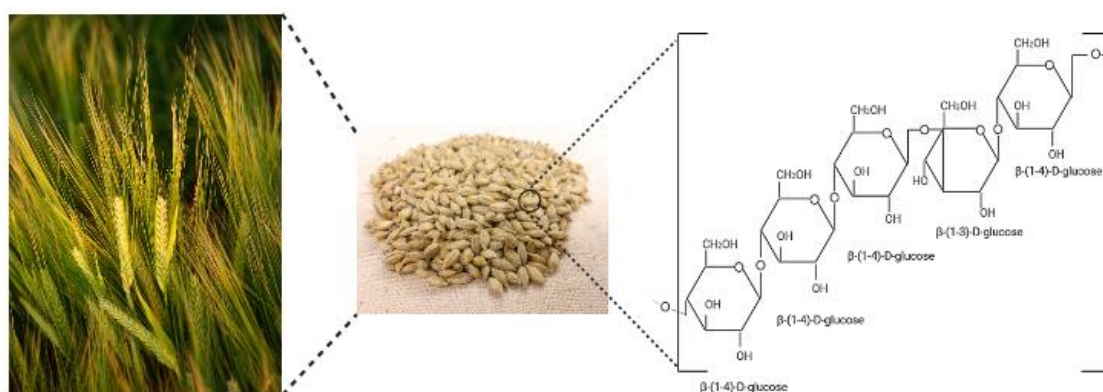


Figure 3.3. Image of *Hordeum vulgare L.* (left) and barley grains (left) (95). Barley β glu structure: β -(1 \rightarrow 3) and β -(1 \rightarrow 4) glycosidic bonds (right).

β glu can be divided in water soluble and insoluble components. In this regard, the water-insoluble part of β glu has been studied to treat gastrointestinal pain and chronic constipation, while the water-soluble β glu is considered as a potent immunity booster. Among the already mentioned therapeutic activities, β glu can also be useful in the dermatological field. In fact, this substance has been used in different formulations (such as creams, ointments, and suspensions) for several decades as a general protection. Interestingly, it increases collagen production and reduces eczema, psoriasis, and other skin diseases. β glu was found to be a film forming humectant and a promoter of wound healing (92). In addition, β glu is an interesting molecule because of its gel forming and

thickening properties, which allow to obtain a gel with a suitable consistency for extrusion in 3D printing (96).

Finally, sodium hyaluronate (NaHy) was selected. NaHy is a glycosaminoglycan (long sugar chain) biopolymer extensively used for biomedical applications due to its biofunctionality, biocompatibility, biodegradability and non-immunogenicity (97). NaHy chemical structure consist of a repeating disaccharide unit of D-glucuronic acid and N-acetyl-D-glucosamine linked by β -(1 \rightarrow 4) and β -(1 \rightarrow 3) glycosidic bonds (**Figure 3.4**).

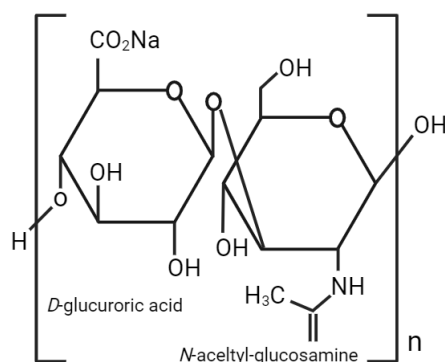


Figure 3.4. NaHy chemical structure.

In the field of topical applications NaHy is used as a dermatological ingredient (as moisturizers, filler, mattifying, soothing) and as wound healing because of its capability to promote skin regeneration (98). The chemical, physical and physiological characteristics of NaHy highly depend on its molecular weight and concentration (99). High Molecular Weight (HMW) NaHy ($\geq 10^6$ Da) inhibits endothelial cell growth, thus acting as an anti-angiogenic molecule. It is also the main lubricating agent in the synovial joint fluids, and it has beneficial roles in inflammation, tissue injury repair, wound healing and immunosuppression thanks to its fibrinogen binding ability and ability to modulate the recruitment of inflammatory cells, levels of cytokines and cell migration (98,100,101). Low Molecular Weight (LMW) NaHy (2×10^4 - 10^6 Da) shows pro-angiogenic and pro-inflammatory activities, stimulating cytokines, growth factors and chemokines expression. This type of NaHy can also induce tumor progression and ECM remodeling (99,100).

Some studies (102,103) highlight the use of NaHy not only for its therapeutic activity but also for its ability to modify the properties of other polymers and the final

viscosity of formulations. When mixed with other polymers, the chemical and physical characteristics of the resultant hydrogels highly depends on NaHy molecular weight and concentration. HMW NaHy at high concentrations leads to the reinforcement of the 3D polymer network structure and consequent increase of solution viscosity and viscoelasticity (101). Due to the greater complexity of the resultant 3D network, the mechanical strength of the hydrogel may also increase, which is crucial for 3D printing. In fact, some authors (104) have already highlighted the direct relationship between HMW NaHy and the final rheological properties of hydrogels: the presence of HMW NaHy induces steeper shear thinning slopes and better post-print shape retention with respect to LMW NaHy. This makes HMW NaHy hydrogels better candidates for extrusion-based 3D printing. It has been reported that as NaHy molecular weight increases a smaller amount polymer content is needed to achieve optimal 3D printability (105). According to this, some studies claim that HMW NaHy gels are of great usefulness for 3D printing. Specifically, NaHy-based gels with molecular weights ranging between 120 and 2500 kDa and concentrations ranging from 0.1% to 4% w/v, have provided good mechanical properties during 3D printing, together with excellent biocompatibility and biodegradability (106). In view of the properties, activity, and origin of NaHy, as well as the current state of the art, a HMW NaHy (800 kDa) was selected.

3.2. Materials

CS and Gly were supplied by A.C.E.F. s.p.a. (Fiorenzuola d'Arda, Italy). Sodium alginate (Alg), ethanol 96% (EtOH), were acquired from Sigma-Aldrich (Milano, Italy). Barley seeds (cultivation in Monteleone of Spoleto, Perugia, Italy) were purchased from Antica Spezieria Bavicchi (Perugia, Italy). Calcium chloride (CaCl_2) was purchased from Carlo Erba (Milano, Italy). NaHy MW 800 kDa was obtained by Altergon (Avellino, Italy). Ultrapure water was obtained by reverse osmosis process in a MilliQ system Millipore (Rome, Italy). Other reagents and solvents were of analytical grade and used without further purification. The simulated wound fluid (SWF, pH 6.5) was prepared by dissolving 8.30 g of NaCl and 0.28 g of CaCl_2 in 1000 ml of ultrapure water.

For biological studies, the test media were prepared as follow:

- Mueller-Hinton agar (MHA); deionized water, Mueller-Hinton agar (3.8 w/v; Oxoid Limited, Basingstoke, UK); pH 7.3 ± 0.2 , 25°C.
- Mueller-Hinton agar 5% defibrinated sheep blood (MHAB): deionized water, Mueller-Hinton agar (3.8% w/v; Oxoid Limited, Basingstoke, UK), defibrinated

sheep blood (5% v/v; Allevamento Blood di Fiastra Maddalena, Teramo, IT; pH 7.3 ± 0.2 , 25°C).

3.3. Methods

3.3.1. Hydrogels formulations

Starch-based hydrogels were formulated from the glycerol gel (starch glycerolate) monograph contained in the Farmacopea Ufficiale Italiana (F.U. XII Ed.). The modification consisted in the addition of a filler in order to improve the strength of the final hydrogels. Six different formulations were prepared (**Table 3.1**).

Table 3.1. Hydrogels composition.

Hydrogels	CS% (w/w)	Gly% (w/w)	water% (w/w)
G1	10	60	30
G2	10	50	40
G3	10	40	50
G4	10	30	60
G5	10	20	70
G6	10	10	80

The hydrogel was prepared as follows: CS was dispersed under magnetic stirring (600 rpm) in Gly/water mixture at 80 °C, until gelation. The resultant white, consistent and homogeneous semisolid hydrogel was then put into a sterile, 60-catheter cone syringe suitable for PAM extrusion and left to cool at room temperature (R.T) for 24 h in order to promote the removal of air bubbles incorporated during the preparation. In this period, they completely disappear as they spontaneously left the formulation (107).

The β glu suspension (β glu content 6.30 ± 0.70 g/100 g) was prepared according to a previous work (92). Briefly, barley grains were grounded in a knife mill GRINDOMIX GM 200 (Retsch, Predengo, Cremona, Italy) working at 4000 rpm for 3.30 min. The obtained flour was sieved by stainless steel sieves (Endecotts Ltd., London, UK) to select the fraction with a size range of 400–500 μ m. According to literature (108), this selected fraction was boiled in EtOH (80%, v/v) under reflux for 2 h in order to inactivate β -gluconases enzymes responsible for β glu enzymatic hydrolysis. Thereafter, the suspension was centrifuged (Hettich zentrifugen, Universal 32R) for 10 min at 4000 rpm, 20°C, to remove EtOH. A total of 150 ml of water was added to the solid and was treated

3. Pressure Assisted Microsyringe 3D printing

by a high-power ultrasonic (HPU) transducer (emitted power of 750W; transmitted power of 200W, frequency of 20 KHz, amplitude of 50%) working at 55 °C for 15 min, and equipped with a Horn 330 Type ultrasonic probe VCX750 (SONICS, Newtown, CT, USA). Then, the obtained suspension was centrifuged (10 min, 4000 rpm, 20 °C) and the supernatant was collected. The solid was re-dispersed in 150 ml of water to repeat the HPU treatment for other 2 cycles. A total of 3 cycles were performed (**Figure 3.5**).

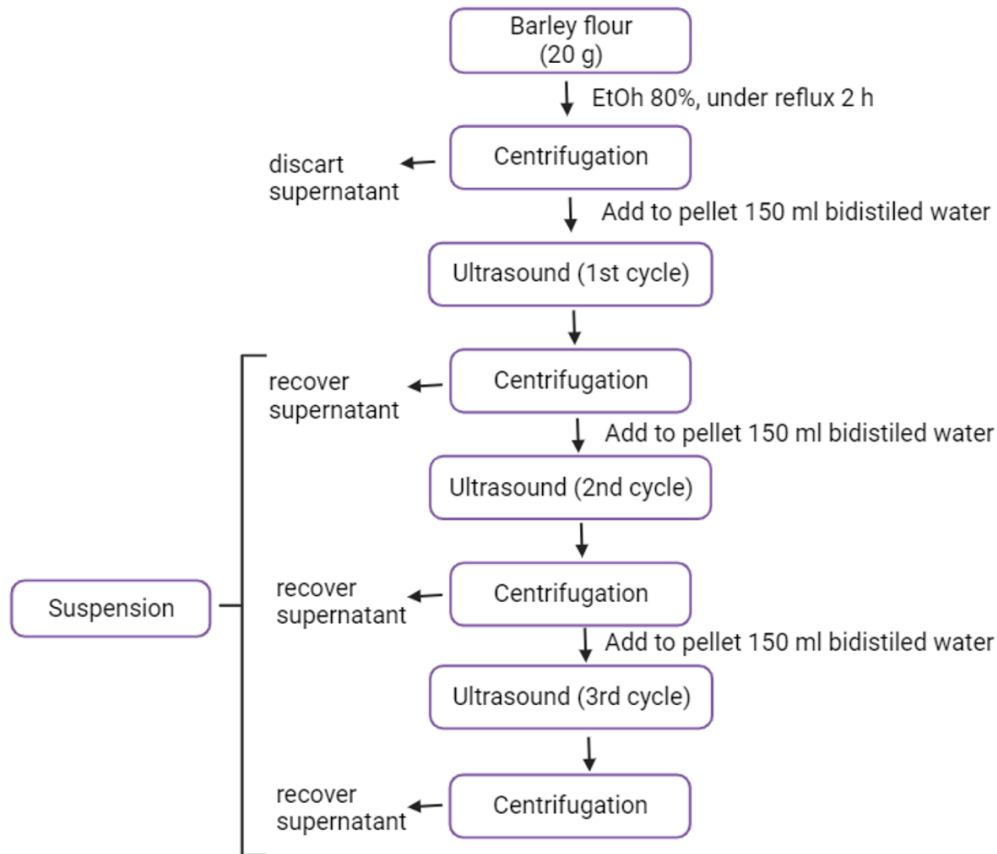


Figure 3.5. Extraction process of β glu from barley flour.

Considering that the amount of filler generally useful to improve the mechanical properties of polymeric patches is 1% w/w (corresponding to β glu suspension 43.72% w/w) (109), this percentage of β glu was included in the formulation (**Table 3.2**).

Table 3.2. Hydrogels prepared using β glu as filler.

Hydrogels	CS% (w/w)	Gly% (w/w)	β glu suspension% (w/w)	water% (w/w)
G3- β glu	10.00	39.00	43.72	7.28

3. Pressure Assisted Microsyringe 3D printing

G4- β glu	10.00	29.00	43.72	17.28
G5- β glu	10.00	19.00	43.72	27.28

The hydrogels were prepared following the procedure described by Valencia et al. and Perotti et al., properly modified (110,111).

The filler, represented by a water suspension of β glu, was dispersed in water under magnetic stirring (600 rpm) for 30 min at R.T. Then, Gly was added under magnetic stirring (600 rpm) for 15 min at R.T. The dispersion was warmed at 80°C before the addition of 10% w/w CS and left to stir with a magnet (600 rpm) at 80°C until gelation (~7 min). The obtained hydrogel was then put into the sterile, cone printing syringe (suitable for PAM extrusion) and left to cool to the standardized conditions (R.T. for 24 h (107)) (Figure 3.6).

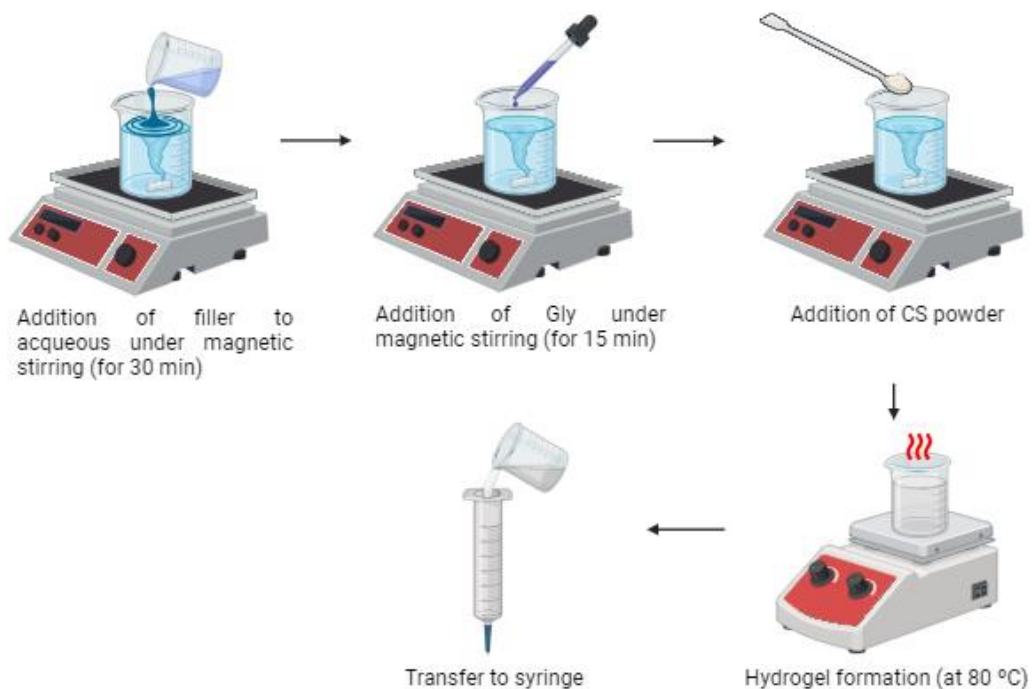


Figure 3.6. Schematic representation of the CS hydrogel preparation method.

The hydrogels containing NaHy were prepared using the materials and quantities shown in the **Table 3.3**. NaHy was initially added to β glu suspension under magnetic stirring (600 rpm) for 30 min and then, Gly was added under magnetic stirring (600 rpm) for 15 min at R.T. Then, CS was added to this mixture and heated at 80 °C until hydrogel

3. Pressure Assisted Microsyringe 3D printing

formation. Finally, it was transferred to the sterile conical impression syringe and left under the same conditions as above (R.T. for 24 h) (**Figure 3.7**).

Table 3.3. NaHy based hydrogels composition.

Hydrogels	CS% (w/w)	Gly% (w/w)	β glu suspension% (w/w)	water% (w/w)	NaHy% (w/w)
NaHy-H1	10.000	29.000	43.720	17.185	0.095
NaHy-H2	10.000	29.000	43.720	17.090	0.190
NaHy-H3	10.000	29.000	43.720	16.900	0.380

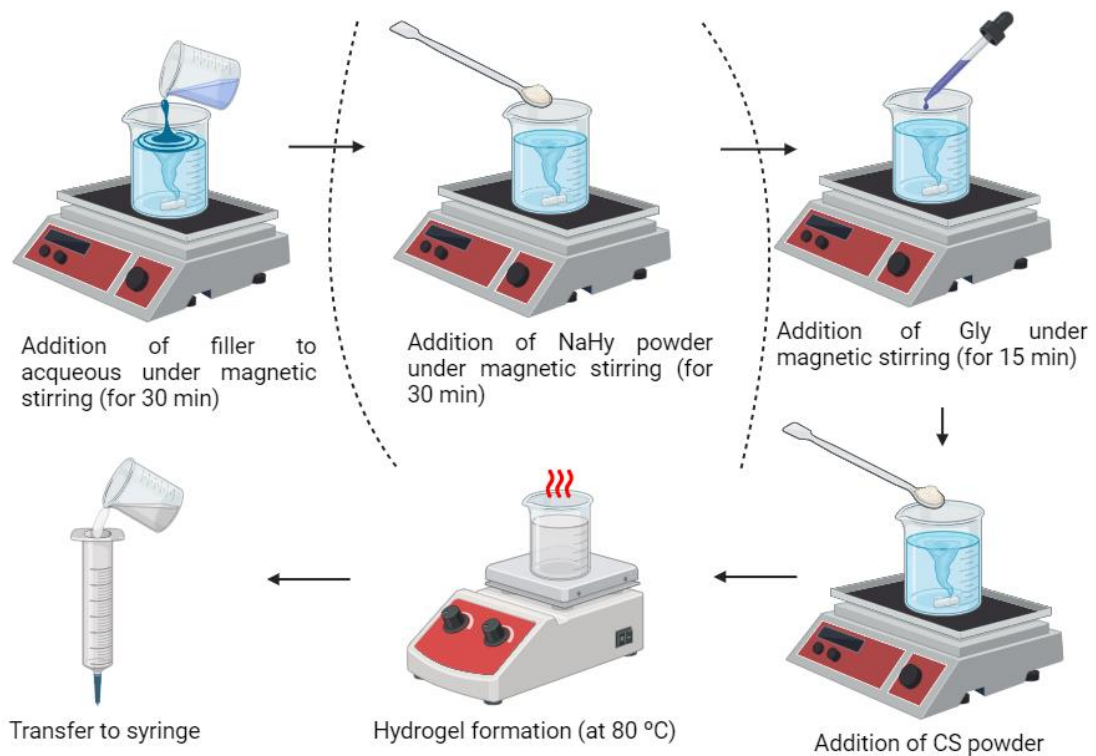


Figure 3.7. Schematic representation of the CS hydrogel preparation method containing NaHy.

3.3.2. Rheological measurements

Rheological tests of the most suitable hydrogels were carried out by using a rotational rheometer (Scientific's Ares model) with parallel flat plate geometry (diameter

3. Pressure Assisted Microsyringe 3D printing

25 mm). Mode: Dynamic Rate Sweep Test (RST), Transient Step Rate Test (SRT), and Dynamic Temperature Step Test (DTSt). The experiments were performed in triplicate; each result represents the average of the three measurements (n=3).

3.3.3. Patches preparation

3.3.3.1. Selection of printing parameters and design

Rectangular patches having 10 cm × 2 cm dimensions were designed by CAD software (OnShape education) and exported as .stl file. The .stl file was then imported into a slicer software (Ultimaker Cura 4.13.1.) in which printing parameters, such as the layer height, print speed, infill percentage, and flow rate, were pre-established (**Table 3.4**).

Table 3.4. Studied printing settings.

Parameters	Values	Units
Nozzle diameter	0.80-1.62	mm
Layer height	0.2-0.6	mm
Flow rate	30-80	%
Volumetric flow rate	1.5-48.2	mm ³ /s
Print speed	10-30	mm/s
Infill density	60-100	%

Patches were prepared using selected hydrogels by extrusion-based 3D printing technique PAM by means of a customized Creality 3D Ender-3 V2 (Shenzhen Creality 3D technology Co., China) equipped with syringe extruder (**Figure 3.8**).

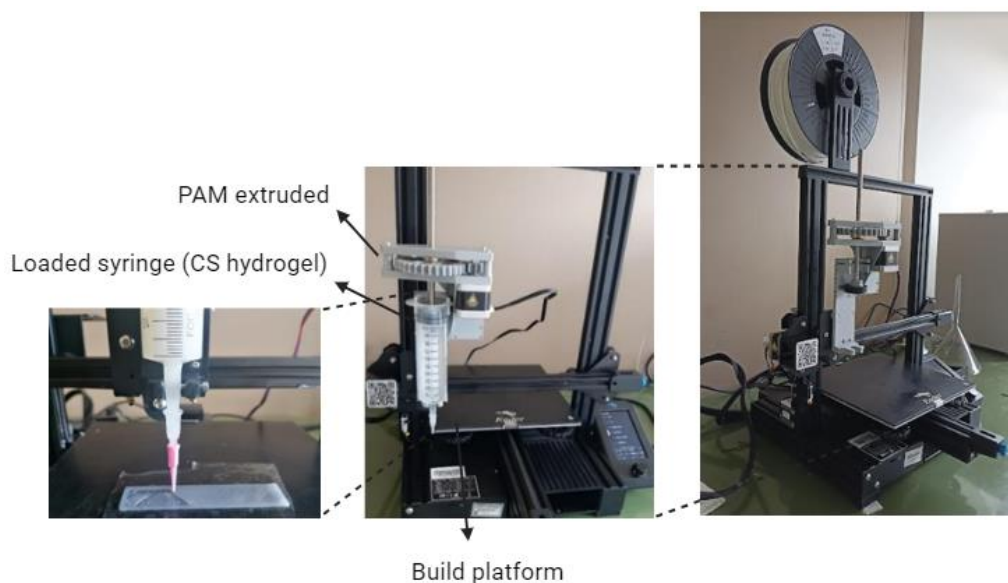


Figure 3.8. Creality 3D Ender-3 V2 modified for 3D printing by PAM technique.

The hydrogels were printed on different supports, namely Teflon (PTFE), plastic (PET), and silicone. The wet patches were then dried at different temperatures (37°C, 40°C, and 70°C) and for different times (12 h, 16 h, and 24 h) in order to optimize the post-processing conditions. All the dried patches were then conditioned at R.T. under two different relative humidity (RH) conditions: 40% RH under CaCl₂ and 37% RH under SiO₂.

Nozzle diameter

The selection of the most suitable nozzle diameter (syringe tip) was performed on the basis of (i) hydrogel consistency, (ii) hydrogel rheological behavior, and (iii) quality of the printed material (112). Different nozzle diameters, from 0.80 mm to 1.62 mm, were evaluated to extrude the material.

Infill density

The infill refers to the internal structure of the 3D object, which can have different patterns and shapes; the infill density is a percentage value of the volume of material present in each layer that fills the inner part of the print. If the infill is 100%, the internal structure is full, while setting the infill to 0% will result in the object being empty.

Flow rate

The flow rate indicates the speed at which the printer extrudes a given amount of material; this parameter influences many other factors, such as the printing speed, the under- or over- extrusion of material, adhesion to the substrate, and line width. This parameter controls the speed at which the filament is extruded (filament flow through the nozzle), thus indicating the printer how much of the filament cross-sectional area should be extruded per unit time. In the slicer software it is expressed as a percentage value relative to the full extrusion rate, and it has been optimized by ranging from 30% to 80%. From this value, it is possible to retrieve the exact volumetric flow rate as described in Equation (Eq.) 3.1. A low flux value is usually related to deposition of less material and so, higher resolution, while high values can lead to the formation of surfaces with low resolution due to excessive material deposition.

Volumetric flow rate

The volumetric flow rate (VFR) through the printer nozzle is calculated from the pre-set print speed, that is, the speed at which molten material is deposited from the

syringe nozzle to the platform. The volume flow rate, Q , can be calculated using the radius of the nozzle, r , and the printing speed, v :

$$Q = \pi r^2 v (f_r/100) \quad \text{Eq. 3.1.}$$

Print speed

The printing speed represents the distance that the nozzle travels in a determined amount of time, normally expressed as mm/s. Different print speeds were evaluated in a range from 10 mm/s to 30 mm/s, and the selection of the set value was made considering the best hydrogel extrudability. The printing speed was also adjusted on the basis of the characteristics of the printed layer.

Material extrusion rate (MER)

The MER is the amount of material extruded at different printing speeds when a specific pressure is applied through a nozzle of fixed dimension; it is expressed in mg/min. In order to design and develop customized suitable patch, the optimization of the material extrusion rate is required since it determines the amount of extruded material in unit time, thus affecting other parameters like the final resolution.

Optimization of post-printing process

The 3D printing of the extruded hydrogel was carried out on different backing materials including PTFE, PET, silicone, to study the impact of the backing on i) the material spreadability, ii) the integrity iii) and homogeneity of the final product. The backing for printing is also important to determine post-printing process conditions as temperature and drying time. Monolayer patches (0.2 mm total thickness), bi-layered patches (0.4 mm total thickness) and three-layered patches (0.6 mm total thickness) were prepared in an attempt to define the most suitable final structure.

3.3.3.2. Backing layer preparation

The backing layer was prepared by the casting method using alginate according to a previous work (113). The exact composition was Alg 1.5% w/w, Gly 10% w/w, water 88.5% w/w. The preparation of this mixture to form the patch backing layer was carried out under magnetic stirring (600 rpm) for 90 min. Alg gel (385 ml) was casted in plastic backing (24 × 34 cm) and dried in oven at 37°C for 50 h. Afterwards, it was immersed in a solution of CaCl₂ at 5% w/v for 3 min in order to promote Alg polymerization, which was subsequently dried in an oven at 37°C for 24 h. The obtained film was washed with

water to remove the excess of CaCl_2 and finally dried at 37°C for 24 h, as shown in **Figure 3.9**.

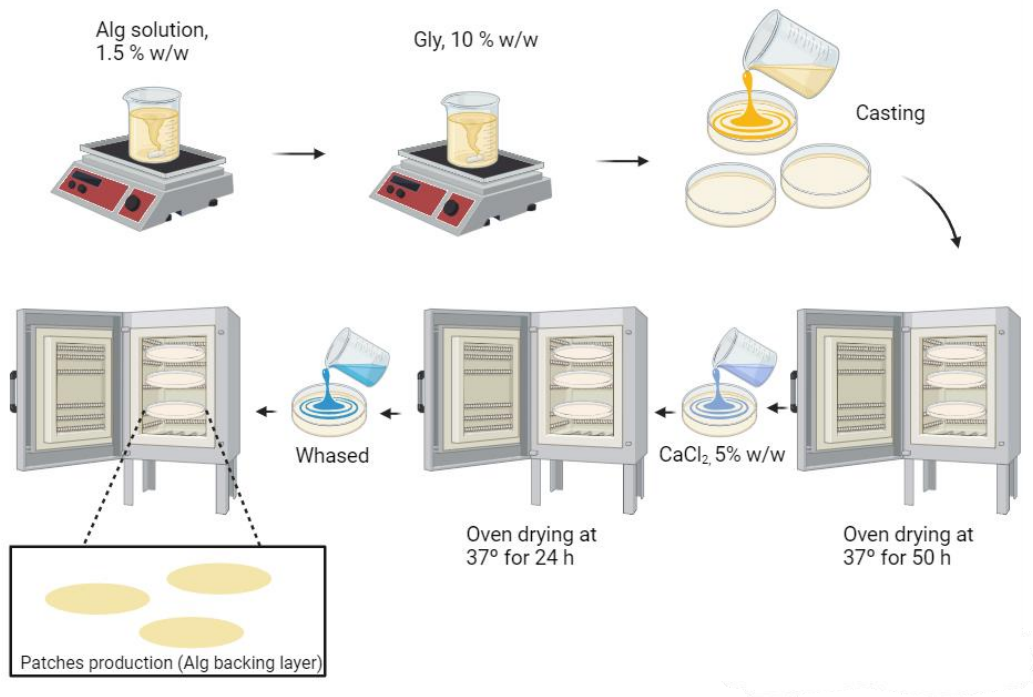


Figure 3.9. Production of the Alg backing layer by solvent casting.

3.3.4. Patches characterization

Scanning Electron Microscopy (SEM)

The morphology and thickness of the printed patches were investigated by Scanning Electron Microscopy using an FE-SEM LEO 1525 ZEISS (Carl Zeiss Microscopy, Jena, Germany). The sample was deposited on conductive carbon adhesive tape, and metallization with chromium (8 nm) by sputtering was carried out. The images were acquired by means of In-lens detector with an electron high tension (EHT) of 5 kV.

Thermogravimetric analysis

Thermal stability of the produced patches was determined by thermal gravimetric analysis by using a TG/DTA Seiko 6300 (Seiko Instruments, Torrance, CA, USA). Each patch was cut in similar portions (weight 10 mg) and placed inside small alumina crucibles. Analyses were carried out by heating the samples between 30 and 900°C at $10^\circ\text{C}/\text{min}$, nitrogen flow at 250 ml min^{-1} .

Mechanical characterization

3. Pressure Assisted Microsyringe 3D printing

Tensile tests were determined by using a digital microprocessor instrument (Lloyd LR30K, Lloyd Instrument, Fareham, UK). The patches were cut in portions 100 mm × 10 mm (UNI ISO 527) to have a useful length of 50 mm. The experiment was performed at 5 mm min⁻¹, cell load 50 N. The two ends of the patch were fixed with clamps to the dynamometer. The sample was subjected to tensile stress until deformation and break. Values for elastic modulus (E), stress, and deformation at break (σ_b and ε_b) were registered. The obtained data are an average of five measurements (n=5). The formulations were stored at R.T. for 1 week under vacuum conditions and in oversaturated calcium chloride (CaCl₂) solution.

Fourier-Transform Infrared Spectroscopy (FT-IR)

Infrared (IR) spectra of the samples and all their components were registered by a Shimadzu IR Spirit QATR-S spectrometer (Kyoto, Japan). QATR-S is a single-reflection ATR measurement attachment. Spectra were registered from 400 to 4000 cm⁻¹ with a resolution of 2 cm⁻¹.

Swelling Capacity

Patches swelling properties and erosion were evaluated by determining the hydration percentage (%) and matrix erosion or dissolution percentage (DS %) calculated using **Eq. 3.2** and **3.3** respectively:

$$\text{Hydration \%} = \frac{W_2 - W_1}{W_2} \times 100 \quad \text{Eq. 3.2.}$$

$$\text{DS \%} = \frac{W_1 - W_3}{W_1} \times 100 \quad \text{Eq. 3.3.}$$

Each patch was cut in portions of 2 cm² (1 cm x 2 cm) and a single portion was weighted (W₁), immersed in SWF (1 ml) in an Eppendorf (2 ml Corning, Torino, Italy) and held at 32.0 ± 0.1 °C for established times (1, 2, 3, 4, 5, 6, 24, 48 h). After immersion, the patches were wiped from the excess of SWF using filter paper and weighted (W₂). Then the patches were dried at 60 °C for 24 h and kept in desiccator over CaCl₂ at 40 % R.H. for 48 h and reweighted (W₃). The obtained results represent the average of three measurements (n=3) (114).

Contact angle

3. Pressure Assisted Microsyringe 3D printing

The water contact angle of the printed patches was evaluated using the sessile drop method. Contact angles of the drops (FTA 1000, First Ten Angstroms, Newark, CA, USA) were measured at R.T. under static conditions on pressed glass plates of powdered materials; the measurement values represent the mean value of 10 drops. The analysis was estimated by measuring the angle of a 20 μ l deionized water sessile drop on the disc surfaces.

3.3.5. Biological activity

Antimicrobial activity assay

The antibacterial activity of the samples was evaluated against 15 strains, including Gram + bacteria, Gram - bacteria and yeasts.

The experiments were performed using agar well diffusion technique (24,25). For each organism an initial suspension of 0.5 McFarland in 0.9% sterile saline solution was prepared and 100 μ l were distributed on MHA/MHAB plates by a swab. Then, each patch was placed on the inoculated plates which were incubated according to the growth conditions shown in **Table 3.5**. After the incubation time, the presence of the inhibition halo was evaluated and its diameter was measured by a gauge.

Table 3.5. Bacterial strains tested and growth conditions.

	Strain	Growth Conditions
GRAM + bacteria	<i>Staphylococcus epidermidis</i> WDCM 00036	37 °C for 24 \pm 2 h
	<i>Enterococcus faecalis</i> WDCM 00087	37 °C for 24 \pm 2 h
	<i>Bacillus subtilis</i> WDCM 00003	30 °C for 24 \pm 2 h
	<i>Staphylococcus aureus</i> WDCM 00034	37 °C for 24 \pm 2 h
	<i>Streptococcus pyogenes</i> ATCC 19615	37 °C for 24 - 48 h
GRAM - bacteria	<i>Pseudomonas aeruginosa</i> WDCM 00025	25 °C for 24 - 48 h
	<i>Klebsiella pneumoniae</i> WDCM 00097	37 °C for 24 \pm 2 h
	<i>Proteus mirabilis</i> WDCM 00023	37 °C for 24 \pm 2 h
	<i>Escherichia coli</i> WDCM 00013	37 °C for 24 \pm 2 h
Yeast	<i>Candida</i> CM 00054 <i>albicans</i> WD	25 °C for 24 - 72 h

The experiments were performed using the agar-well diffusion technique, properly modified, with a test medium (pH 7.2) prepared according to the recipe previously described (see *Section 3.2.*). After preparation, the test medium was autoclaved. After cooling at 45 - 48°C, 1 ml of bacterial suspension was added reaching a final concentration of 1×10^5 CFU/ml. Different inoculated media were used for each

bacterial strain. The suspensions were accurately mixed and poured (20 ml) into Petri dishes (90 mm diameter) and let to cool on a horizontal surface. Indeed, 100 μ l of products were placed in a hole of 13 mm in diameter, previously made in the center of cooled agar. The plates were incubated according to the growth conditions shown in **Table 3.5**.

For each bacterial strain, each product was tested and three inoculated agar plates were incubated to verify medium sterility. At the end of the incubation, the presence and the diameter of the inhibition halo was evaluated by a gauge.

Cell Viability - MTT Assay

The human immortalized keratinocyte cell line HaCaT, purchased from I.Z.S.L.E.R. (Istituto Zooprofilattico Sperimentale della Lombardia e dell' Emilia Romagna), was used as model to assess the epidermal homeostasis during wound treatment. HaCaT cellular viability was assessed after treatment for 24 h with the extract by MTT assay (115). To do so, the HaCaT cells were seeded onto a 96-well plate at a density of 1×10^4 cells/well with DMEM complete medium. After 24 h the medium was replaced by DMEM solutions containing different concentrations of the samples. After 24 h the “treatment solution” was withdrawn and replaced by DMEM medium containing 0.5 mg/ml of MTT reagent (which was previously dissolved in PBS 1X). After 3 h of incubation at 37°C, the supernatant was carefully removed, and formazan salt crystals (created by living cells in presence of MTT) were dissolved in 200 μ l dimethyl sulfoxide (DMSO) and added to each well. After 30 min the absorbance (OD) values were measured spectrophotometrically at 540.0 nm using an automatic microplate reader (Eliza MAT 2000, DRG Instruments, GmbH).

Each experiment was performed two times in triplicate. The cell viability was expressed as a percentage relative to that of the control cells as described in literature (116). A one-way ANOVA test was performed using GraphPad software (GraphPad Prism 9.2.0.332, GraphPad software, San Diego, CA, USA).

Scratch assay (In-vitro wound healing)

The on wound closure of β glu released from the patch was investigated by CytoSelect™ Wound Healing Assay Kit (Cell Biolabs, Inc., San Diego, USA). HaCaT cells were seeded into 24-wells tissue culture plate containing properly treated inserts ($5 \times 10^4/500 \mu$ l) in the plate wells with their “wound field” aligned in the same direction. These cells were incubated for 24 h in DMEM supplemented with 10% FBS to allow the cells adhere and reach the 80% confluence (117).

3. Pressure Assisted Microsyringe 3D printing

After removing the inserts from the wells, the medium was carefully withdrawn and the wells were washed twice with serum-free medium to remove dead cells and debris. Finally, the cells were treated with different concentrations of samples selected based on MTT results for further 6, 12 and 24 h.

Migration into the wound field was determined by using manual fixing with cell stain solution. To analyze cell migration, a picture for each scratch was taken at the same cell area after 6, 12 and 24 h of incubation. Representative microphotographs focused on the center of the wound field were taken (the wound area of the treated cells was observed). Three sets of experiments were performed. The influence of compounds on wound closure was compared to the control (untreated cells growing in DMEM supplemented with 10% FBS). A one-way ANOVA test was performed using the Graphpad program (GraphPad Prism 9.2.0.332, GraphPad software, San Diego, CA, USA).

Ex-vivo adhesion studies

Patches adhesion force was assessed using pig skin samples (from shoulder region) obtained from Large White pigs weighing ~165–175 kg, supplied by Veterinary Service of ASL N.1 Città di Castello (Perugia, Italy) and used within 12 h of pig death. The *ex vivo* adhesion force was measured by a dynamometer (Didatronic, Treni, Italy). The patch was attached to a support using cyanoacrylate glue and connected to the dynamometer Didatronic (Whatman GmbH, Dassel, Germany). A precise piece of porcine skin tissue was cut in a 4 cm diameter and fixed with cyanoacrylate glue on the surface of glass support, which was then placed in a thermostatic bath at $32.0^{\circ}\text{C} \pm 0.5$. Patches were printed in the same dimension and shape as the porcine skin by simply modifying the .gcode file, so that they could properly adhere to the skin sample. The free side of the patch was wetted with 150 ml of SWF and put in contact with the skin sample by applying a light force for 2 min (**Figure 3.10**). The force necessary for patch detachment from the skin was measured and expressed as an average of three measurements ($n = 3$) (118).

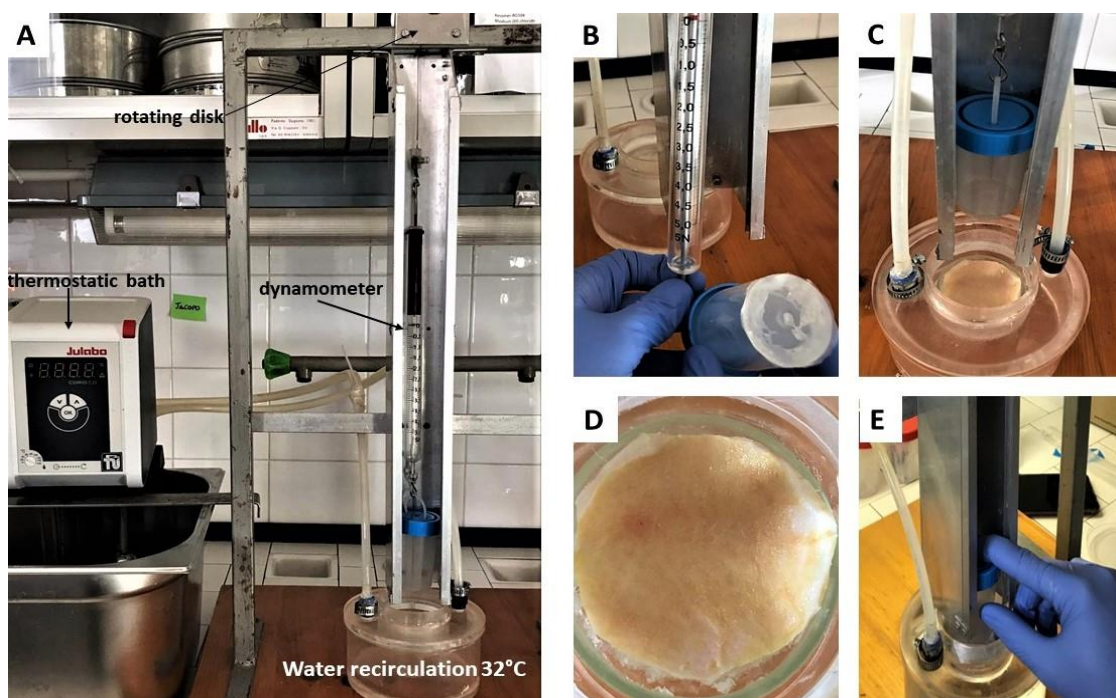


Figure 3.10. Experimental setup for *ex-vivo* adhesion studies.

3.4. Results and discussion

Monographs of many starch-based formulations for dermatological use are reported in the F.U. XII Ed. The starting point of this study was precisely the recipe of “Starch Glycerolate”, consisting of CS 10% w/w, Gly 70% w/w, and water 20% w/w properly modified. However, this gel was not suitable for PAM extrusion due to inconsistent flow through the printer syringe nozzle. Modified starch glycerolate compositions were so planned and studied aiming to improve the nozzle flow (**Table 3.1**).

Afterwards, the extrusion suitability through the printed syringe nozzle was evaluated. Formulations (see **Table 3.1**) G1 and G2 were too viscous (nozzle clogging), while G6 were too fluid (leakage from the syringe); for these reasons, these hydrogels were considered not suitable for printing and thus excluded. The remaining formulations, namely G3, G4 and G5 appeared to be more suitable for the purpose and were further characterized. A preliminary printing test showed that these three hydrogels did not enable the printing of a homogeneous object. During the extrusion, the object in process was cracked with consequent imperfections in the final object. Thus, a further modification of the compositions of hydrogels G3, G4, and G5 was made by including β glu as filler (**Table 3.2**) (119).

The extrusion ability of the resultant hydrogels was then evaluated. The dimensions and shape of the resultant product printed using both G3- β glu hydrogel and G5- β glu hydrogels did not correspond with the CAD design (printing fidelity). This is attributable to the consistency of the two hydrogels. G3- β glu hydrogel was probably too viscous due to low water content, while G5- β glu hydrogel was too fluid due to the high-water content. For this reason, G3- β glu and G5- β glu were excluded from the study. In the case of G4- β glu hydrogel, it was possible to obtain an object able to maintain the features set by CAD and, for this reason, considered suitable for the scope of the study.

As mentioned in the *Section 3.1.*, NaHy was considered as active ingredient with wound healing activity. Likewise, the concentration of NaHy must be optimized, reason why three different concentrations of NaHy were explored in order to obtain suitable hydrogels for PAM 3D printing (**Table 3.3**). The hydrogel with the highest amount of NaHy (NaHy-H3) caused nozzle occlusion due to extreme viscosity. In turn, the NaHy-H1 hydrogel demonstrated limited physical stability. In fact, after 24 h of storage at R.T., in static conditions (107) (the time standardized after hydrogel production to allow stabilization and air bubbles disappearance), a syneresis phenomenon was observed (presence of water on hydrogel surface). NaHy-H2 hydrogel showed good physical stability and suitable viscosity before 3D printing. Once the preliminary syringability studies were completed, the G4- β glu and NaHy-H2 hydrogels were selected.

The hydrogels that showed the highest stability for extrusion were deeply characterized and in the first instance, the rheological properties were evaluated.

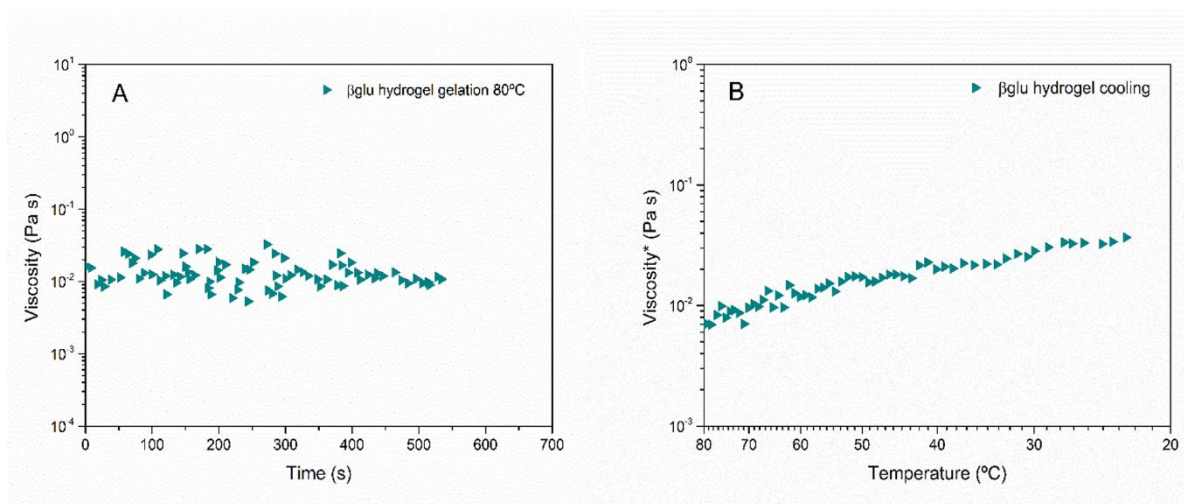
3.4.1. Rheology of hydrogels

The hydrogel flow properties (viscosity) have a significant impact on the quality of the final printed object (120). Generally, for PAM printing, it is preferable to use semisolid formulations having shear-thinning behavior, as it implies that the viscosity of the system will reduce as the external stress increases (extrusion in this case) without modifying the internal network of the hydrogel, so when the stress is removed the viscosity is recovered (49,52).

The G4- β glu hydrogel formation process at 80°C was evaluated by rheological analysis by SRT, and the rheogram (**Figure 3.11A**) shows a wide viscosity variability until 420 s (~7 min), when the viscosity values tend to be more consistent and almost constant with time, thus indicating hydrogel formation. Regarding the hydrogel cooling process studied by DTSt (**Figure 3.11B**) the viscosity increased as temperature decreased,

3. Pressure Assisted Microsyringe 3D printing

as a consequence of hydrogel consistency improvement during cooling. Since the hydrogel consistency varies as a function of temperature and even time, it is of particular interest to define this parameter after preparation and storage at a fixed time (24 h) and temperature (25°C) (107). As shown in **Figure 3.11C**, the viscosity profile of the gel after preparation, called G4- β glu fresh hydrogel, measured by RST analysis, was between 10^{-2} and 10 Pa·s in the shear rate range 10^1 – 10^{-1} s $^{-1}$ and it was not linear. This is ascribable to the necessity of a time of stabilization for the newly formed hydrogel. In fact, the viscosity measured for the same hydrogel stored at 25°C for 24 h was significantly higher in the shear rate tested and showed to be almost linear (**Figure 3.11C**). This result demonstrated the stabilization of the polymeric network and stresses the importance of the formulation process in the final performance of the hydrogel. Moreover, the decrease in viscosity as a consequence of shear rate increase is indicative of shear-thinning behavior, in which an increase in shear rates leads to polymeric chain alignment and an ordered structure. High shear rates imitate the extrusion of hydrogel via the nozzle, where viscosity reduction results in uniform extrusion (121). Therefore, the obtained results demonstrated the suitability of the G4- β glu hydrogel for PAM 3D printing.



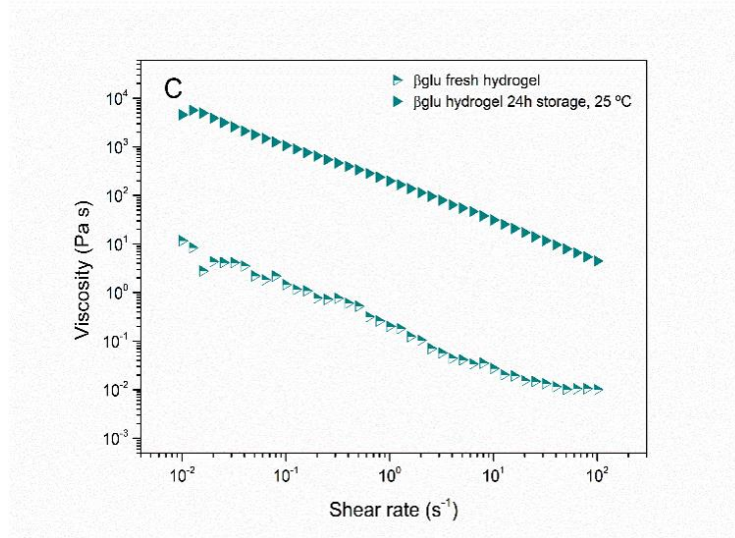


Figure 3.11. Rheograms of G4- β glu hydrogel (A) viscosity (Pa·s) vs. time (s) showing the gel formation at 80°C; (B) viscosity (Pa·s) vs. temperature (°C); (C) viscosity (Pa·s) vs. shear rate (s^{-1}) of the hydrogel just after preparation and after storage at 25°C for 24 h; (n=3).

Subsequently, the NaHy hydrogels were characterized, and a viscosity study was performed on all the hydrogels having different NaHy % (**Figure 3.12**), to determine their viscosity in comparison with the selected hydrogels (G4- β glu and NaHy-H2).

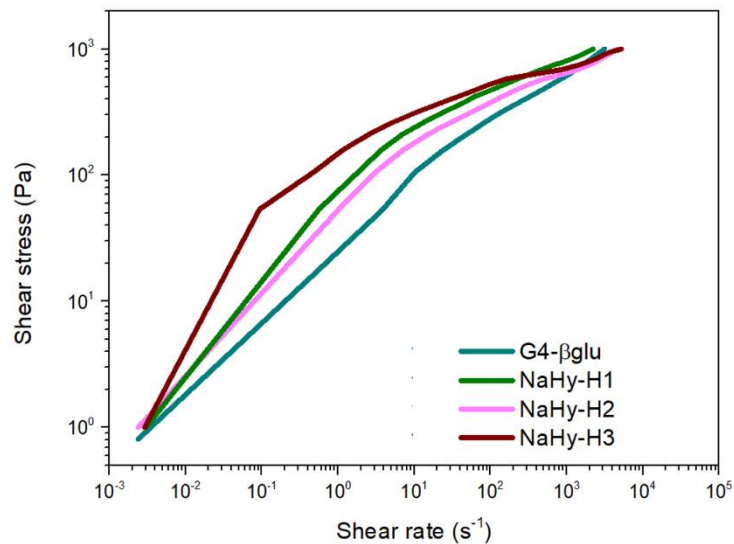


Figure 3.12. Rheograms (flow curves) of G4- β glu and NaHy hydrogels at different %. Shear stress (Pa) vs. shear rate (s^{-1}); (n=3).

3. Pressure Assisted Microsyringe 3D printing

The obtained flow curves showed pseudoplastic and shear-thinning behaviour for all the hydrogels with a shear rate in the range from 10^{-3} to 10^3 s^{-1} (**Figure 3.12**) (117). The increase of NaHy concentration produced an increase in the shear stress due to the higher number of polymer chains in the 3D polymer network of these formulations. In **Figure 3.12** NaHy-H3 shown to be the most viscous, confirming the a priori studies of syringability, followed by NaHy-H2 and NaHy-H1 showing a similar rheological profile. Nevertheless, the previous macroscopic studies showed that NaHy-H1 was not stable after standardized conditions (107) and it was discarded despite its adequate viscosity. Therefore, the rheological study was continued with the most suitable hydrogel (NaHy-H2).

For NaHy-H2, the hydrogel formation at 80°C was studied by SRT. As reported in **Figure 3.13A**, the moment when the time-dependent viscosity stabilizes starts at 450 s (~7.5 min). The result of DTSt analysis about hydrogel cooling process are reported in **Figure 3.13B**, showing that the viscosity decreases as the hydrogel cools (102) and that the viscosity decreases as a function of temperature as a consequence of hydrogel consistency improvement during the cooling (102).

The standardized method for PAM printing of G4- β glu hydrogel (107) suggested to keep the prepared hydrogel in static conditions 24 h before 3D printing. Taking this into account, the differences in viscosity of NaHy-H2 before and after 24h in static conditions at 25 °C were evaluated (**Figure 3.13C**).

Both NaHy fresh hydrogel and the matured gel, after 24 h at constant temperature of 25°C, showed a linear decrease in viscosity as the stress (shear rate) increased. Again, this result is positive in terms of PAM 3D printing, since it guarantees that the hydrogel will respond to stress solicitation during extrusion (101,122). Nevertheless, the viscosity values of NaHy fresh hydrogel were significantly smaller and variable with respect to NaHy hydrogel after 24 h, which presented higher and more stable viscosity values in the whole range. It is also worth to notice the steeper slope of NaHy hydrogel after 24 h, indicating a faster, consistent response to extrusion, ultimately leading to better printing properties. This is probably due to the filling properties of both β glu and NaHy and their interaction and binding abilities which lead to the formation of internal networks with a suitable yield strength range (123). These considerations justify the choice of using the same 3D printing process parameters for both hydrogels (107).

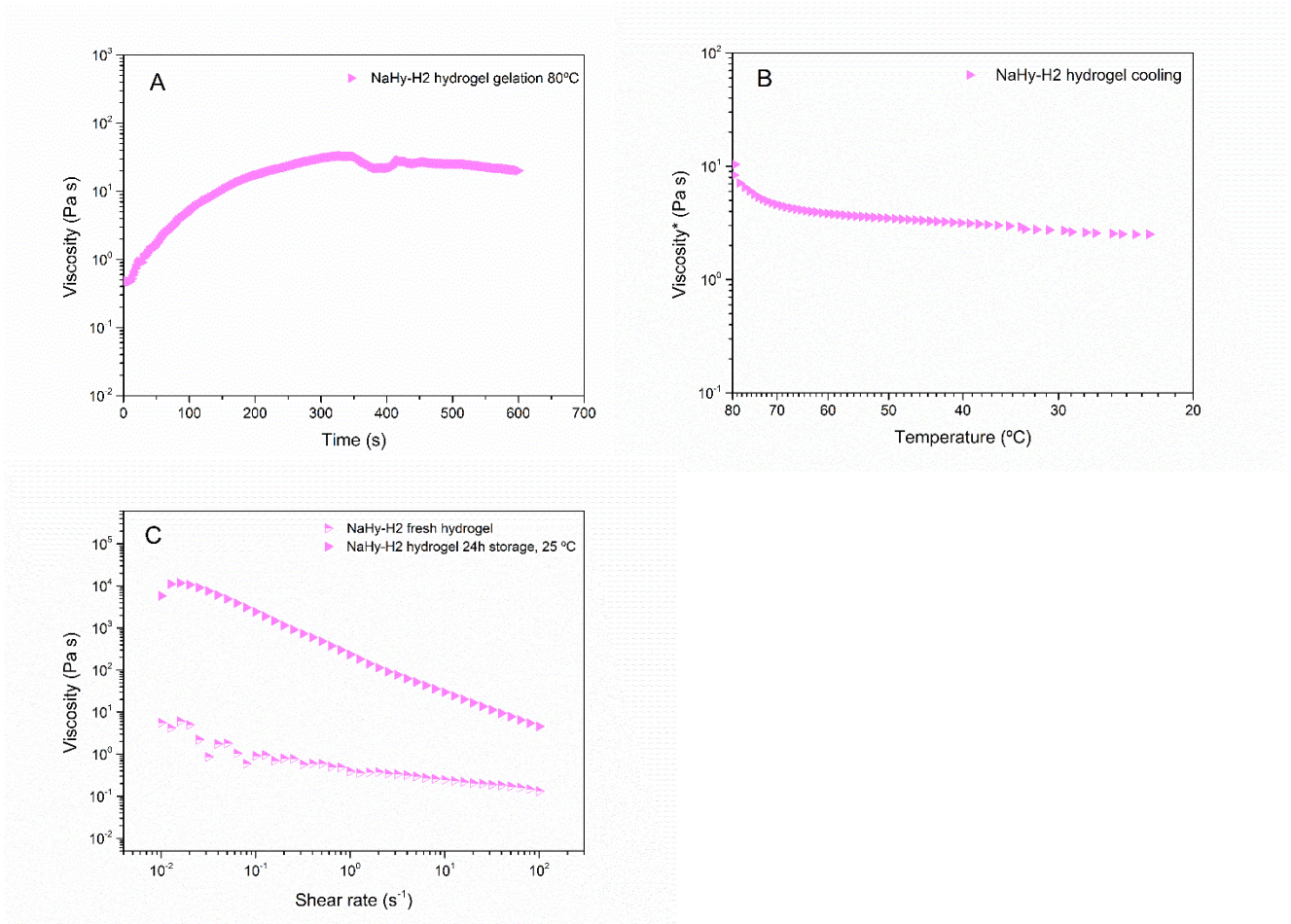


Figure 3.13. Rheograms of NaHy-H2 hydrogel. (A) Viscosity (Pa·s) vs. time (s⁻¹) showing hydrogel formation at 80 °C; (B) viscosity (Pa·s) vs. temperature (°C); (C) viscosity (Pa·s) vs. shear rate (s⁻¹) of hydrogel just after preparation and after storage at 25 °C for 24 h; (n=3).

3.4.2. Patches preparation

3.4.2.1. Selection of printing parameters and digital design

Nozzle diameter

The nozzle diameter has a considerable influence on the printing resolution, the adhesion between printing layers and even on the hydrogel extrusion (56). The three-nozzle tested corresponded with standardized 20, 16 and 14 gauge (**Figure 3.14**). The 20-gauge (0.80 mm) nozzle produced a line of uniform thickness, resulting in an optimal extrusion. The 16-gauge also led to a continuous deposition, but the layer thickness was larger than the nozzle size, resulting in an excessive amount of extruded material. The 14-gauge nozzle (1.62 mm internal diameter) caused the deformation of the printed layer and

3. Pressure Assisted Microsyringe 3D printing

was thus considered inadequate. Thus, a diameter nozzle of 0.80 mm (20 gauge) was selected to print the selected hydrogels (G4- β glu and NaHy-H2).

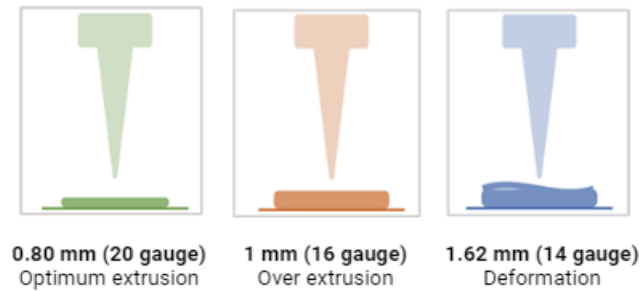


Figure 3.14. Schematic representation of behavior during extrusion using tips with different internal diameters.

Infill density







All tests were performed with the filling fixed at 100 %. This could increase the strength and stiffness of the printed object and thus improve the mechanical characteristics of the planned structure.

Flow rate

This parameter is preset in the slicing software and expressed in percentage as it is normalized with respect to the full extrusion rate of the printer. The corresponding VFR is calculated by *Eq 3.1*. The behavior of the hydrogels during extrusion and the amount of deposited material were evaluated between 30% and 80% with a constant printing speed of 15 mm/s. This range was chosen according to preliminary tests: flow rate below 30% were unable to extrude the hydrogels, preventing the printing from happening; for flow values over 80% the extrusion was too fast, leading to lack of printing accuracy. The printing results working between 30-80% flow (see **Table 3.6**) showed that low flow values provided better resolution, higher uniformity in material deposition, and lower deformation. The selected hydrogels showed the same behavior. After evaluating the quality of the printed patches in terms of resolution, presence of imperfections, and material deposition, a flow rate value of 40% was selected (Patch F_40).

3. Pressure Assisted Microsyringe 3D printing

Table 3.6. Printed patches from G4- β glu hydrogel at different percentages flow.

Patch code	Flow (%)	Image	Evaluations
Patch F_30	30		Incomplete extrusion
Patch F_40	40		Complete extrusion, optimum layer thickness
Patch F_50	50		Rapid extrusion and non-continuous patch
Patch F_60	60		Over extrusion
Patch F_70	70		Very rapid extrusion, shape deformation
Patch F_80	80		Very rapid extrusion with shape deformation and a high layer thickness

Print speed

Once the nozzle, the infill and the flow were selected, the next parameter to optimize was the print speed. To do so, the starting point was Patch F_40. In particular, a print speed range of 10–30 mm/s was evaluated (**Table 3.7**). High print speeds (20–30 mm/s) induced poor quality and low printing accuracy; at lower values (10–15 mm/s), a more homogeneous extrusion of the material and higher resolution of the printed patch structure could be observed. However, 10 mm/s led to uneven material deposition due to the noticeably slower movement of the extruder, resulting in variable thickness of the extruded gel. By applying a print speed of 15 mm/s it was possible to obtain a continuous extrusion and a uniform patch (Patch F_40_S_15), this being the selected printing speed. Both hydrogels showed the same behavior.

Material Extrusion Rate (MER)






The MER is a parameter that determines the amount of material extruded per unit of time and determines the printability. The MER was evaluated at different printing speeds, with a fixed flow rate of 40%. The patches evaluated of both hydrogels were F_40_S_10, F_40_S_15, F_40_S_20, F_40_S_25, and F_40_S_30.

A linear decrease ($r = -0.99$) of the amount of extruded material in one minute can be observed with respect to the increase in the printing speed for both hydrogels. The values of the correlation coefficient (R^2) were 0.98 and 0.99 for G4- β glu and NaHy-H2, respectively, as shown in **Figure 3.15**.

In consideration of the data obtained, it is possible to conclude that hydrogels (G4- β glu and NaHy-H2) show the same behavior with respect to the set printing parameters; for this reason, the same 3D printing conditions were selected for both of them.

3. Pressure Assisted Microsyringe 3D printing

Table 3.7. Printed patches from G4- β glu hydrogel at different values of printing speed.

Patch code	Speed (mm/s)	Image	Evaluations
Patch F_40_S_10	10		Slow printing
Patch F_40_S_15	15		Optimum printing Smooth and continuous extrusion
Patch F_40_S_20	20		Rapid printing with low material extrusion
Patch F_40_S_25	25		Very rapid printing
Patch F_40_S_30	30		Very rapid printing, poor adhesion to the support

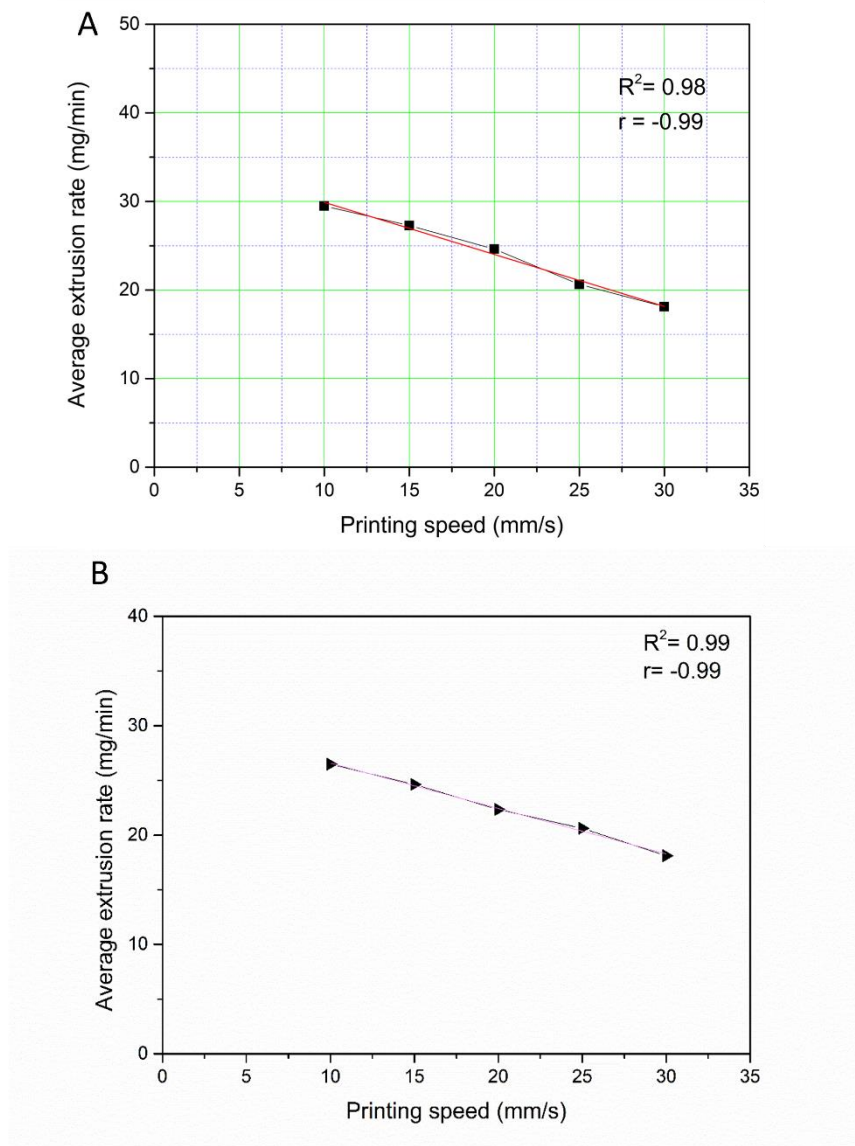


Figure 3.15. Effect of print speed on the extrusion rate of the G4- β glu (A) and NaHy-H2 (B) hydrogels.

Optimization of 3D printing design

During the extrusion process the material is pressurized and pushed out through the nozzle tip. The resulting extruded semisolid is then placed over a printing platform, following the pre-determined pattern created using CAD software, following a path and a particular shape. In the pattern design phase, the evaluate of the raster angle is very important because it represents the orientation of the filament filling the patch. The raster angle is the angle between the route of the nozzle and the X-axis and it is decisive for the

final mechanical properties of the 3D printed device. **Figure 3.16** shows the different raster angles that could be used.

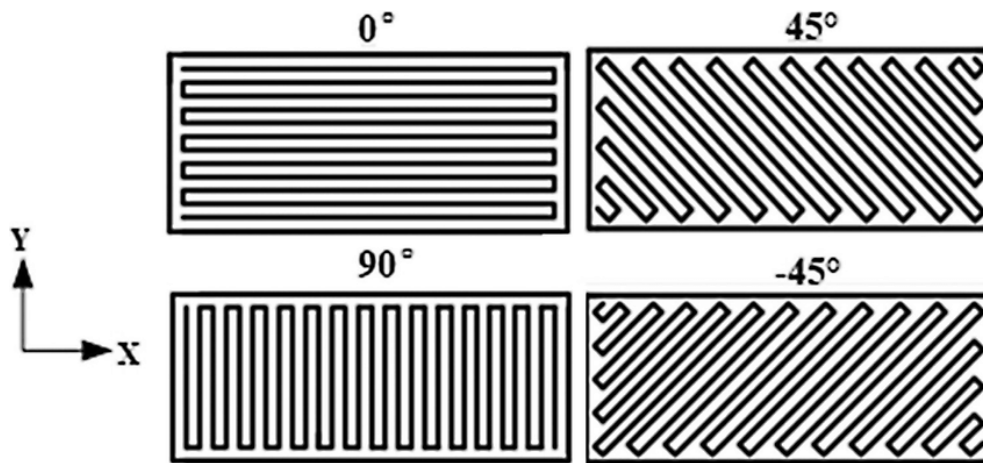


Figure 3.16. Raster angles of 0° , 90° , 45° and -45° .

The optimal raster angle for maximum structural strength is 0° , whereas a raster angle of 90° results in the lowest level of structural integrity. The 45° orientation offers intermediate mechanical qualities but enhanced strength when subjected to force along the Y-axis, compared to the 0° orientation. Moreover, when considering the movement of the syringe in the XY plane with respect to the plate, adopting a 45° orientation helps to mitigate syringe sudden changes of direction.

During the preliminary stage of this study, a 45° orientation of the inner filling was chosen in order to evaluate the resistance of the patch to stress in various directions. For patches with more than one-layer (multi-layered) the orientations $+45^\circ$ and -45° ($+45^\circ/-45^\circ$, **Figure 3.17**) were alternated between layers, since this should maximize the mechanical performance.



Figure 3.17. Orientation of $+45^\circ/-45^\circ$.

Optimization of post-printing process.

3. Pressure Assisted Microsyringe 3D printing

An important aspect to consider during PAM 3D printing is the selection of the printing support. The printing support (or printing surface) can be made of different materials and, ideally, it should establish minimum to no interactions with the printed product. In this study, three materials were selected: PTFE, PET, and silicone. The lower the interaction between the printed structure and the printing support, the easiest the detachment. Subsequently, the printed object requires a post-printing drying process to remove the solvent (water), leading to the final object. The drying process is also crucial to obtain full, resistant and elastic patches. For an optimal drying process, both temperature (°C) and time (h) must be carefully set; too high temperatures or too long times may lead to excessive solvent evaporation, resulting in patch deformation and/or shrinking. On the other end, too low temperatures and short drying times lead to sticky patches easily susceptible to microbiological contamination due to insufficient water removal.










The patches were printed on the selected supports (PTFE, PET, silicone). For each support, three samples were printed with the previously selected printing parameters and then subjected to different drying conditions (see **Table 3.8**). This study enabled to select the best support and the most adequate drying conditions. By looking at the results (**Table 3.8**) silicone support after 24 h of drying at 37 °C was the most convenient as it allowed an easy patch removal, not causing fractures or deformations.

Although these studies enabled the selection of the most suitable hydrogel composition, the optimal printing surface, and the best drying conditions, the final patches showed some limitations such as low mechanical resistance after detachment. Thus, the next steps aimed to solve this problem.

To do so, the first strategy was to print multilayer patches. The incorporation of additional layers should enhance the overall thickness, resulting in stronger patches with higher manageability. Bi-layered and three-layered patches were produced under the already established parameters and post-processing conditions: 0.80 mm nozzle diameter, 100% infill (+45°/-45°), 40% flow, 15 mm/s printing speed, silicone printing surface and 37 °C, 24 h of drying.

3. Pressure Assisted Microsyringe 3D printing

Table 3.8. Optimization of post-printing process (drying conditions and different supports).

Conditions (T/time)	Printing support (or surface)	G4- β glu hidrogel (monolayer, 45°)	Detachment easiness
70 °C/12 h (111)	PET		+
	PTFE		+
	silicone		+
40 °C/16 h	PET		+
	PTFE		+
	silicone		+
37 °C/24 h (124)	PET		++
	PTFE		++
	silicone		+++

The detachment from the printing support was not easy (+), easy (++), very easy (+++).

Table 3.9. Image of rectangular patches 10×2 cm, bi-, and three-layer with +/- 45° orientation.

Layer	Post drying
Bi-layer	
Three-layer	

By comparing the final bi-layered and three-layered patches (**Table 3.9**) with its monolayer counterpart (**Table 3.8**), the former ones resulted more fragile after solvent removal. Thicker patches (three-layers) had a continuous structure and fewer break points but were not adequately dried at the pre-set conditions. Furthermore, the greater thickness precluded their use in wound care, as these patches did not adapt to the conformation of the skin due to lack of flexibility. In fact, their rigidity makes them difficult to use and uncomfortable for patients, ultimately leading to therapeutic non-compliance. The bi-layer structure presented greater surface area discontinuity and was therefore discarded from the study.

Consequently, the monolayer structure could be the most promising because of its greater continuity and flexibility. In order to solve the mechanical resistance problem, an extra support was prepared. To do so, the hydrogels were extruded onto a polymeric support material that, after the post-printing drying process, will act as an additional layer of the final patch. That is, this polymeric backing material will not be detached from the printed hydrogel. With this purpose, the polymeric backing was prepared by casting method using Alg biopolymer with the following composition: Alg 1.5% w/w, Gly 10% w/w, and water (W) 88.5% w/w optimized in a previous work (113). Alg is a natural polysaccharide widely used in the health field for its excellent water solubility, biodegradability, biocompatibility, and no toxicity (125). Moreover, it was successfully employed for patch preparation by solvent casting (113).

The final formulations, Alg_βglu and Alg_NaHy patches are monolayer structures with the Alg support as backing (G4-βglu and NaHy-H2, respectively,) was printed (**Figure 3.18**).

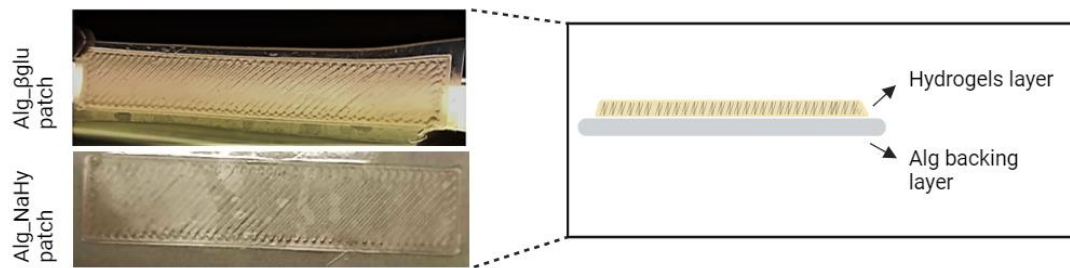


Figure 3.18. Image of patches after drying (left) and schematic representations of the patch composition.

Through macroscopic and morphological analysis, it is possible to observe that, after drying, Alg_βglu and Alg_NaHy patches were more regular and uniform than their monolayered counterparts printed on silicone without Alg. In addition, the patches printed over the Alg layer were more manageable and resistant than the one-layer printed on the silicone backing, since this backing is removed after drying.

3.4.3. Patches characterization

Scanning Electron Microscopy (SEM)

The morphology and thickness of each 3D printed patch were analyzed by SEM. The micrographs of G4-βglu patches are gathered in **Figure 3.19**. The monolayer patch possessed a homogeneous (**Figure 3.19A-B**) but unsmooth surface (**Figure 3.19C-D**), which could be apposite for skin adhesion. The thickness of G4-βglu resulted of $458.36 \pm 29.52 \mu\text{m}$ (**Figure 3.19E**) significantly different from the digital design (CAD: 0.2 cm of the .gcode file), showing low print fidelity.

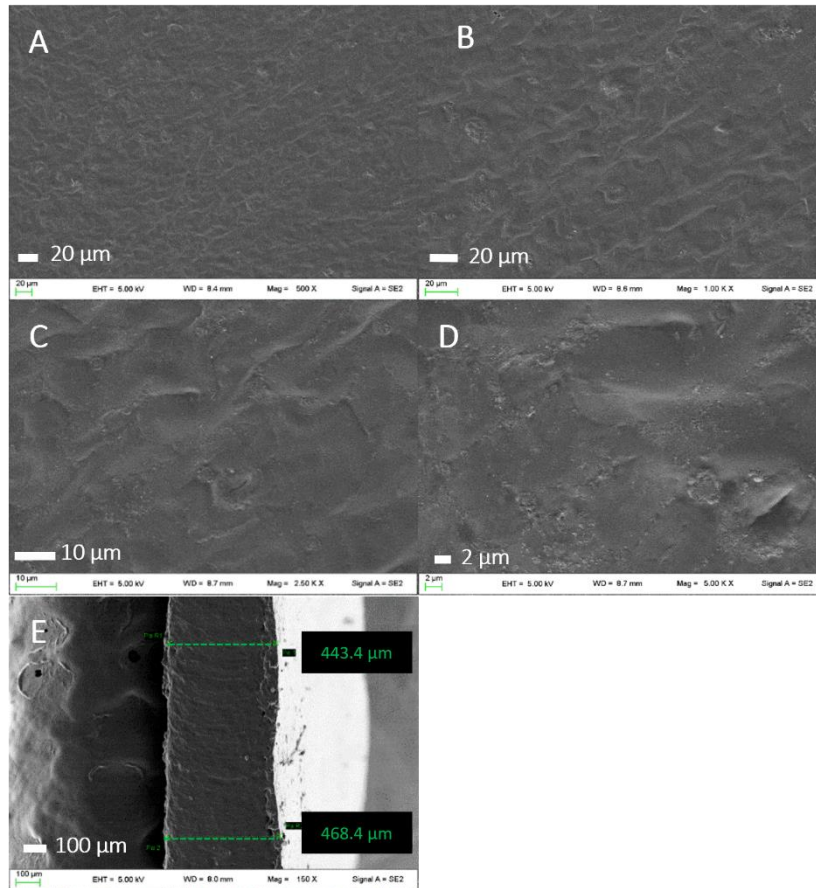


Figure 3.19. One-layer β glu patch surface morphology 500X (A), 1.00KX (B), 2.50KX (C) and 5.00KX (D), and thickness (E).

The surface of the bi-layer β glu patch was similar to the monolayer patch (homogeneous and rough, (Figure 3.20), while the three-layer β glu patch showed a wrinkled surface and a higher discontinuity (Figure 3.21). For both bi-layer and three-layer patches the thickness measured was higher than the thickness defined by the CAD files. In particular, the bi-layer β glu patch had a thickness of 1 mm vs 0.4 mm CAD dimensions; for the three-layer β glu patch it was 2.8 mm vs 0.6 mm of CAD, in both cases probably due to the amount of water accumulated by the hydrogel. Unfortunately, it was not possible to measure the thickness by SEM, due to the amount of water that the patch accumulated, so it was measured with a calliper.

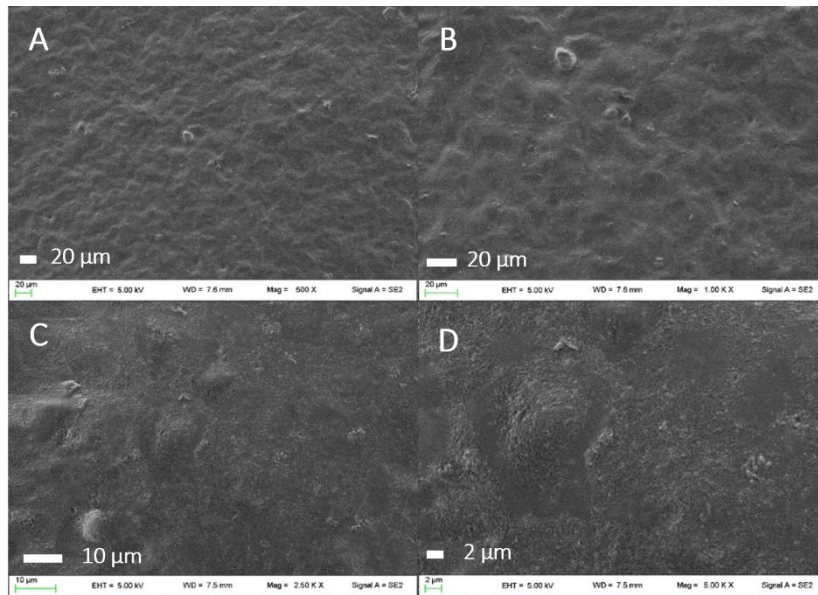


Figure 3.20. Bi-layer β glu patch surface morphology at 500X (A), 1.00KX (B), 2.50KX (C) and 5.00KX (D). Total thickness: 1 mm.

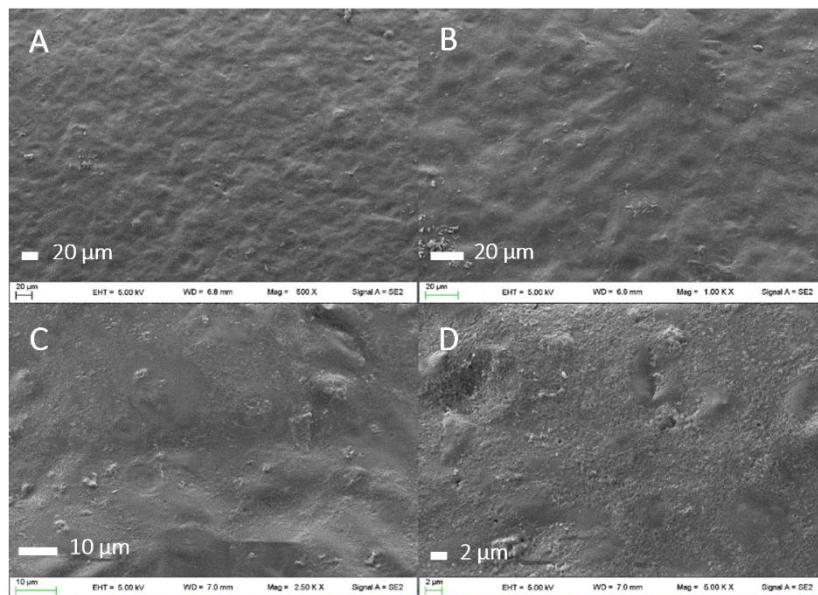


Figure 3.21. Three-layer β glu patch surface morphology at 500X (A), 1.00KX (B), 2.50KX (C) and 5.00KX (D). Total thickness: 2.8 mm.

Finally, the prepared Alg_ β glu patch was characterized. Analyzing both sides of each hydrogel, the G4- β glu sides were wrinkled (**Figure 3.22A-C**), contrary to the Alg backing layer of the Alg_ β glu patch (**Figure 3.22D-F**). The total reported thickness was $926 \pm 18 \mu\text{m}$ (**Figure 3.22G**), which was sufficiently thin to ensure skin imperceptibility

3. Pressure Assisted Microsyringe 3D printing

while providing sufficient mechanical strength to the final patch, being less susceptible to fractures during manipulation.

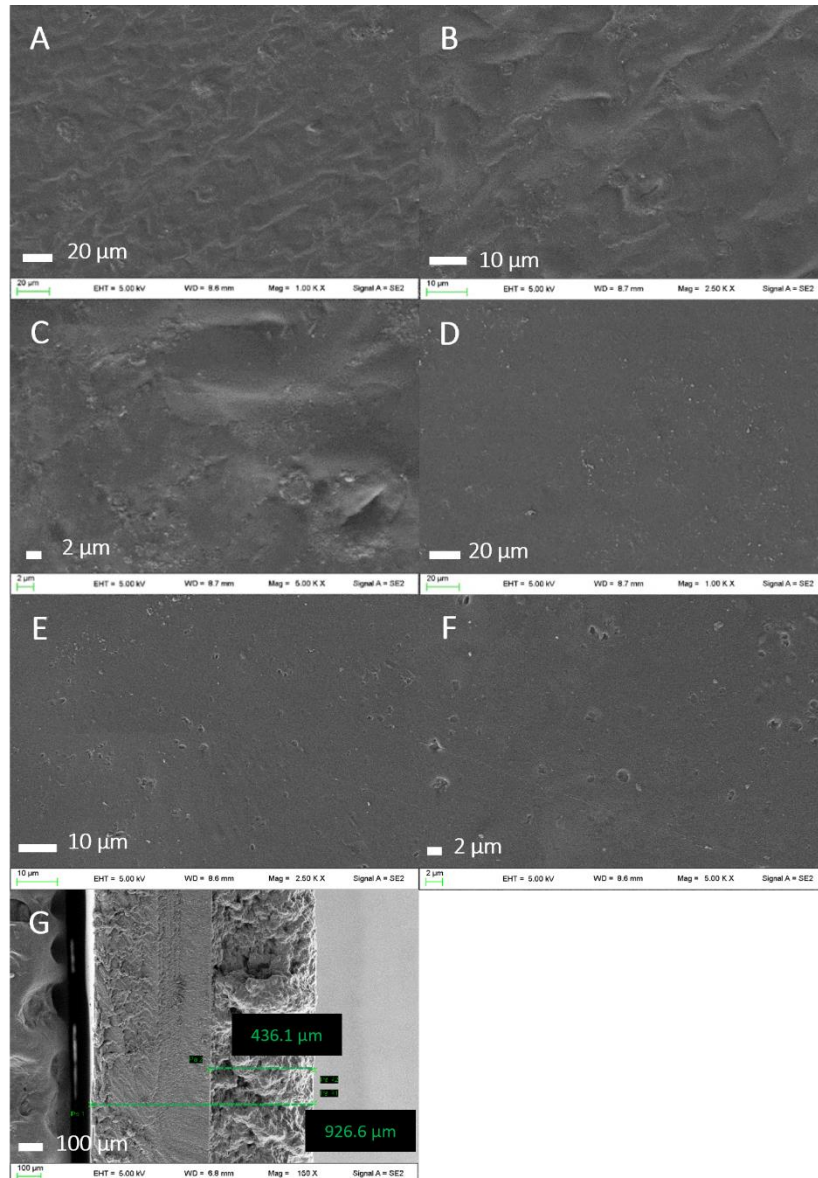


Figure 3.22. Micrographs of the Alg_βglu patch: G4-βglu side (A-C) Alg side (D-F). Magnifications 1.00K X (A, D), 2.50K X (B, E), 5.00K X (C, F) and thickness (G).

The surface of the NaHy-H2 monolayer patch appeared to be homogeneous on both sides but wrinkled (Figure 3.23A-C) (something convenient for skin adhesion), similar to its counterpart without NaHy. This indicates that the addition of this polymer did not produce significant changes in the patch physical appearance. Interestingly, it possessed $222.05 \pm 1.06 \mu\text{m}$ in thickness (Figure 3.23D), suggesting higher printing

3. Pressure Assisted Microsyringe 3D printing

fidelity with respect to the digital design (CAD; 0.222 cm in final patch vs 0.2 cm of the .gcode file), something that is worth to notice since it will offer higher fidelity and, ultimately, higher product quality and reproducibility.

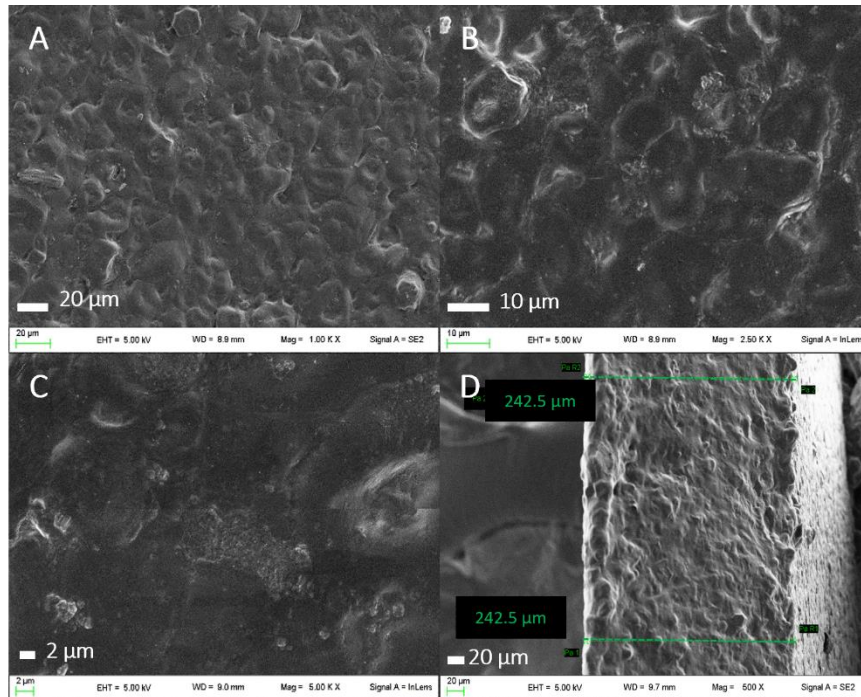


Figure 3.23. One-layer NaHy patch surface morphology 1.00KX (A), 2.50KX (B) and 5.00KX (C), and thickness (D).

Regarding this, corresponding bi-layer counterpart (Figure 3.24) showed a homogeneous distribution of the product (Figure 3.24A-D); it could be to the larger amount of extruded product. The thickness measurement could not be carried out due to the large accumulation of water in the patch that did not allow the vacuum for its thickness characterization by SEM. For the same reason, the three-layer patch they have not been characterized.

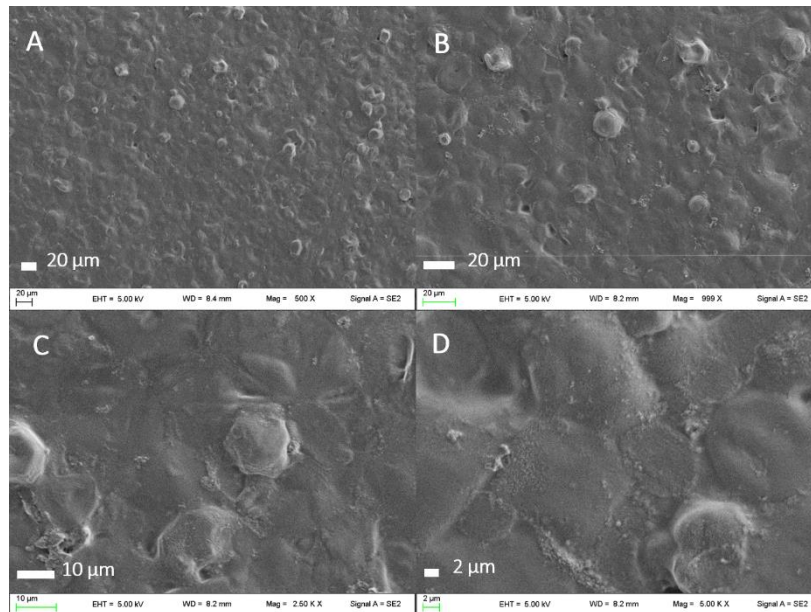


Figure 3.24. Bi-layer NaHy patch surface morphology 500X (A), 1.00KX (B), 2.50KX (C) and 5.00KX (D).

Finally, the Alg_NaHy patch is reported in **Figure 3.25**. This analysis was made by scanning patch surfaces on both sides (NaHy-H2 layer and Alg backing layer). The NaHy-H2 layer was analyzed at 500X and 1.00KX magnifications at maximum because the high amount of water content led to a reduction in the image resolution (due to water evaporation) when working at higher magnifications. The morphological analysis of the NaHy side showed the same surface already reported (**Figures 3.25C-D**), whereas the Alg backing layer (**Figure 3.25A-B**) possessed an evident homogeneity and smoothness. This property is ascribable (in both Alg_βglu and Alg_NaHy) to the solvent casting method used for Alg, allowing a more cohesive layer to be formed without irregularities.

It is also worth to notice the intimate contact established between the NaHy and Alg layers (**Figure 3.25E**), suggesting remarkable cohesion of the 3D printed layer on the Alg backing. The total thickness of the Alg_NaHy patch was $470.07 \pm 12.79 \mu\text{m}$, of which $230.8 \pm 9.90 \mu\text{m}$ corresponded to NaHy layer and $239.27 \pm 13.36 \mu\text{m}$ belonged to the Alg backing layer. This patch showed higher print fidelity (CAD design: 0.2cm) than the Alg_βglu patch since for the NaHy layer it resulted 0.230 cm (Alg_NaHy patch) compared to the βglu layer with 0.436 cm (Alg_βglu patch).

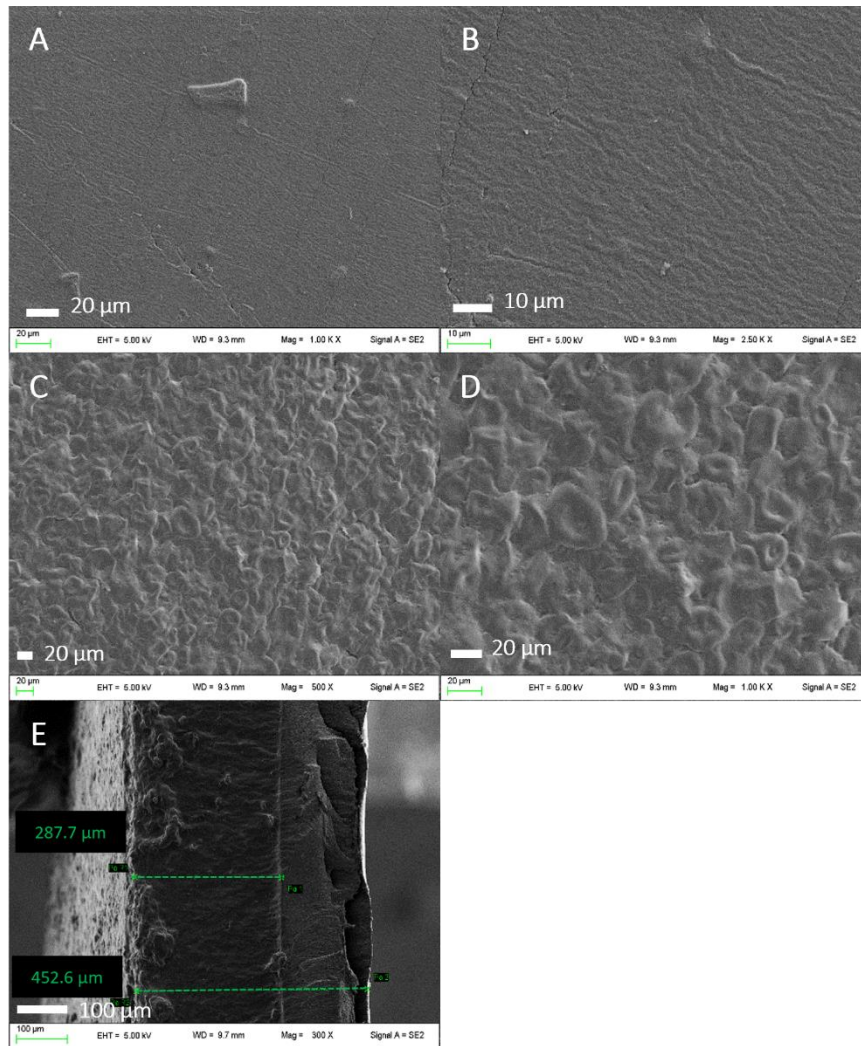


Figure 3.25. Alg_NaHy patch morphology on both sides. Alg backing layer surface morphology 1.00KX (A) and 2.50KX (B); and NaHy layer surface morphology 500X (C), 1.00KX (D) and thickness (E).

Due to the adequate thickness, morphology, manageability, and integrity of the final formulation, the Alg_βglu and Alg_NaHy patches selected for further characterization.

Thermogravimetric analysis (TGA)

TGA measurements for Alg_βglu and Alg_NaHy patches are reported in **Figure 3.26**. The residual mass and the derivative (DTG) curves of both patches are characterized by the presence of a multi-step degradation behaviour. The first phase of weight loss/decomposition has been attributed to the loss of water and moisture content of Alg_βglu and Alg_NaHy (113) adsorbed by the hydrophilic polymer, which were released in the range of about 50 –110°C, with a maximum decomposition rate at 90°C. In both

formulations, the residual water content was estimated to be below 10% at 110°C. Assumed that the dried corn starch and Alg did not undergo weight losses during heating (126,127), the measured weight loss below 110°C can be exclusively ascribed to water content. Moreover, the weight loss in this phase relies on the moisture content of the starch and Alg as a higher moisture content results in higher weight loss (127). At higher temperatures, the patches show one main degradation step at 227° and 233°C for of Alg_βglu and Alg_NaHy, respectively. The second one centred at 270°C and 280°C Alg_βglu and Alg_NaHy, respectively. Both peaks can be attributed to the superimposed degradation of the main fractions in the film composition e.g. glycerol, Alg, starch and β-glucan filler, consisting in glycerol removal and polysaccharides decomposition. The thermal degradation of NaHy can be found in the same temperature range assigned to the second peak (128), that is superimposed to the thermal profile of the main components, so no differences can be found in terms of peak temperatures. On the other hand, the addition of NaHy reduced the mass loss rate and increased the char amount at the end of the test: as reported in (129), NaHy-Alg based systems are thermally more stable than individual polymers, due to the presence of hydrogen bonding between the different polymers.

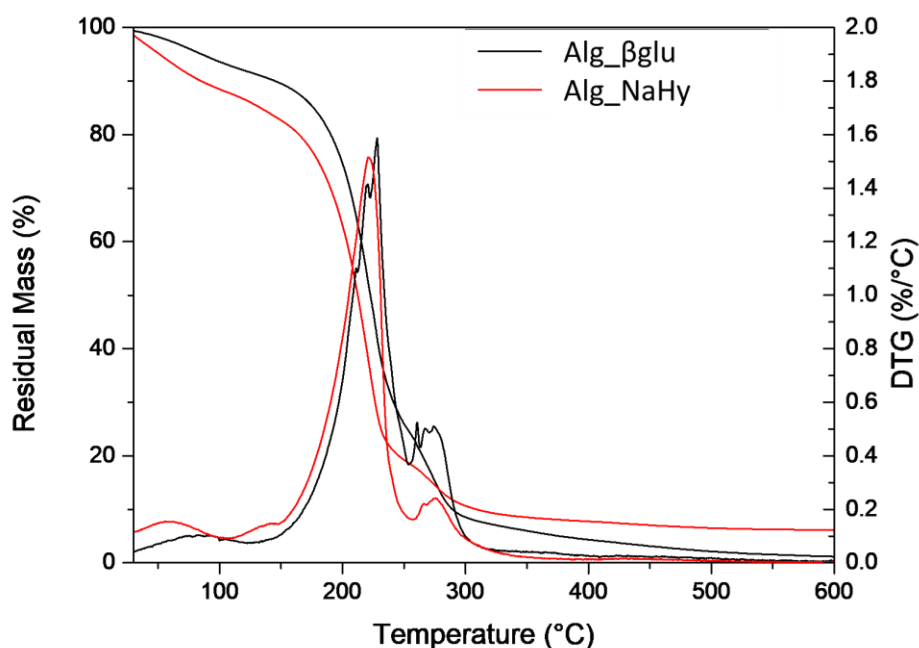


Figure 3.26. Residual mass and derivative mass loss (DTG) curves of Alg_βglu and Alg_NaHy.

Mechanical characterization

Adequate mechanical properties that can tolerate stretching during daily activities are essential for wound contact patch applications (130), thus, it is necessary to know the elastic response of the produced patches. The mechanical characteristics of both systems (Alg_βglu and Alg_NaHy) were evaluated after their storage at R.T. in two different humidity conditions: 1 week under vacuum condition and 1 week under saturated calcium chloride (CaCl₂) solution (relative humidity RH 75%) (107,131). The determination of mechanical response of different systems after storage is essential to evaluate the stiffness of polymeric systems before prior their application in contact with the wound, being that mechanical characteristics of hydrophilic polymeric matrices are strongly influenced by humidity conditions (107,126). In literature it is evidenced that the strain condition for normal skin treatment is 61 to 70% (132). The results of mechanical characterization of the produced patches are reported in terms of elastic modulus (E), stress and deformation at break (σ_b and ϵ_b) (**Table 3.10**). **Figure 3.27** shows the stress–strain curves of Alg_G4_βglu with and without HA stored in the two different RH conditions. No particular variations were observed comparing both polymeric systems. A slight difference/improvement was registered for elastic modulus for Alg_NaHy respect to Alg_βglu, this phenomenon can be related to the presence of NaHy in the layer. NaHy powder act as a filler increasing the stiffness (**Table 3.10**). Limited research has been conducted on the impact of added NaHy on unplasticized starch properties and microstructure: in the case of neat starch, it has been found that, due to its hydrophilicity, NaHy can attach to starch granules via hydrogen bonding and electrostatic effect, leading to the blockage of a continuous starch matrix and a more compact three-dimensional network structure. Analogously, in the presence of glycerol, the different interaction among NaHy, starch, glycerol and water prevented amylose leaching, as the hydroxyl and carboxyl groups of NaHy formed hydrogen bonds with amylose, effectively interfering with starch retrogradation and water interaction (102) providing stability and strength to the patch both in vacuum and controlled humidity.

Table 3.10. Mechanical parameters measured for Alg_βglu and Alg_NaHy stored at R.T. for 1 week under vacuum conditions and in oversaturated CaCl₂ solution.

<i>Formulations</i>	<i>Conditions</i>	σ_b (MPa)	ε_b (%)	E (MPa)
Alg_βglu	Under vacuum	0.92 ± 0.08	50 ± 1	3.80 ± 0.82
	CaCl ₂	0.62 ± 0.07	48 ± 8	3.37 ± 0.31
Alg_NaHy	Under vacuum	0.85 ± 0.16	50 ± 1	4.17 ± 0.59
	CaCl ₂	0.67 ± 0.09	40 ± 2	4.52 ± 0.40

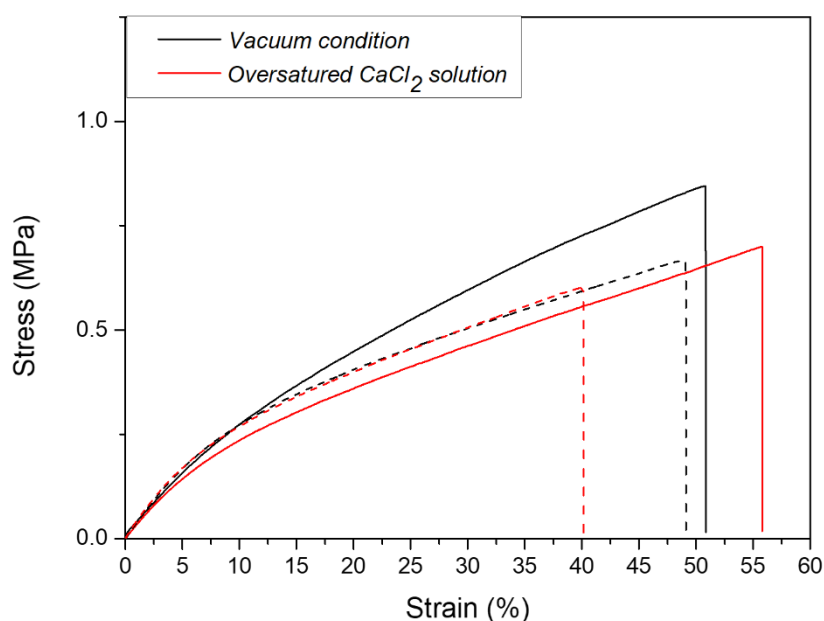


Figure 3.27. Tensile stress–strain curves for Alg_βglu (straight-line) and Alg_NaHy (dash) stored at R.T. for 1 week under vacuum (black line) condition and in oversaturated CaCl₂ solution (red line).

FT-IR

The chemical interactions between the different materials were explored through FT-IR spectra (**Figure 3.28A-B**).

The FT-IR spectrum of pure Gly shows five absorption bands located between 800 and 1150 cm⁻¹, corresponding to the vibrations of the C-C and C-O bonds (**Figure 3.28A**). Three broad bands at 850, 925 and 995 cm⁻¹ corresponding to the C-C backbone vibration; the band at 1045 cm⁻¹ is associated with the C-O bond stretching at C1 and C3, while the band at 1117 cm⁻¹ corresponds to the C-O stretching at C2 (133).

The FT-IR spectrum (**Figure 3.28A**) of pure NaHy showed two absorption bands at 1020 and 1073 cm^{-1} assigned to the stretching of C-O bonds in the hydroxyl groups (134). Also, pure NaHy showed bands at 1410 and 1620 cm^{-1} due to the C-O asymmetrical and symmetrical C-O stretching in COO^- .

In **Figure 3.28B**, the five absorption bands of Gly (above mentioned) were detectable in both patches (Alg_βglu and Alg_NaHy) (133). The effect of the interactions between Gly and water can be analyzed by comparing the spectra of the CS powder with those of the Alg_βglu and Alg_NaHy patches (**Figure 3.28B**). When compared with the IR spectra of the raw materials (**Figure 3.28A**), the characteristic bands of saccharides were shifted. The peaks at 1014 and 1022 cm^{-1} of CS and Alg, respectively, that could be assigned to C-O stretching, shifted to 1022 and 1030 cm^{-1} (133). The two characteristics absorption bands of Alg located at 1590 and 1408 cm^{-1} (belonging to the asymmetric and symmetric stretching vibration of the $-\text{COO}$ group) shifted to 1612 and 1416 cm^{-1} in Alg_βglu and Alg_NaHy patches (125) (**Figure 3.28B**). In addition, the bands at 3006 and 2910 cm^{-1} were related to the formation of inter- and intramolecular hydrogen bonding between saccharides (CS and Alg) and Gly (135). Based on these shifts we can observe how the addition of Gly promotes hydrogen bonding interactions between CS and Gly and Alg and Gly (136) (**Figure 3.28B**).

Finally, as shown in **Figure 3.28B**, the shift from 1620 to 1606 cm^{-1} could indicate the presence of NaHy in the Alg_NaHy patch (134). Finally, there should be an absorption band at 3300 – 3500 cm^{-1} that corresponds to the stretching of the N-H bonds in the amino groups of NaHy (137). The intensity of these absorption bands is due to the structure and composition of the NaHy used. The higher the molecular weight, the higher the intensity of the absorption bands. However, using HMW NaHy (800 kDa), no intense absorption bands were observed. This could be due to the low amounts of pure NaHy used in the patch. Therefore, it is possible to state that no great changes occurred in the Alg_NaHy patch spectrum in comparison to Alg_βglu patch (107) due to the low amounts of NaHy used, which are not detectable in the IR.

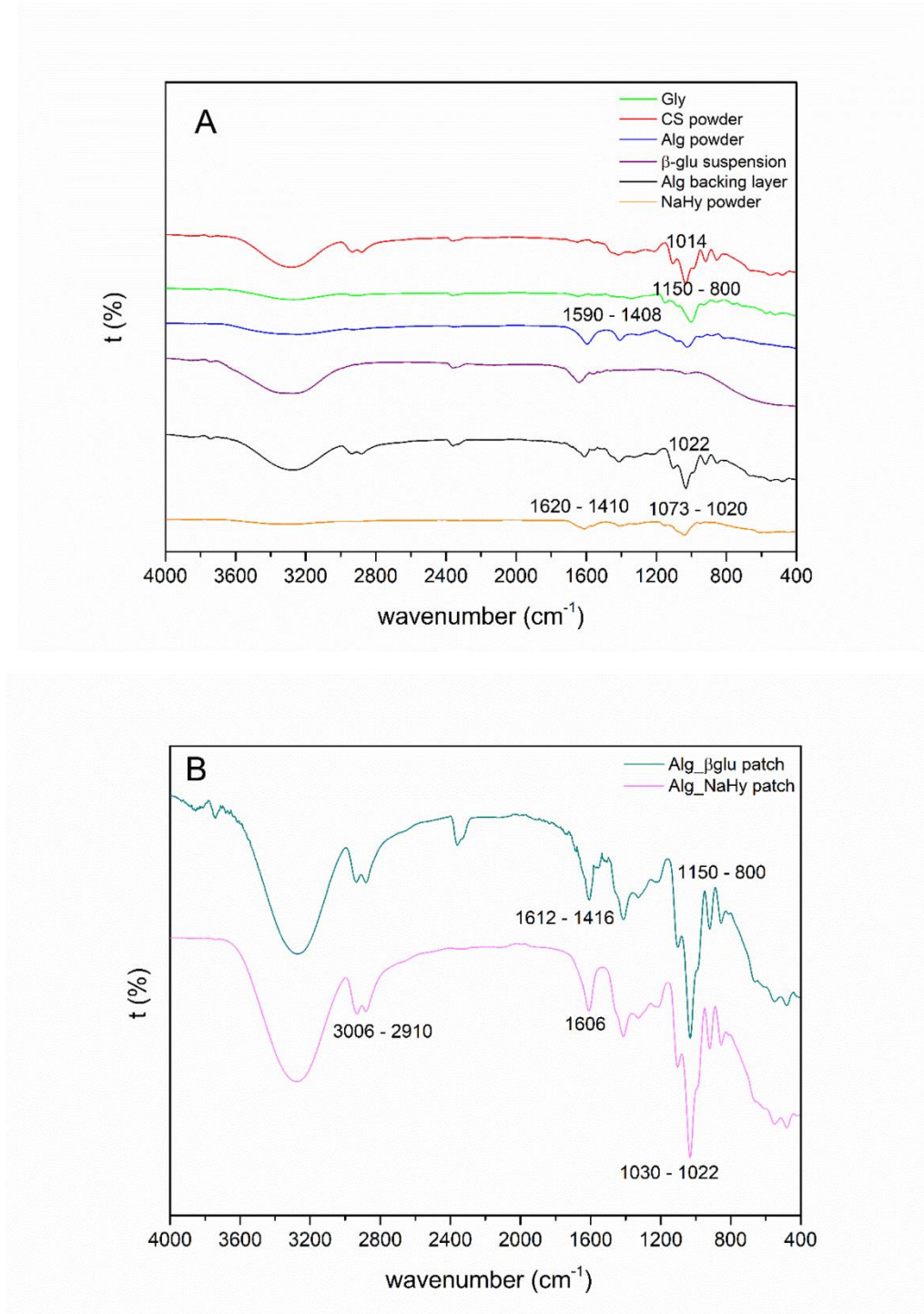


Figure 3.28. FT-IR spectra registered for raw materials (A) and both patches (Alg_βglu and Alg_NaHy) (B).

Swelling capacity

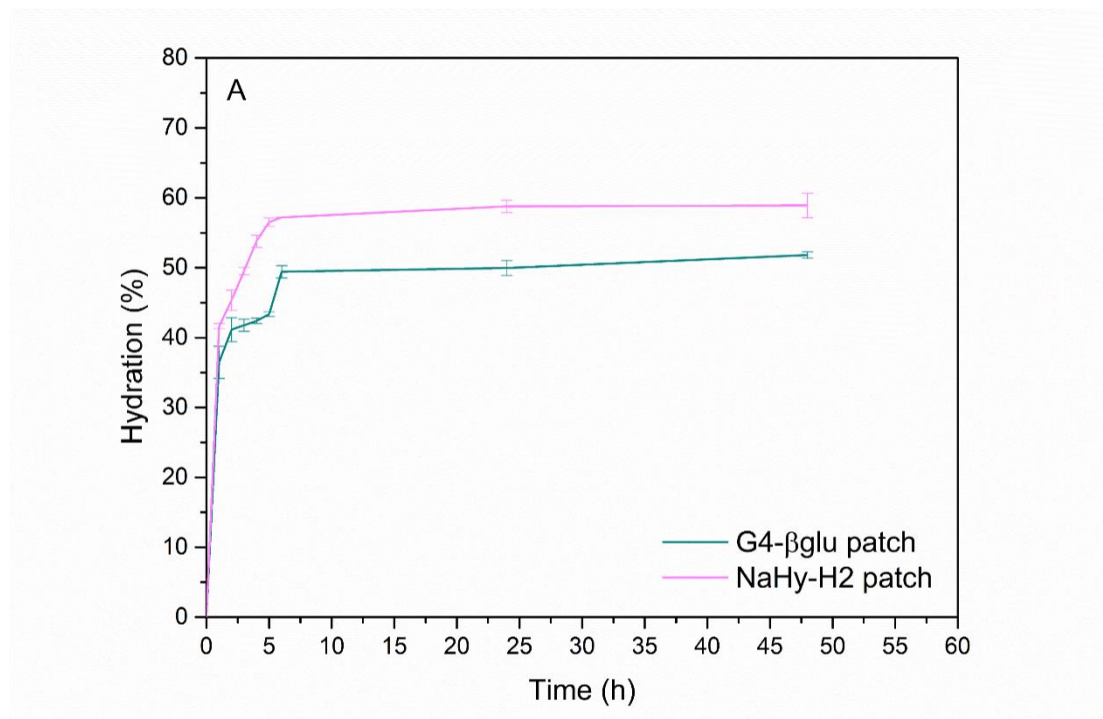
The swelling test is useful to determine the patch's ability to absorb wound exudate when applied *in vivo*. This can be assessed by the measurement of hydration % (Figure 3.29A). Another important property is the ease of removal from skin, especially

3. Pressure Assisted Microsyringe 3D printing

when applied on a wound, to avoid pain and ulterior tissue damage. To assess this aspect, the DS % of each patch was evaluated (**Figure 3.29B**). Both analyses were performed by soaking patches in SWF for predetermined time intervals and then weighed (as reported in *Section 3.3.4*). These experiments were performed on G4_βglu and NaHy-H2 patches (without Alg layer).

The swelling tests results (**Figure 3.29A**) showed that the percentage of SWF absorbed increases gradually within 10 h, reaching ~ 50% for the βglu patch (in 6 h) and 58 % for the NaHy patch (in 6 h). The G4-βglu patch reached the maximum absorption after 48 h, the final value being $51.08\% \pm 0.45$. Regarding the NaHy-H2 patch, the hydration % measured is higher than the βglu patch, being $58.91\% \pm 1.73$ after 48 h, suggesting that the presence of NaHy is able to increase the hydrophilicity of the patch and, subsequently, its ability to potentially absorb exudates.

The DS% results indicated that the Alg_βglu patch had slower degradation ($69.97\% \pm 1.03$ after 48 h) than NaHy patch, reporting an $80\% \pm 1.2$ after 48 h.



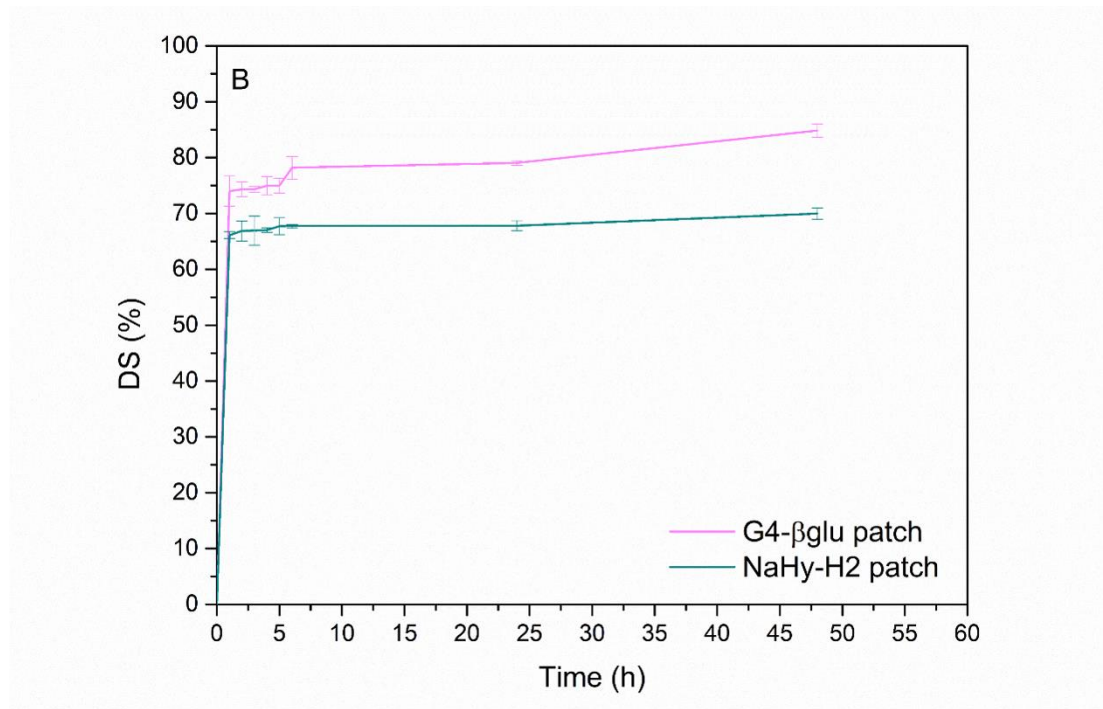


Figure 3.29. Hydration % (A) and DS % (B) diagrams of G4-βglu vs. NaHy-H2 patches.

Contact angle

The wettability is another important property to be evaluated when developing skin formulations, especially if it is intended to absorb wound exudates. The wettability was quantified by means of the contact angle, which was determined for both Alg_βglu and Alg_NaHy patches (**Figure 3.30**).

In both cases, a low contact angle was obtained. The average values are $14.56^\circ \pm 0.18$ and $12.17^\circ \pm 0.14$, for Alg_βglu and Alg_NaHy patches measured over the G4-βglu and NaHy-H2 sides, respectively. Alg_NaHy (**Figure 3.30**) showed a smaller contact angle than Alg_βglu, indicating a greater hydrophilicity due to NaHy and, more particularly, to the high amount of carboxyl and hydroxyl groups. Moreover, the different surface wettability could also be attributed to different porosities and roughness of the material.

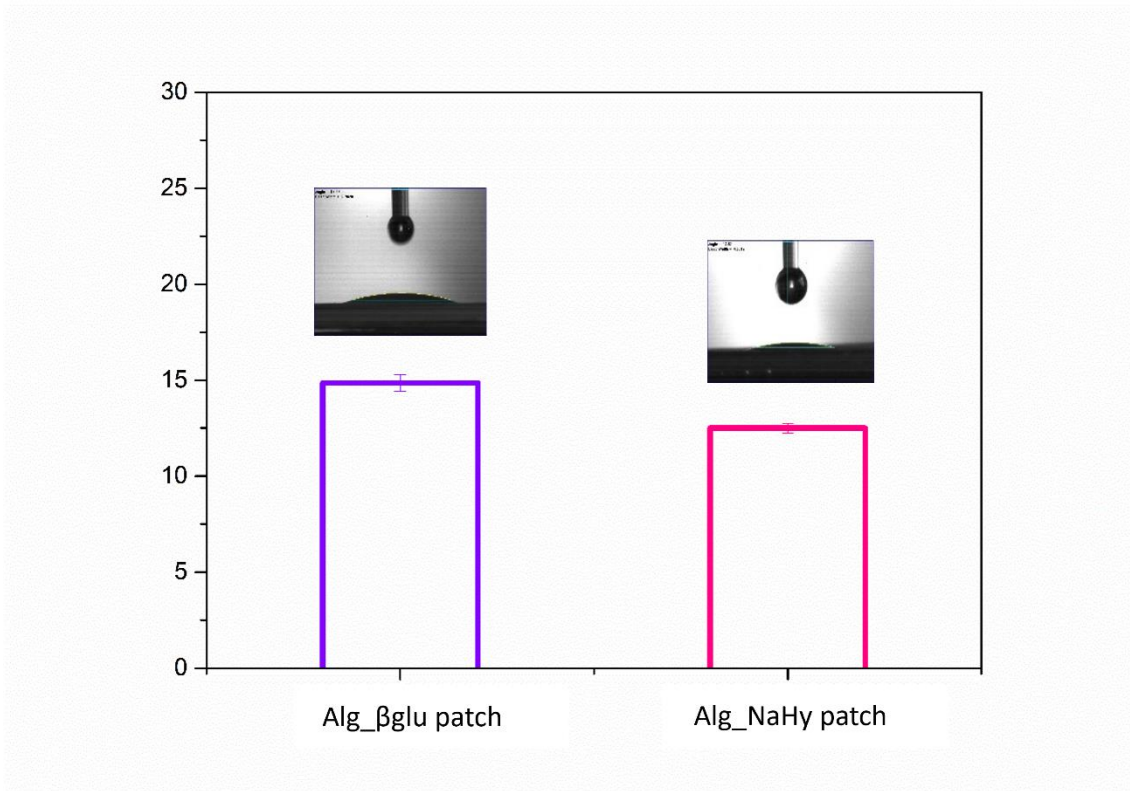


Figure 3.30. Contact angle of Alg_βglu and Alg_NaHy patches measured over the G4-βglu and NaHy-H2 sides, respectively.

3.4.4. Biological properties

Antimicrobial activity assay

The antimicrobial activity of βglu and βglu combined to NaHy, released by Alg_βglu and Alg_NaHy patches respectively, was evaluated by measuring the inhibition zone for the strains reported in **Table 3.5** representing the most common strains infecting skin wounds.

For Alg_βglu patch, the absence of antimicrobial activity was expected given the absence of antimicrobial activity of βglu. Remember that the main βglu activities are immunomodulating and bacteriostatic. Regarding Alg_NaHy, the antimicrobial property is not detectable because of the NaHy low concentration, which was determined in agreement with the optimal mechanical and 3D printability.

Cell viability- MTT assay

To assess the safety of the patches once applied on skin, an in vitro cytotoxicity assay was carried out by MTT test using the human immortalized keratinocyte cell line HaCaT. In particular it was considered the effect of the soluble fraction of βglu released

from the patches after incubation in the cell culture medium. The cells were kept in contact with different dilutions of the above mentioned sample for 24 h, since it was considered as indicative life time of the *in situ* patch application according to ISO 10993-5-2009.

The obtained results are shown in **Figure 3.31** show that just the highest concentration of β glu 14.4 μ g/ml is not safe for the cells as the measured viability is below 70%. In all the other cases cells viability resulted satisfactory.

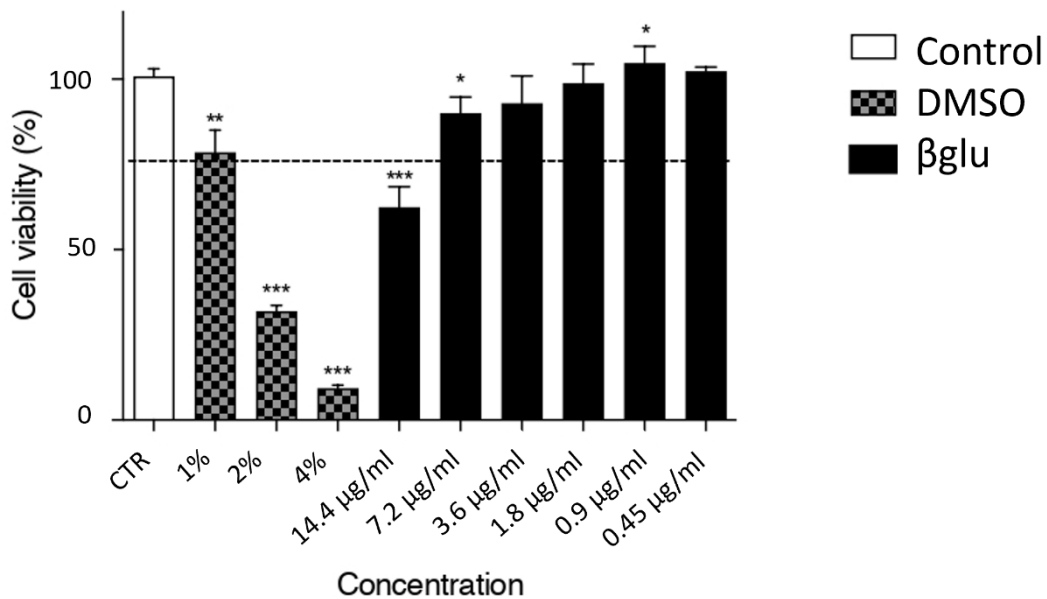


Figure 3.31. HaCaT cell viability measured *in vitro* for both patches. DMEM is used as negative control (CTR with 100% of cell viability) and DMSO, known to induce cell death, is used as a positive control with 3 different concentrations.

Scratch assay (In-vitro wound healing)

The safe β glu concentrations were then submitted to *in vitro* assays in order to evaluate their ability to stimulate keratinocytes growth and thus useful for wound healing enhancement. The most interesting results were obtained for the concentration 7.2 μ g/ml and 3.6 μ g/ml.

Interesting results were observed after 12 h of treatment as a significant wound area reduction can be detected for both 7.2 μ g /ml and 3.6 μ g /ml β glu concentration in comparison to CTR (untreated cells). After 24 h, the concentration 3.6 μ g /ml allowed to promote a complete wound field closure in comparison to CTR (**Figure 3.32**).

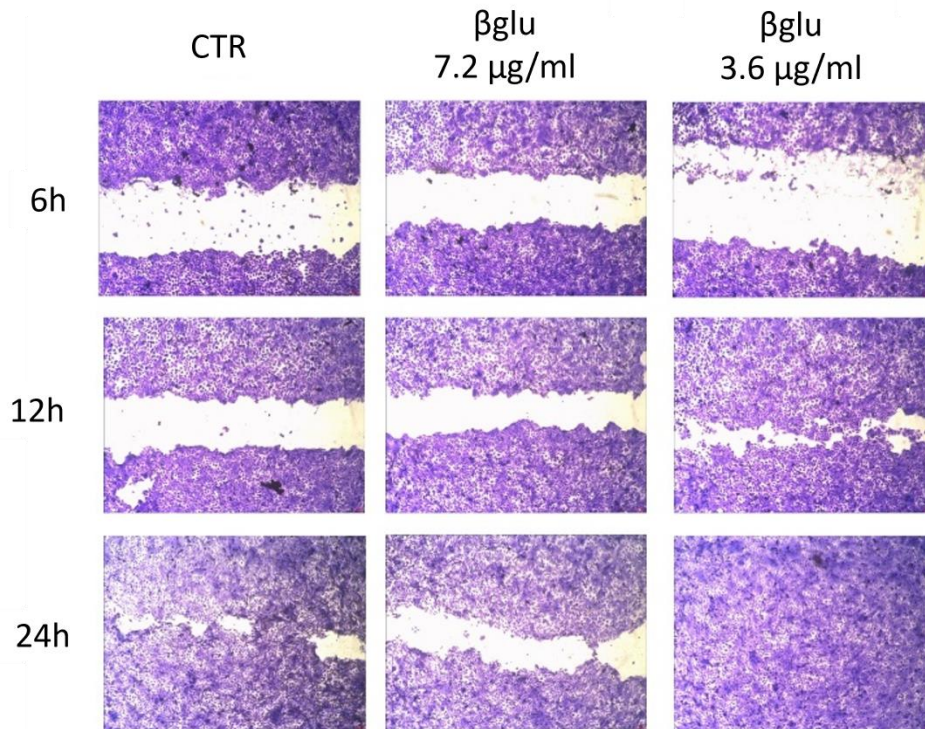


Figure 3.32. Pictures of the wound field at 6, 12, 24 h of treatment with the different concentrations of β glu compared with control (CTR).

Ex-vivo adhesion studies

The *ex-vivo* adhesion experiments were performed on healthy skin tissues as described in *Section 3.3.5*. The results obtained for both Alg_βglu and Alg_NaHy patches are gathered in **Figure 3.33**, the results expressed as adhesion strength (N).

The adhesion strength measured was 0.77 ± 0.23 N and 1.23 ± 0.21 N for Alg_βglu and Alg_NaHy patches respectively. Considering the results and the patch compositions, it is possible to observe that the greatest adhesion strength was shown by the patch containing NaHy. So, it can be hypothesized that this result is due to the establishment of a greater number of adhesion forces due to the NaHy addition to the βglu formulation. As the number of hydrogen bonds between formulation and skin increases, there is a higher adhesive strength of the formulation to the skin. More specifically, the main components of both patches (starch, βglu and NaHy when used) are very rich in free hydrophilic carboxyl (-COOH) and hydroxyl (-OH) groups, thus allowing the establishment of a wide number of hydrogen bonds, and other weak chemical bonds, with the biological substrate. That is the reason why the Alg_NaHy patch reported greater bioadhesion force than Alg_βglu.

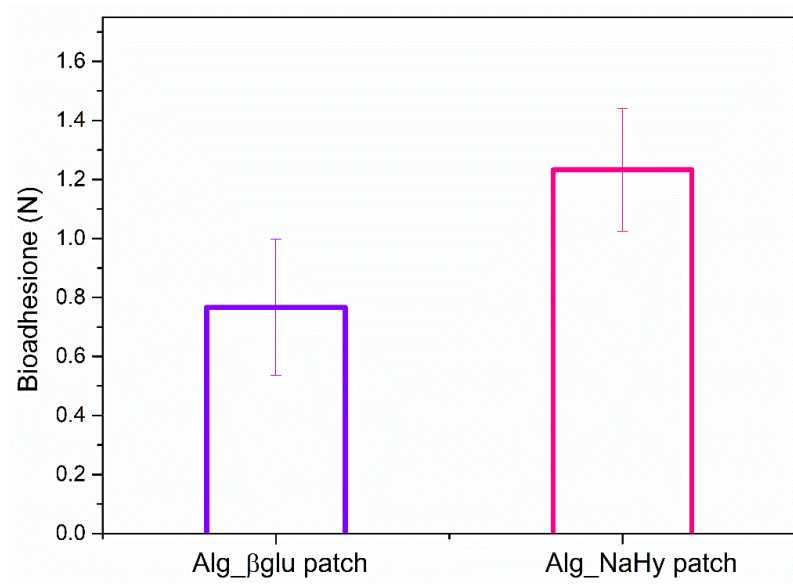


Figure 3.33. Bioadhesion force (N) (\pm SD) of Alg_beta glu and Alg_NaHy patches.

4. TPS filaments optimization suitable for FDM printing

4. TPS filaments optimization suitable for FDM printing

4.1. TPS filaments optimization suitable for FDM printing

FDM technique is based on extrusion of a filament through a nozzle and deposited layer by layer on the build plate of the 3D printer. These filaments are produced by hot melt extrusion (HME) (138,139). In order to be printed by FDM technique, they require suitable properties such as uniform dimension (1.75 mm diameter), mechanical and thermal properties. The latter aspect is very important as the filaments are subjected to high temperatures during both extrusion by HME and FDM. FDM is a fast-growing technique useful in pharmaceutical field for the production of customized solid dosage forms such tablets, capsules, suppositories (66,67). Moreover, FDM is a solvent-free process with continuous production and good integration of the active pharmaceutical ingredient (API) into the filament. The main disadvantage is the high working temperature that limits the use to thermostable drugs. Synthetic polymers such as PLA and PCL have been largely employed for the production of mechanically strong implant and bone tissue engineering scaffolds (140,141).

Considering the limitations in the use of synthetic polymers due to recent restriction introduced from the UE regulation 2023/2055 about microplastics, it is necessary to find suitable alternative in biopolymers (142). In literature few studies are reported about the production of filaments based on biopolymers (such as potato starch and cellulose) (143,144). In recent years, there has been a growing interest in the use of starch-based thermoplastic filaments (TPS) as a biodegradable polymer (145).

The main limitation is the use of starch as polymer for filaments production is represented by poor mechanical properties and low melting point.

The aim of this research was to develop TPS filament mixed to different additives, such as plasticizer and minerals, in order to improve starch mechanical and thermal and make it suitable for FDM printing.

As additives they were used: halloysite (HAL), montmorillonite (MMT), citric acid (CA), magnesium stearate (MgSt).

Starch (previously described in *Section 3.1.*) offers a new economical perspective as biodegradable polymer due to its high availability, renewable origin and biocompatibility (146,147). In its native form, starch is not processable as a thermoplastic since it degrades without melting, thus being necessary to add plasticizers to induce its gelatinization, as well as improve its thermal and mechanical properties (148). For this purpose, based on literature data, TPS was combined to Gly as plasticizer (30% w/w) and

4. TPS filaments optimization suitable for FDM printing

extruded to form TPS filament, adjusting processing conditions (**Table 4.1**). During this process, the starch granules lose their crystallinity and finally result in an amorphous material (149,150). In contrast to commonly used thermoplastic polymers, TPS has three primary drawbacks, namely suboptimal mechanical qualities, limited heat stability, and high-water sensibility. This can be solved by:

- i) Combine starch to different types of fillers (151),
- ii) chemical modification of starch (esterification and cross-linking),
- iii) starch blending with other thermoplastic polymers like PVA.

Regarding the addition of fillers, clays were considered useful additives due to their natural origin and non-polluting character. MMT is a layered aluminosilicate mineral whose structure consists of two tetrahedral silica sheets (SiO_4) sandwiching an octahedral alumina (AlO_6) layer (**Figure 4.1A-C**) (152).

Clays or phyllosilicates are hydrated aluminosilicate minerals composed of Al and Si oxides and other cations such as Mg, K, Ca, Na and Fe. They are formed by continuous tetrahedral and octahedral sheets stack on each other. Each tetrahedral stratum (T) consists of Si^{4+} coordinated to 4 oxygens, while the octahedral stratum (O) is formed by the coordination of metal cations (Mg, Al, Fe, Li, among others) with oxygen, OH^- or F^- of the tetrahedral sheet. The T and O sheets are associated with the apical oxygen atom of the tetrahedral one, producing 1:1 (also known as T:O) or 2:1 (or T:O:T) phyllosilicates. In the particular case of layered clay minerals like MMT, it is possible to find an “interlayer space” between each T:O or T:O:T stack which is occupied by interchangeable metal cations, responsible for the main properties of this mineral: swelling capacity, rheological modifiers, moisture-retaining, cation exchange capacity (CEC) and adsorption properties. These properties have found useful applications in health (153). MMT chemical formula is $(\text{M}_x (\text{Al}_2\text{-yMg}_y) \text{Si}_4\text{O}_{10} (\text{OH})_2 \text{nH}_2\text{O})$ (154). In its natural origin, MMT is called “bentonite” due to the presence of secondary mineral phases.

HAL is a bilayer aluminosilicate with a chemical composition similar to kaolinite and its chemical formula is $\text{Al}_2\text{Si}_2\text{O}_5 (\text{OH})_4\text{-nH}_2\text{O}$. Its tubular structure is in the sub-micrometre range (2-10 μm) (**Figure 4.1D-F**) (152). HAL is a 1:1 phyllosilicate consisting of an octahedral geometry layer interspersed with a planar T layer, linked by oxygen bridges. Three octahedrons constitute the fundamental unit of the octahedral sheet (155). Due to HAL crystalline structure as nanotubes, it exhibits different chemical compositions on their outer and inner surfaces. The outer surface is composed of siloxane groups (Si-O-Si) and a small number of Al-OH and Si-OH on the edges, bestowing it with

4. TPS filaments optimization suitable for FDM printing

a negative net charge. The inner surface of the nanotube is composed of aluminol groups (Al-OH), which contribute a positive charge. The variation of charges can be attributed to the different dielectric and ionization characteristics of silicon oxides and aluminum (156).

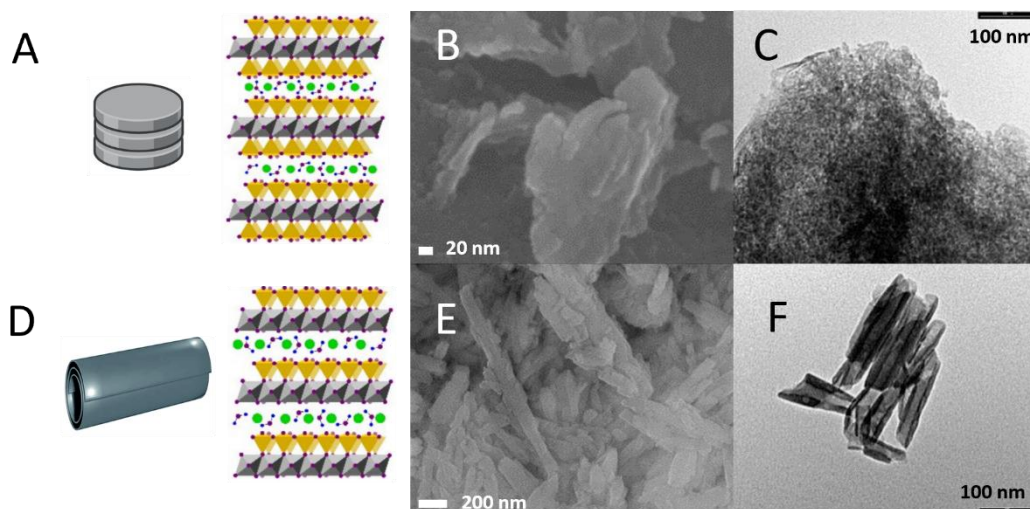


Figure 4.1. Schematic representation of MMT lamellar structure (A)(157); MMT micrograph (magnification 500K X) obtained by SEM (B); MMT micrograph obtained by TEM (C); schematic representation of HAL tubular structure (D); HAL SEM micrograph (magnification 100K X) (E); TEM micrograph of HAL (F).

The clays (MMT and HAL) (33) have been described as biocompatible materials, even reporting proliferative activity. Both minerals are abundant in nature, affordable, and non-toxic, which makes them highly interesting in the pharmaceutical field. Several characteristics exhibited by these substances have practical implications in this field, among them, their significant adsorption capacity, high CEC, and chemical inertness. Clay minerals can be frequently used as excipient or active ingredients. As excipients they play an important role as organoleptic enhancers, lubricants, dispersing agents, gel-forming, emulsifying, and thickening agents. Additionally, there has been a wide academic focus on the advancement of drug delivery and transportation mechanisms by integrating drugs with clay minerals (156), also improving their physicochemical properties.

Natural organic ingredients like CA have also proven to be useful in the improvement of TPS physicochemical properties of TPS (158). CA is a weak

4. TPS filaments optimization suitable for FDM printing

tricarboxylic acid and its chemical formula is $C_6H_8O_7$. It has interesting properties for the pharmaceutical field (19) due to its biocompatibility, versatility, and environmentally friendly chemistry (159). It is present mainly in citrus fruits as lemons but it can also be obtained from microbes (such as some fungi as *Aspergillus*) through fermentation processes, substrates and microorganisms, this being the main current CA source (160). In the pharmaceutical and food industries, CA has traditionally been used as flavoring, buffering, antioxidant, and chelating agent (159). In fact, due to the acidic nature of CA it can interact with polymers and reduce their brittleness, promoting the dissolution of starch granules. When combined to Gly, it induces the rupture of inter and intra-molecular H bonds, thus plasticizing starch under shear and temperature conditions, enabling the obtention of homogeneous and less frail filaments (158,161).

Another crucial aspect for the production of TPS filaments is the flowability of the pristine ingredients during the extrusion process to give rise to the final filament. In this regard, the addition of lubricants is a key step. Therefore, MgSt was added to the mixture for the production of the filaments. MgSt is the magnesium salt of stearic acid. It is also natural ingredient commonly used as an anti-caking excipient commonly used in cosmetics, food and pharmaceutical formulations, proving also its usefulness in the processability of materials during extrusion processes (162).

Finally, since the final objective is the production of patches for wound healing, the presence of active substances is required. The active ingredients to be introduced must be stable and resistant to the working conditions of the production technique which in this particular case entail high temperatures both during the generation of the filament and during the FDM printing technique. Among the possible candidates, MSM was chosen as model molecule both for its thermostability, and for its suitability for topical administration as it possess anti-inflammatory and antioxidant properties (163). MSM ($(CH_3)_2SO_2$, **Figure 4.2**) is an organosulfide, member of the methyl-S-methane compound within the Earth's sulfur cycle. MSM is found as traces in plants, animals, and humans, but it can be synthetically produced through DMSO oxidation with hydrogen peroxide (H_2O_2) and subsequently purification by either crystallization or distillation. Prior to its clinical use, it mainly served as a polar, aprotic, high-temperature commercial solvent (163).

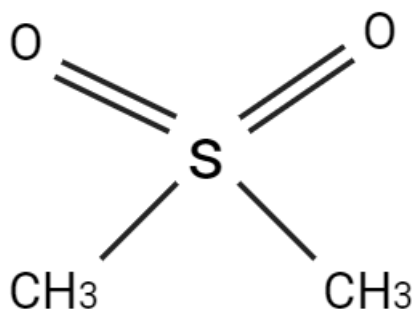


Figure 4.2. MSM chemical structure.

4.2. Materials

CS and MSM were purchased from A.C.E.F. (Fiorenzuola d'Arda PC, Italy). Gly, HAL, MMT, MgSt and CA were purchased from Sigma-Aldrich (Milano, Italy).

For biological studies, all the tested strains were bought from Microbiologics, St. Cloud, MN, USA, except for *Propionibacterium acnes* which was bought from Mecconti S.A.R.L. Sp. z o.o., Warsaw, Poland.

Test media were prepared as mentioned in *Section 3.2*.

4.3. Methods

4.3.1. TPS filaments preparation

The previously described materials (MMT, HAL, CA, MgSt, MSM) were combined for the preparation of the TPS filaments by hot melt extrusion (HME). These additives have a great potential to enhance the extrusion process, water absorption, crystallinity, thermal properties, and antimicrobial activity of the TPS filament to target applications in the healthcare field. Thus, the filaments reported in **Table 4.1** were prepared and characterized in order to find the most suitable for patch production by FDM technique.

Table 4.1. TPS filaments composition.

Filaments	CS% (w/w)	Gly% (w/w)	HAL (phr*)	MMT (phr)	CA (phr)	MgSt (phr)	MSM (phr)
F0	70	30	-	-	-	-	-
F1	70	30	2	-	-	-	-
F2	70	30	-	2	-	-	-

4. TPS filaments optimization suitable for FDM printing

F3a	70	30	-	-	3	-	-
F3b	70	30	-	-	3	2	-
F4	70	30	-	2	3	2	-
F5	70	30	-	2	3	2	2.5

***phr**: parts % resin.

TPS filaments were prepared using a three-steps process. In the first step, the main components of the matrix (CS and Gly) were mechanically mixed during 15 min at 450 W until a homogeneous mixture was obtained. All the mixtures have been prepared using CS/Gly mass ratio of 70/30 (w/w) (**Figure 4.3A**). In the second step, the CS/Gly mixtures were combined with the rest of the ingredients in the following order, as shown in **Figure 4.4**, by using a co-rotating twin-screw extruder Micro Compounder 5 & 15cc from DSM (XploreInstruments BV, Sittard, The Netherlands), the screw speed set at 30 and 120 rpm. During this process, the barrel temperatures of the extruder were set at 135, 140 and 145°C for zones 1, 2 and 3, respectively (**Figure 4.3B-C**). In the third step, a second extrusion was performed using a desktop Pellet Filament Extruder (Extruder Line II+ ROBOTDIGG LIMITED) to obtain filaments formulations suitable for FDM 3D printing extrusion (with the desired 1.75 mm diameter). The barrel temperatures of the extruder were also controlled at 120 and 140 °C for zones 1 and 2, respectively (**Figure 4.3D, E and F**). Finally, the obtained filaments were stored in oven at 40°C for two weeks under a RH of 40% before use.

4. TPS filaments optimization suitable for FDM printing

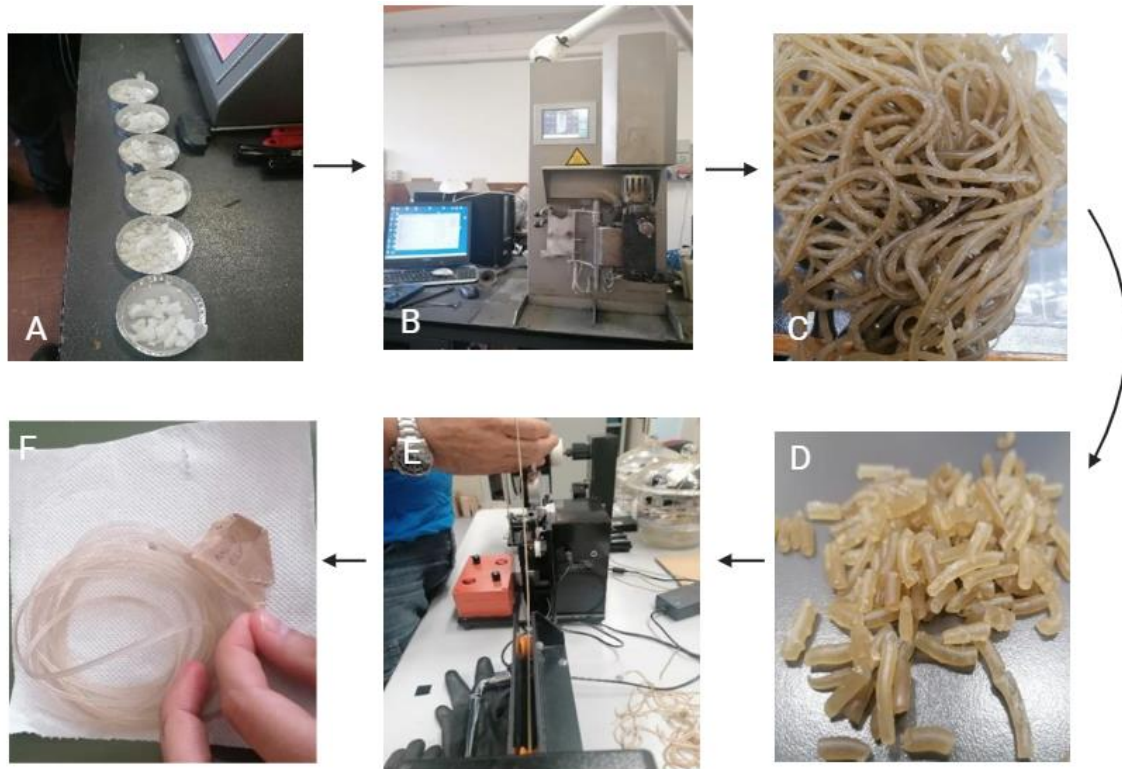


Figure 4.3. Physical mixture (A); co-rotating twin-screw extruder (B); filament obtained after the first extrusion (C); filament after cutting for second extrusion feeding (D); desktop Pellet Filament Extruder (E); final filament with the desired diameter (1.75 mm) (F).

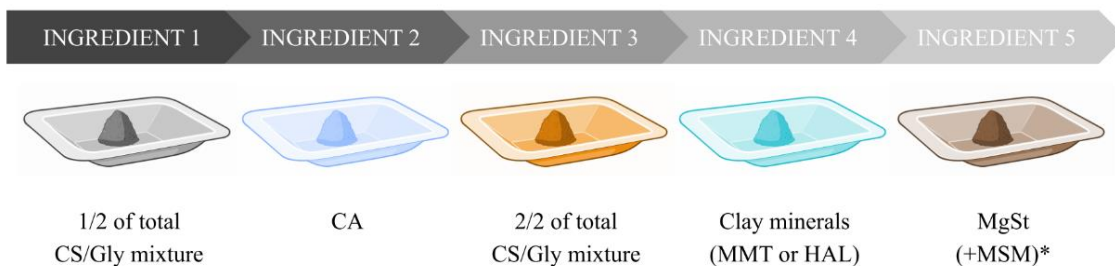


Figure 4.4. Sequence of addition of ingredients. *Sample with MSM was added at the same time of MgSt.

4.3.2. TPS filaments characterization

SEM

For detailed information about SEM methodology, see section 3.3.4.

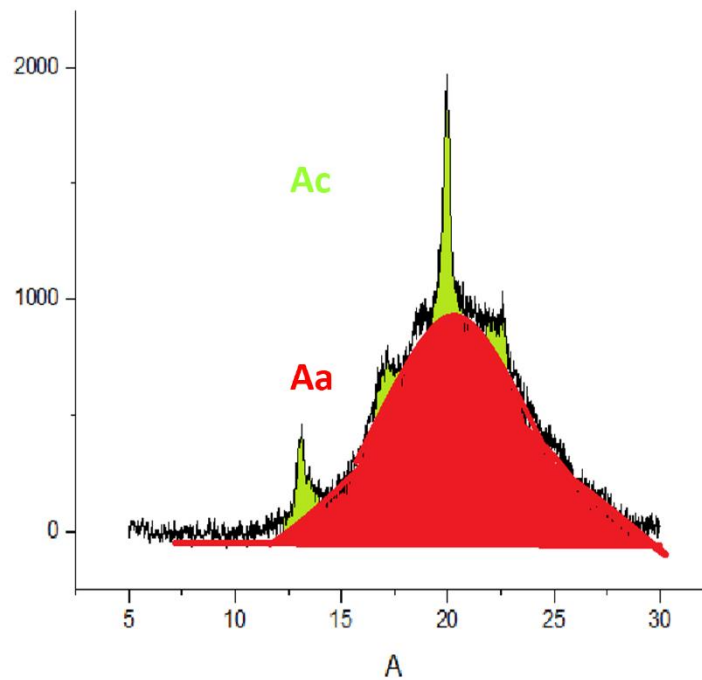
FT-IR

For detailed information about FT-IR methodology see section 3.3.4.

X-Ray Powder Diffraction (XRPD)

Filaments were firstly dried at 40°C for 24 h and then pulverized by a knife mill (for 2 min at 40 rpm) prior to XRPD analyses. The study was carried out by using a PANalytical X'Pert diffractometer equipped with an X'Celerator solid-state detector and a sample holder spinning. XRDP patterns were recorded by using random oriented mounts with CuK α radiation, at 45 kV, 40 mA, in the range 3 to 50° (2 θ). The estimation of the solid composition in crystalline phases was obtained by X'Pert HighScore Plus (PANalytical, 2005). The crystallinity was calculated (**Eq. 4.1**) as the ratio of area under the crystalline peaks to the entire area of under the diffractogram as shown in **Figure 4.5** (164,165).

$$X_c = \left(\frac{A_c}{A_c + A_a} \right) \times 100 \quad \text{Eq. 4.1.}$$



4. TPS filaments optimization suitable for FDM printing

Figure 4.5. Area of the crystal and non-crystal regions (amorphous). A_c = areas of the crystal regions. A_a = area of the non-crystal regions (amorphous).

Thermal properties

The thermal profiles were studied by Differential Scanning Calorimetry (DSC) using a Q200 (TA Instruments) and Thermogravimetric Analysis (TGA) using a Seiko instrument (see model in *Section 3.3.4.*). DSC measurements were carried out from 30 to 600°C at 10°C/min. Each sample was scanned 3 times. TGA measurements were performed over a range of temperatures from 30 to 900°C in nitrogen atmosphere.

Swelling capacity

The capacity of the filaments to absorb exudates was evaluated in vitro by the measurement of both hydration percentage (%) and dissolution capacity (DS%) calculated by **Eq. 3.2** and **Eq. 3.3**, respectively (*see section 3.3.4.*).

An accurately weighed sample (W1) for each filament was immersed in simulated wound fluid (SWF) (1 ml) inside an Eppendorf and kept at $32.0 \pm 0.1^\circ\text{C}$. At predetermined time intervals (1, 8, 16 and 24 hrs) the sample was wiped using filter paper to remove the excess of SWF and weighted (W2). Then it was dried in an oven at 37°C for 48 hrs and reweighted (W3) (114).

4.3.3. Biological properties

Antimicrobial Activity Assay

The antibacterial activity of the samples was evaluated against 15 strains, including Gram + bacteria, Gram - bacteria and yeasts. The experiments were performed using agar well diffusion technique (166,167). For each strain an initial suspension of 0.5 McFarland in 0.9% sterile saline solution was prepared and 100 μl were distributed on MHA/MHAB plates by a swab. Then, 30 mg (diameter 3 mm) of each filament were placed on the inoculated plates and then incubated according to the growth conditions shown in **Table 4.2**. After the incubation time, the presence and the diameter of the inhibition halo was measured by a gauge.

4. TPS filaments optimization suitable for FDM printing

Table 4.2. Strains tested and growth conditions.

	Strain	Growth Conditions
GRAM + bacteria	<i>Enterococcus faecalis</i> WDCM 00087	37 °C for 24 ± 2 h in MHA
	<i>Enterobacter cloacae</i> WDCM 00083	37 °C for 24 ± 2 h in MHA
	<i>Staphylococcus epidermidis</i> WDCM 00036	37 °C for 24 ± 2 h in MHA
	<i>Staphylococcus aureus</i> WDCM 00034	37 °C for 24 ± 2 h in MHA
	Methicillin-resistant <i>Staphylococcus aureus</i> ATCC BAA-1708	30 °C for 24 ± 2 h in MHA
	<i>Bacillus subtilis</i> WDCM 00003	37 °C for 24 ± 2 h in MHA
	<i>Bacillus cereus</i> WDCM 00001	30 °C for 24 ± 2 h in MHA
	<i>Streptococcus pyogenes</i> ATCC 19615	37 °C for 24-48 h in MHAB
	<i>Propionibacterium acnes</i> ATCC 11872	37 °C for 48-72 h under anaerobic conditions in MHAB
	<i>Clostridium perfringens</i> WDCM 00007	37 °C for 24-48 h under anaerobic conditions in MHAB
GRAM - bacteria	<i>Pseudomonas aeruginosa</i> WDCM 00025	25 °C for 24 - 48 h in MHA
	<i>Klebsiella pneumoniae</i> WDCM 00097	37 °C for 24 ± 2 h in MHA
	<i>Proteus mirabilis</i> WDCM 00023	37 °C for 24 ± 2 h in MHA
	<i>Escherichia coli</i> WDCM 00013	37 °C for 24 ± 2 h in MHA
Yeast	<i>Candida albicans</i> WDCM 00054	25 °C for 48-72 h in MHA

4.3.4. Prototypes patches preparation

4.3.4.1. Selection of printing parameters and digital design

In order to evaluate the suitability of the prepared filament for extrusion by FDM, prototypes patches were prepared by means of a Creality 3D Ender-3 V2 (Shenzhen Creality 3D technology Co., China) (**Figure 4.6**).

Circular patches of 2 cm diameter were designed using CAD software (OnShape education) and exported as .stl files. The .stl file was then imported into a slicer software (Ultimaker Cura 4.13.1). Slicing parameters such as nozzle diameter, layer height, top and bottom width, flow rate, fan speed and print temperature and speed were pre-established (**Table 4.3**).

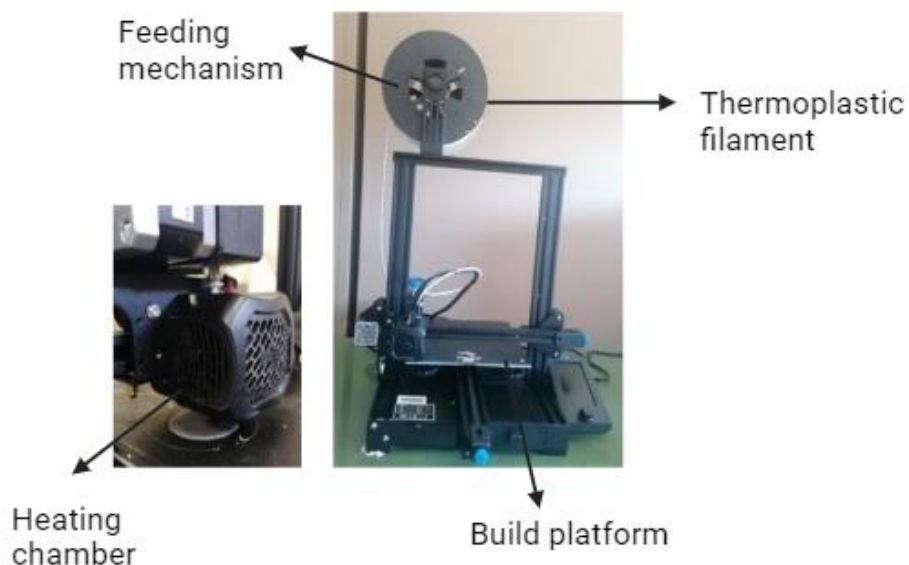


Figure 4.6. Creality 3D Ender-3 V2.

Table 4.3. Studied printing setting.

Parameters	Values	Units
Nozzle diameter	0.4-0.8	mm
Printing temperature	150 – 300	°C
Build plate temperature	80	°C
Layer height	0.2 - 0.3	mm
Top/bottom thickness	0.1 – 0.3	mm
Flow rate	15-97	%
Fan speed	0-100	%
Print speed	5-60	mm/s
Infill density	100	%

Printing temperature and nozzle diameter

FDM technique requires the filament is melted or softened and deposited layer by layer to produce dosage forms. The minimum temperature required to achieve melt/deposition must be optimized without causing degradation of the polymers and drug used. Generally, the required temperature is higher than the temperature used in HME. Printing temperatures were evaluated from 150 to 300°C. The melted filaments must pass through a narrow nozzle (0.4, 0.6 and 0.8 mm) of the FDM 3D printer before being deposited on the build plate (168).

Build plate temperature

4. TPS filaments optimization suitable for FDM printing

Printed object (patch or scaffold in this study) is deposited layer by layer being necessary to remain in attached to the build plate of the 3D printer until the production of patch is complete. A wrong temperature causes the failure of the printing process, as the printed patch is incomplete due to the lack of contact with the build plate. On the other hand, an excessively high build plate temperature does not allow effective cooling and solidification of the overlapping layers causing a collapse of the patch structure. Therefore, it is necessary to achieve adhesion between the build plate and printed patch by setting a specific temperature based on the thermal characteristics of the polymer (CS) and of the active ingredient (MSM) used in the filament formulation (168). Following these considerations, the build plate temperature was fixed at 80°C.

Layer height

Layer height affects resolution and smoothness of the dosage form. Patch printed with lower layer heights give improved mechanical properties and higher strength, however, require more printing time (168). In this study it was set at 0.2 mm to better adapt to the skin.

Top/bottom thickness

Top and bottom thickness affect significantly both physical properties as well as in vitro release characteristics of the API of the printed dosage forms (168). It was evaluated at 0.1 and 0.3 mm.

Flow rate

See previous chapter 3.3.3.1 for detailed description. In this study, was evaluated in a range of 15 % to 97 %.

Fan speed

Fan speed controls how quickly the hot filament cools as it is extruded onto the build plate, thus influencing the quality and strength of the printed object. It was evaluated from 0 to 100 %.

Print speed

Time required to produce a single dosage form depends on printing speed. The quality of the printed patches depends on the choice of printing speed, as high speeds

result in low quality objects, and low speeds require more printing time to obtain the final object. In addition, at high speeds the filament could fracture during the printing process. Also, this parameter influences on the thickness of the printed object, since at high speeds, it tends to decrease (169). Print speeds were evaluated from 5 to 60 mm/s.

4.4. Results and discussion

TPS filaments could be a useful starting material for the production of sustainable formulations by FDM 3D printing. However, it presents some limitations such as: i) poor mechanical properties, ii) low thermal stability and iii) high water sensibility. For this reason, it was necessary to introduce in the composition some additives in order to overcome these problems. With this aim HAL, MMT, CA, MgSt were used. MSM was selected as model molecule to be used for the production of loaded filaments. Filaments for FDM printing are generally produced by HME. This method is divided into two extrusion processes, during the first extrusion takes place the plasticization of the starch and the melt compounding with the other additives. The obtained filaments show a diameter too large compared to that necessary for FDM printing thus, a further processing step is necessary. During the second extrusion process, it is possible to achieve the suitable diameter (170). The accuracy of filament diameter is essential for the FDM printing process. The suitability of a mixture for the FDM process depends on the ingredients and the order in which they are introduced in the starting mixture, the conditions under which it is processed and the uniform dispersion of fillers and plasticizers in the filaments during the extrusion process. The filaments commonly used in FDM 3D printing should be 1.75 ± 0.50 mm in diameter. In literature (170), the diameter used ranges 1.54 to 1.90 mm. Filaments that are too small or too large can produce under- or over-extrusion, which can compromise the quality of the printed object (170). A close tolerance on the diameter is essential during melting and depositing of materials. Despite this, there is still limited research about the use of proper diameter of 1.75 ± 0.50 for each filament, except for F3a, which was shown to be non-uniform in diameter along the filament, probably due to the addition of CA without other additives (**Figure 4.7**). However, this suitable diameter was affected by environmental humidity, so specific storage conditions for the filaments should be set (for 2 weeks under 40% RH).

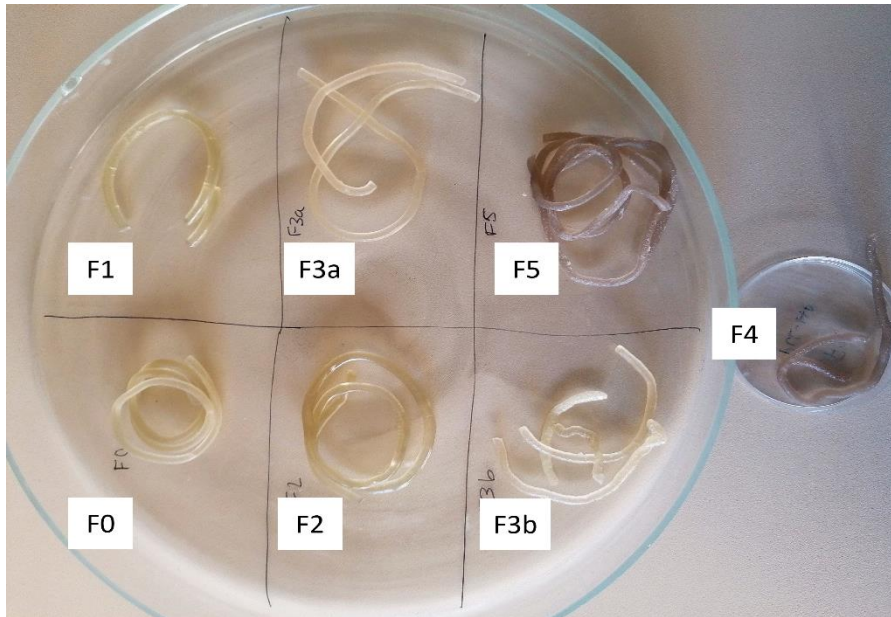


Figure 4.7. TPS filaments image.

4.4.1. TPS filaments characterization

Macroscopic appearance and SEM

The SEM micrographs of TPS (F0) and TPS with different additives (F1-F5) are reported in **Figure 4.8** and **4.9**. As a representative sample of the TPS filaments, F0 micrographs showed a homogeneous surface and a compact structure, but some agglomerations ascribable to starch can be appreciated. The addition of HAL (F1) and MMT (F2) resulted in more homogeneous aspect of the filaments, both in the surface and in the transversal section. This effect can be related to the deagglomeration effect of HAL and MMT fillers in the TPS (171). Moreover, it also demonstrates the uniform dispersion of both HAL and MMT particles, guaranteeing more reproducible filaments. In any case, since MMT produced more homogeneous results, HAL was discarded. F3b sample showed higher surface homogeneity than F3a sample, this is probably due to the addition of MgSt that improved the flowability and so, the extrusion processability of TPS, as supported by the literature (172,173). The presence of CA (F3a, F4 and F5) produced discontinuities in form of pores within the filaments, probably due to the differential melting and decomposition temperatures of this ingredient (174). F4 filament showed a smoother surface and less agglomeration inside the transversal section due to the presence of both MMT and MgSt. The aspect of F5 sample was very similar to F4, indicating that the active ingredient (MSM) did not interfere with the filament processability and apparently showed a homogeneous distribution within the filament matrix **Figure 4.8**. In

4. TPS filaments optimization suitable for FDM printing

F4 and F5 filaments, CA produced more homogeneous porosity, with smaller pore diameters, demonstrating that the combination of all the additives can counteract undesirable filament discontinuities. Therefore, the incorporation of CA into formulations, combined with the herein used additives, could appear as a possible strategy in the development of TPS with controlled porosity. This could be particularly interesting in the design of patches with modified drug release features.

The colour of the filaments is different, as shown in the column of the images of **Figure 4.9**. For F0, F1 and F3a it is translucent yellow, while for F2 and F3b appeared as dark yellow, while F4 and F5, were opaque, due to the addition of the MMT.

4. TPS filaments optimization suitable for FDM printing

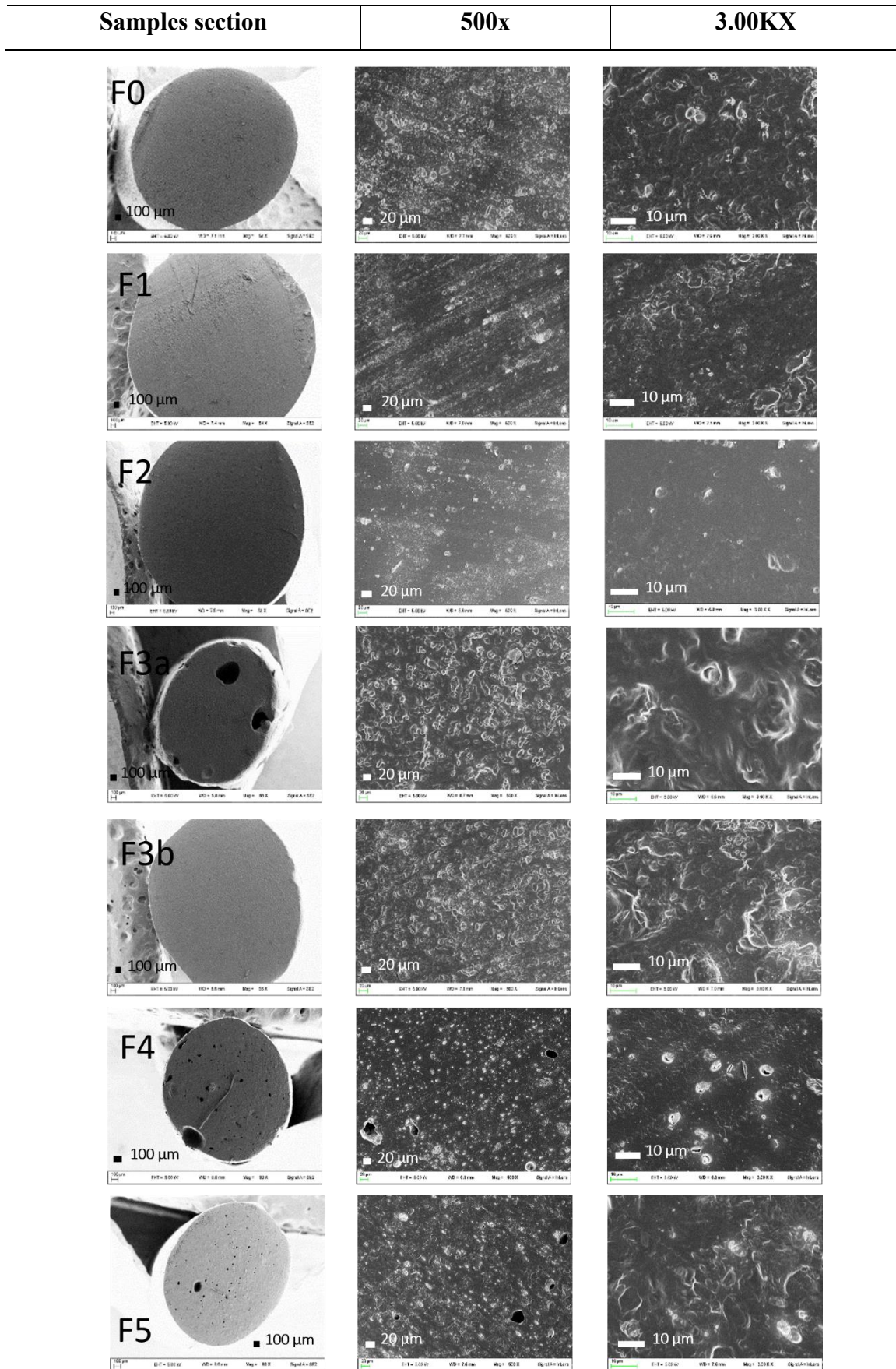


Figure 4.8. Section micrographs of TPS filaments F0, F1, F2, F3a, F3b, F4 and F5. Magnifications 500X and 3.00K X.

4. TPS filaments optimization suitable for FDM printing

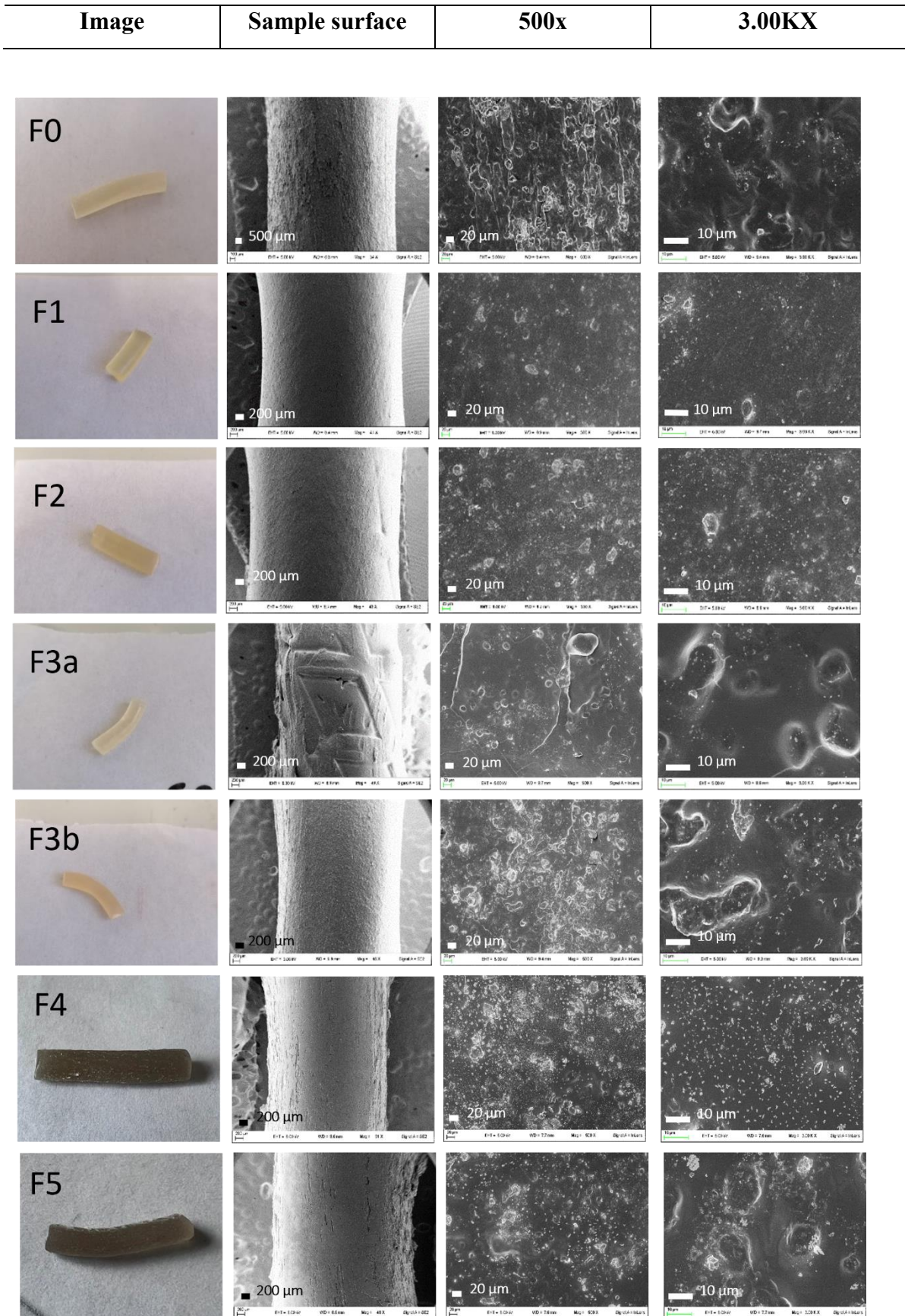


Figure 4.9. Image and surface micrographs of TPS filaments F0, F1, F2, F3a, F3b, F4 and F5, respectively. Magnifications 500X and 3.00K X.

FT-IR

The **Figure 4.10A** shows characteristic bands of the FT-IR spectra for pure CS and TPS at 30 % (w/w) Gly (F0). The starch chains are linked by glycosidic bonds. The amylose chains have a linear structure formed by glucose residues linked by α -1,4-glycosidic bonds, and in the case of branched amylopectin, there are additionally α -1,6-glycosidic bonds, as already mentioned in the section 3.3.1. The FT-IR spectrum of CS shows a band in the region 920-938 cm^{-1} from oscillations of α -1,4-glycosidic and α -1,6-glycosidic bonds. If the amylopectin content is higher, i.e., if the α -1,6-glycosidic bond is larger, the characteristic band shifts to a greater extent toward higher wavenumbers. As a result, the effect of Gly, shear forces and high temperature during the extrusion process, intramolecular and intermolecular hydrogen bonds between the hydroxyl groups of the CS chains have been affected. Instead of these bonds, more stable hydrogen bonds are created between the -OH groups of CS and Gly. In the CS spectrum, the 3302 cm^{-1} band, related to hydrogen bonds, is shifted to 3291 cm^{-1} in the case of TPS. According to the harmonic oscillator model, the wavenumber at which the characteristic bands of a specific group of atoms decreases with increasing interaction strength of the molecule (175). After the plasticization process, the band of glycosidic bonds in the TPS spectrum shifts from 925 cm^{-1} to 916 cm^{-1} . This means that, when CS is subjected with the Gly shear forces and temperature influence the material, α -1,6-glycosidic bonds are broken, reducing their wavenumber. Characteristic changes in the spectrum of TPS compared to CS also occur in the 900-1200 cm^{-1} region. In this range, in the FTIR spectra of CS the bands related to C-O stretching vibrations in C-O-H groups are at 1078 cm^{-1} and 1148 cm^{-1} and the band originating from C-O stretching vibrations in C-O-C groups at 925 cm^{-1} . Both of the above groups can form hydrogen bonds with Gly, which causes these bands to shift to a lower wavenumber. Finally, a band appears around 1640 cm^{-1} , originating from the bending oscillation of the -OH groups of the water molecules adsorbed by the amorphous regions of the CS granules (176).

Figure 4.10B shows the FT-IR spectra of the 30 % Gly TPS (F0) and TPS modified (F1-F5) to identify the functional groups of the samples. An absorption band at 3291 cm^{-1} corresponding to the hydroxyl (-OH) groups of CS, while the bands at 2917 and 2878 cm^{-1} belong to the methyl (C-H) bond stretching vibration of the polysaccharide, according to Paluch *et al* (177). The band at 1712 cm^{-1} corresponded to the functional

4. TPS filaments optimization suitable for FDM printing

group (C=O), while that at 1365 cm^{-1} is due to the (C- H) vibration and the C-O stretching of the C-O-H groups of CS produced bands at 1143 and 1067 cm^{-1} (178). The spectra of TPS modified were almost superimposable to the whole range of the TPS spectrum at 30 % Gly. This may be due to the low penetration of the FT-IR ATR technique together with the small concentrations of the different additives.

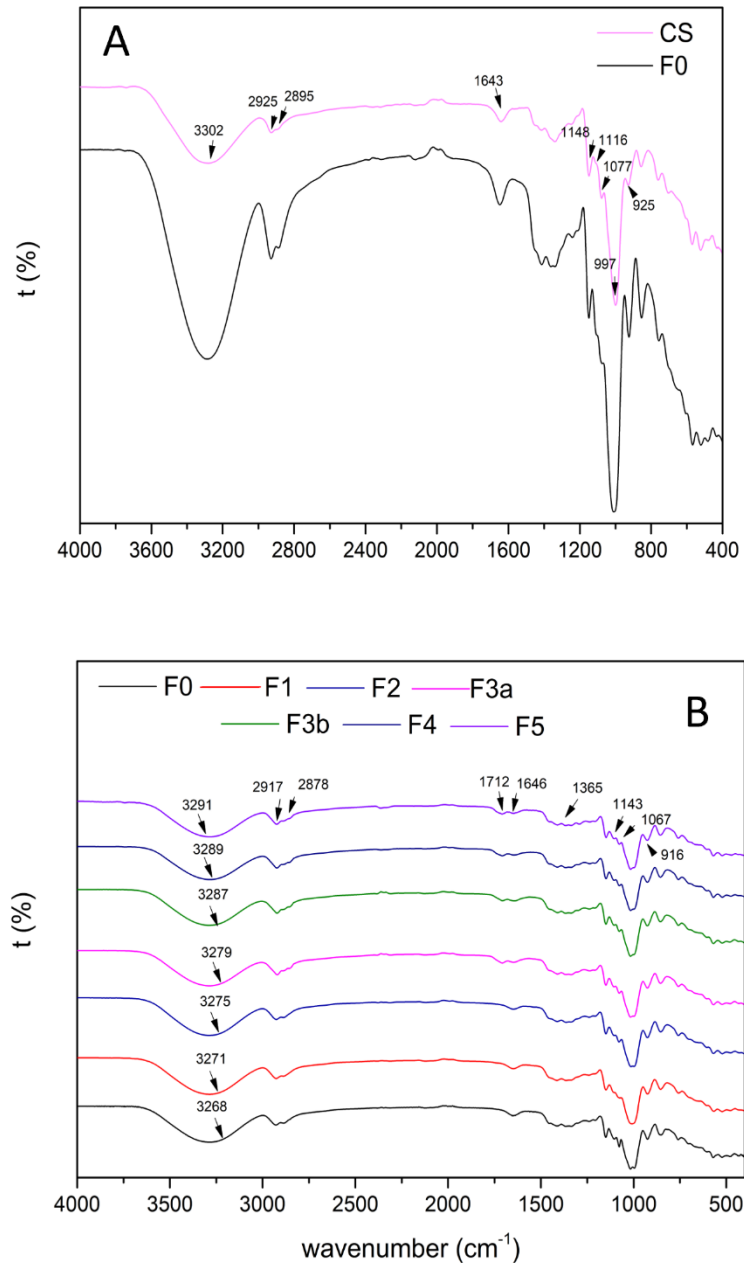


Figure 4.10. FT-IR spectra of (A) CS and TPS 30 % Gly (F0) and (B) TPS filaments with different additives.

XRPD

The crystallinity of TPS filaments with different additives is gathered in **Table 4.4** and represented in **Figure 4.11**. According to literature (179,180), after extrusion processing of TPS filaments, two types of crystallinities can be observed: i) A- type (resulting from incomplete melting of the starch granules during the extrusion process); and ii) V_H -type (resulting during thermo-mechanical extrusion process). As it can be seen in **Figure 4.11**, a predominance of crystallinity V_H -type with 3 characteristic signals $2\theta = 13^\circ$, 20° and 22.5° was observed.

In agreement with Ghanbari. A *et al.* (151), the main diffraction peaks visible in all the XRDP patterns can be ascribable to the plasticizing process of CS with Gly. The main reflection in each diffractogram at $2\theta = 23.0^\circ$, 17.3° , 20.0° , 18.3° and 20.4° for F0, F1, F2, F4 and F5, respectively, suggested that the crystalline structure of each filament follows V_H -type pattern (151). The presence of MMT, present in F2, F4 and F5 can be confirmed by weak diffractions at $2\theta = 7.0^\circ$ and 27.4° . HAL possess a reflection around $2\theta = 13.0^\circ$, which in this case coincides with a reflection ascribable to other ingredients (probable CS or Gly), being therefore, masked. No other mineral diffractions are detectable, probably due to the low amount of MMT and HAL in the total filament composition. MSM is not detectable due to its amorphous form, since during the preparation process this active is melted.

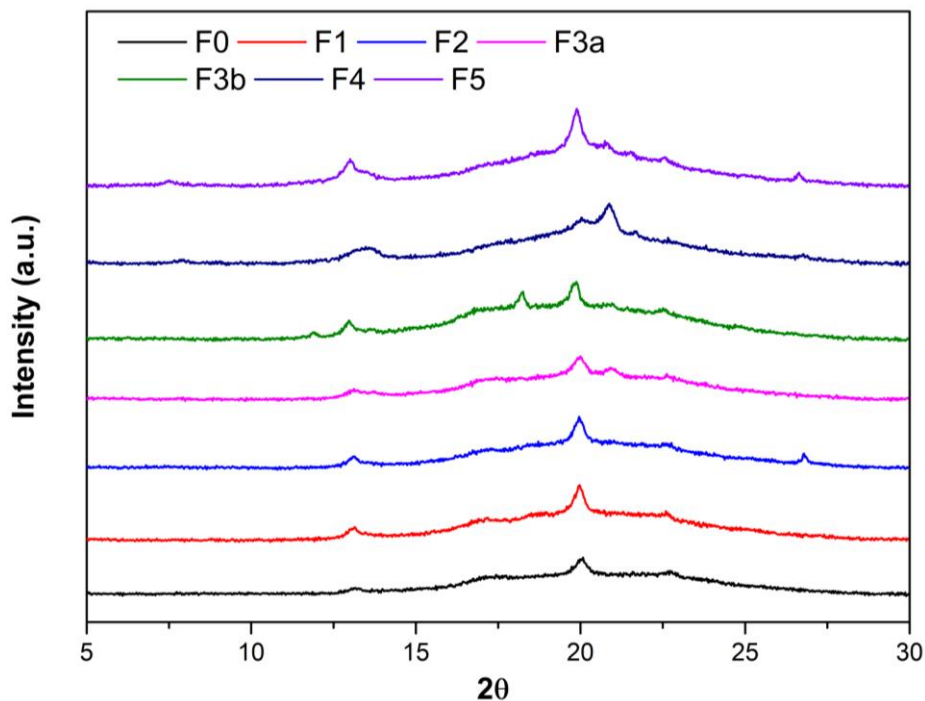


Figure 4.11. XRDP of each filament (F0, F1, F2, F3a, F3b, F4, F5)

4. TPS filaments optimization suitable for FDM printing

Regarding the crystallinity (**Table 4.4**), samples F1 and F5 showed smaller crystallinity values with respect to F0. F3b showed the lowest crystallinity as a result of the incorporation of MgSt. This effect was attenuated in samples F4 and F5 due to the presence of crystalline phases (MMT). This result suggests that when CS is plasticized with Gly, clays have the possibility of interacting with polymeric chains of starch, increasing their dynamics, obstructing their rearrangement to a certain extent, and consequently preventing retrogradation of the polymeric matrix. This could be attributed to the fact that the filament has absorbed humidity from the environment, according to Camila. S *et al* (148). In addition, the results suggest that the addition of the different additives (CA, MgSt, MSM) also decrease the crystallinity of the samples (181). Particularly, CA has proven to increase the thermal profile and plasticization of TPS, ultimately slowing down the crystallization (158,161).

It should be underlined that the addition of plasticizing additives aimed to reduce the mechanical strength of the filament and favours its extrusion. In this sense, both Gly and MgSt fulfil this function (**Table 4.4**). The crystalline values in the presence of clays (F1, F2, F4, F5) are slightly higher than F3a and F3b due to the presence of particular crystalline minerals that do not melt during processing.

Table 4.4. Crystallinity values of each filament.

<i>Sample</i>	<i>X_c</i>
F0	23.0 ± 0.8
F1	17.3 ± 1.2
F2	20.0 ± 0.9
F3a	16.9 ± 0.7
F3b	13.4 ± 1.3
F4	18.3 ± 1.1
F5	20.4 ± 0.9

Thermal properties

DSC has been considered as a valuable method to quantify transition temperatures and it is possible to provide the parameters of the order-disorder transition occurring in semi-crystalline starch granules during gelatinization. Various microscopic techniques revealed that starch gelatinization was delayed to higher temperatures as the Gly

4. TPS filaments optimization suitable for FDM printing

concentration increased (182). In the presence of Gly (20 and 50% w/w) the peak temperatures of CS increased from 10.7 to 19.7°C, respectively, as reported in the literature (182).

The DSC curves of TPS and TPS modified can be seen in **Figure 4.12**. No sharp events can be seen in F0 apart from a wide endothermic event probably due to the combination of physisorbed water evaporation and melting of CS and Gly. CA has an endothermic event around 160 °C (183), which can be modified when combined with CS and other additives (thus explaining the results of F4 and F5). The endothermic event starting around 140 °C in F3b can be ascribed to the presence of MgSt, whose melting range has been reported to be around 120-150°C (184). This event can also be detectable in F4 and F5 (though overlapped with CA endothermal in the latter). No exothermic events are detectable in this temperature range, pointing out that no degradation events are occurring for any of the ingredients.

The first scan evidences the presence of an endothermic peak, due to the residual plasticization of the TPS based materials, that was almost complete in the case of drug containing F5 sample. Melting peaks at lower temperature (between 60 and 90 °C) can be ascribed to the melting of MgSt (recrystallized during the cooling step), that partially covered the signal related to TPS glass transition (T_g).

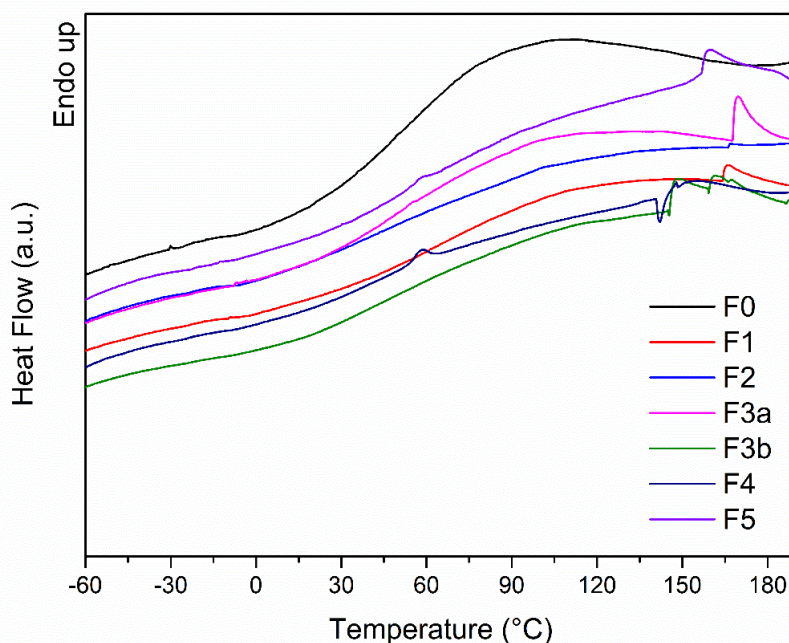


Figure 4.12. DSC profiles (first heating scan) of F0, F1, F2, F3a, F3b, F4 and F5 filaments.

4. TPS filaments optimization suitable for FDM printing

Figure 4.13A shows the TGA curves of TPS filaments and TPS filaments with different additives. Three main steps that take place in the ranges 60-250 °C, 250-350 °C and 350-600 °C are presented. The first ramp accounted in all cases for approximately 20% of weight loss, corresponding to evaporation of the physiosorbed water of the CS, in agreement with the DSC results (**Figure 4.12**). The second step, the main weight loss (65% of total mass), occurred from 250 to 350 °C, and it can be ascribed to polysaccharide decomposition. The delimitation of this stage was obtained in the derivative curve DTG (**Figure 4.13B**) that shows a well-defined peak, which suggests that this degradation happened as a single mechanism of decomposition. Finally, from 350 °C a slow weight loss occurs until reaching stability at temperatures higher than 600 °C. At these temperatures the degradation products of the previous event continue to degrade. The residual mass corresponded to inorganic components of TPS filaments (including CS and mineral phases MMT and HAL) (185).

The F0 filament showed higher weight losses with respect to the rest of samples in the first step due to the absence of additives. F1 profile is similar to F0 in the whole range, indicating that HAL does not improve the thermal resistance of the filament. On the contrary, the presence of MMT (F2) did seem to improve the thermal resistance, especially during the first weight loss step, initiating the second degradation step at slightly higher temperatures. This makes sense when looking at the TGA profiles of these clay minerals on their own, MMT having less weight loss than HAL (186,187). In fact, it has been reported that the addition of MMT increased thermal stability of filaments probably because of the interaction of MMT with CS, which made the internal structure of the molecule more compact (188). A higher mass loss was reported for F3a during the second step, noting that this additive is more labile (189). Nevertheless, this lability can be compensated by the addition of MMT, since the F4 and F5 filaments weight loss profile was similar to those without CA and even showed higher mass residual.

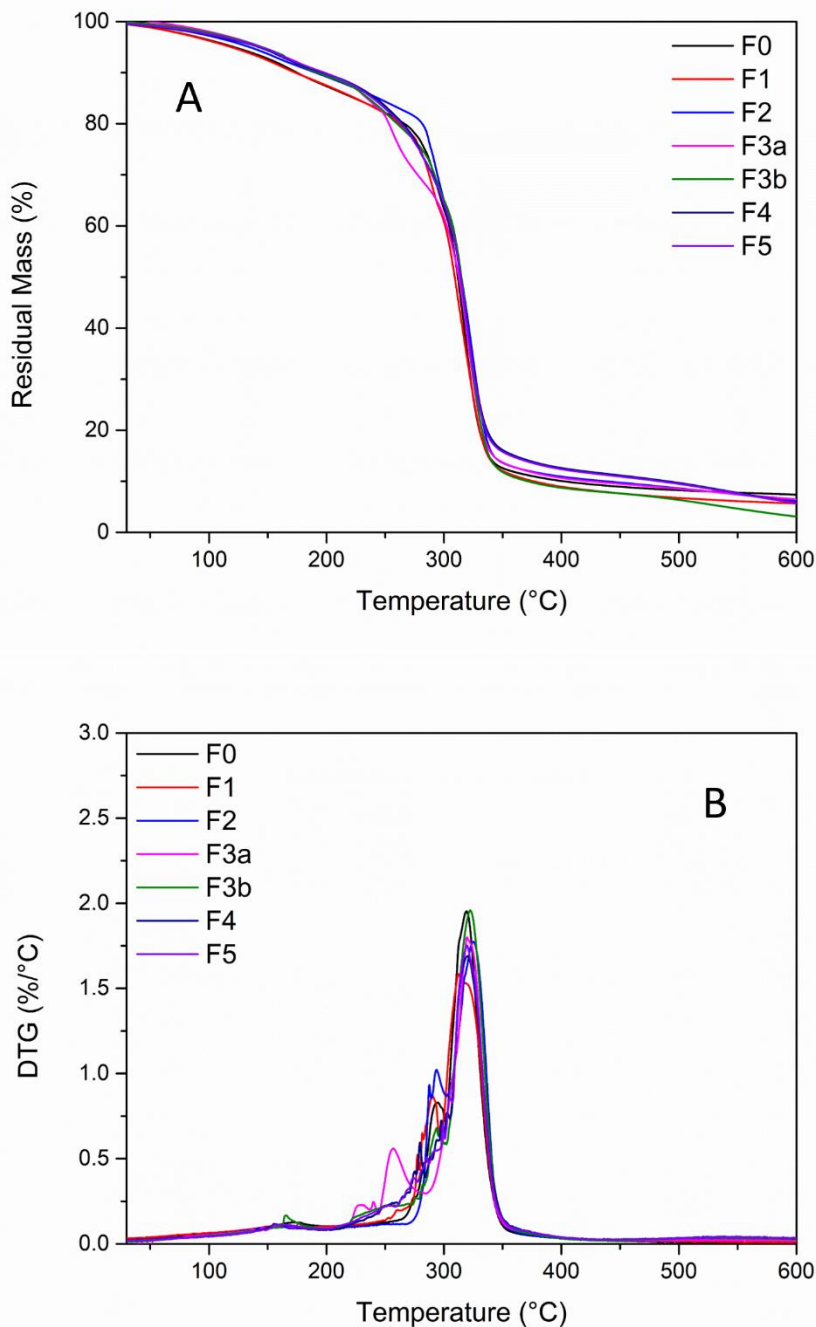


Figure 4.13. TGA profiles of F0, F1, F2, F3a, F3b, F4 and F5.

Swelling capacity

As already highlighted in previous sections (3.3.4.), the swelling test is useful to evaluate the ability of the filament to adsorb wound exudate measured as hydration% (**Figure 4.14A**), allowing it to maintain adequate moisture characteristics for healing. The matrix erosion or DS% of each filament was evaluated as a complementary study after the swelling (**Figure 4.14B**) in order to evaluate also the maintenance or loss of filament

4. TPS filaments optimization suitable for FDM printing

integrity. Both analyses were performed by immersing filament pieces in SWF for predetermined time intervals and then weighed (as indicated in *Section 4.3.2.*).

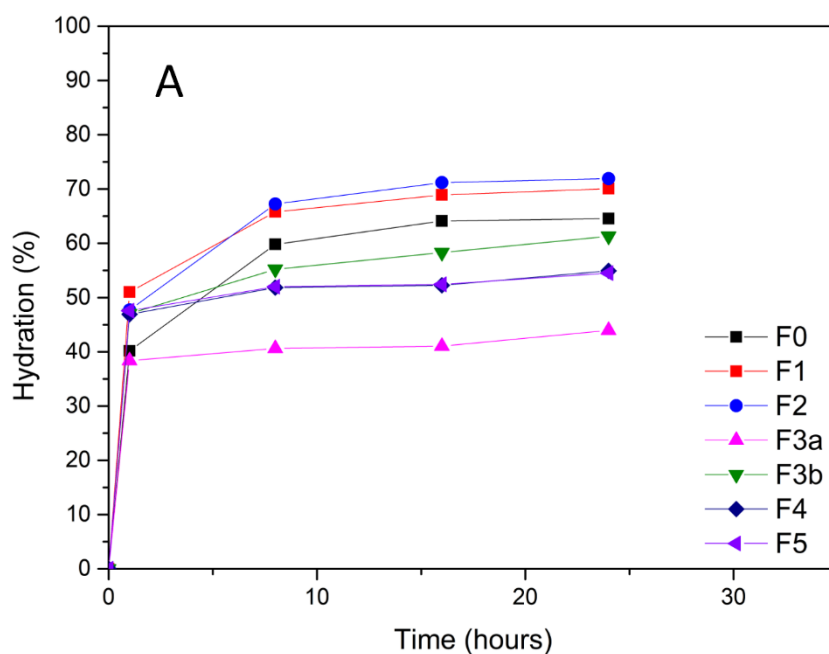
The highest exudate adsorption ($71.98\% \pm 0.90$) was found for F2 sample, followed by F1, F0, F3b, F4-F5 and F3a (**Table 4.5, Figure 4.14A**). All the filaments have the ability to absorb a significant amount of SWF within 24 h. However, some differences can be ascribed to their different composition. F1 and F2 (same profile) showed the highest adsorption capacity due to the presence of HAL and MMT (153,190). It is widely known that clays have an enormous swelling capacity, especially MMT. It is also worth noting that this swelling process is progressive. The swelling capacity of F3a, containing CA, showed the lowest values probably due to CA dissolution in water, triggering the degradation of the filament and so, reducing the SWF adsorption capacity. Similar results were already reported, authors ascribing this effect due to the lower capacity of the biopolymer to bind water molecules in presence of CA (191) or to the reticulation degree (192). Das *et al.* (44) have also reported that CA reduced the swelling but improves the filament dissolution. Moreover, the presence of CA created internal porosity (**Figure 4.7**), jeopardizing their integrity and favouring erosion. Filaments with MgSt tend to reduce the SWF adsorption capacity with respect to F0. This can be explained by the water repellent feature of MgSt, widely reported during the formulation of tablets and capsules (193,194). This property has reported to hinder disintegrants (CS) swelling, which could explain these results.

Regarding DS% (**Figure 4.14B**), there is an indirect correlation between the swelling capacity and matrix erosion. The lowest weight loss was found for F0, F1 and F2, losing a total of 29.17, 27.40 % and 25.87 %, respectively (**Table 4.4**). In particular, F2 maintained a slightly higher integrity, suggesting the benefits of MMT use to obtain a swellable and at the same time stable filaments (minor erosion mechanisms) useful for example to realize implantable scaffolds or patches applied over exudated wounds. F3a is the filament showing the higher fragment lost suggesting its lower integrity in SWF compared to the other filaments. This agrees with our hypothesis about CA dissolution and filament degradation previously mentioned (192). MgSt increases filament degradation respect to their counterparts. We hypothesize that MgSt could hinder the internal polymer network (reticulation degree) thus accelerating filament disintegration.

4. TPS filaments optimization suitable for FDM printing

Table 4.5. Swelling and DS value.

Filament samples	maximum swelling capacity value (\pm SD)	maximum DS value (\pm SD)
F0	64.61 % \pm 0.40	29.17 % \pm 0.01
F1	70.07 % \pm 1.40	27.40 % \pm 0.03
F2	71.98 % \pm 0.90	25.87 % \pm 0.01
F3a	44.68 % \pm 1.00	58.68 % \pm 0.30
F3b	61.55 % \pm 0.30	55.02 % \pm 0.80
F4	55.35 % \pm 0.80	54.95 % \pm 0.60
F5	55.40 % \pm 1.20	55.85 % \pm 0.90



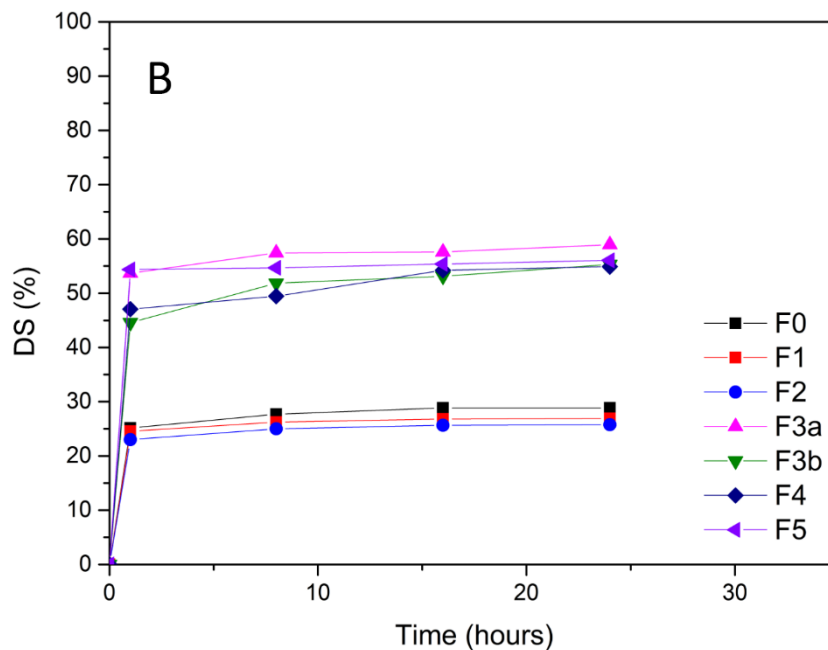


Figure 4.14. Hydration (%) (A) and DS (%) (B) of all filaments (F0-F5). For graph clarity the SD are previously indicated.

4.4.2. Biological properties

Antimicrobial activity

Filaments antimicrobial activity was studied by the agar diffusion method properly modified (166,167), the results gathered in **Table 4.6**. **Figure 4.15** presents captured images of some of the results of the antibacterial assay reported in **Table 4.6**.

As expected, F0 filaments did not show antimicrobial activity, followed by F1 (with HAL) and F2 (filament with MMT).

The most important antimicrobial activity was observed for F3a against *S. pyogenes* (195). The same filament also showed antimicrobial activity against other three Gram+ bacteria, including *C. perfringens*, as previously described in literature for CA (196). In view of F3a composition, it is possible to correlate the CA presence to the antimicrobial activity. In general, CA proved to be more effective against Gram+ bacteria than Gram- bacteria. Unfortunately, no studies were found that showed antimicrobial activity against the same bacteria tested, but literature data confirms the highest antimicrobial activity against Gram+ bacteria (192,195,196). Such antibacterial effectiveness is due to the acidic nature of CA that can break down protein synthesis and cell membrane, thus inhibiting bacteria proliferation (192).

4. TPS filaments optimization suitable for FDM printing

On the other hand, although studies on the antifungal activity of CS are found in literature (197), we did not have good results in any case, which could be due to the high temperatures of the plasticization process for filament production. It could also be related to the absence of CS diffusion throughout the agar, limiting its effect to the bare filament surface.

Table 4.6. Filaments antimicrobial activity.

Strains	F0	F1	F2	F3a	F3b	F4	F5
	diameter (mm)						
Gram +							
<i>E. faecalis</i>	-	-	-	-	-	-	-
<i>S. epidermidis</i>	-	-	-	8.19	-	-	-
<i>B. subtilis</i>	-	-	-	-	-	-	-
<i>S. aureus</i>	-	-	-	-	-	-	-
<i>S. aureus MR</i>	-	-	-	-	-	-	-
<i>S. pyogenes</i>	-	-	-	13.35	10.30	10.23	10.23
<i>B. cereus</i>	-	-	-	-	7.12	-	7.01
<i>C. perfringens</i>	-	-	-	8.97	-	-	-
<i>P. acnes</i>	-	-	-	10.31	-	-	-
Gram -							
<i>P. aeruginosa</i>	-	-	-	-	-	-	-
<i>K. pneumoniae</i>	-	-	-	-	-	-	-
<i>P. mirabilis</i>	-	-	-	8.17	7.60	7.22	7.31
<i>E. coli</i>	-	-	-	-	-	-	-
<i>E. cloacae</i>	-	-	-	-	-	-	-
Yeast							
<i>C. albicans</i>	-	-	-	-	-	-	-

∴ no halo observed

4. TPS filaments optimization suitable for FDM printing

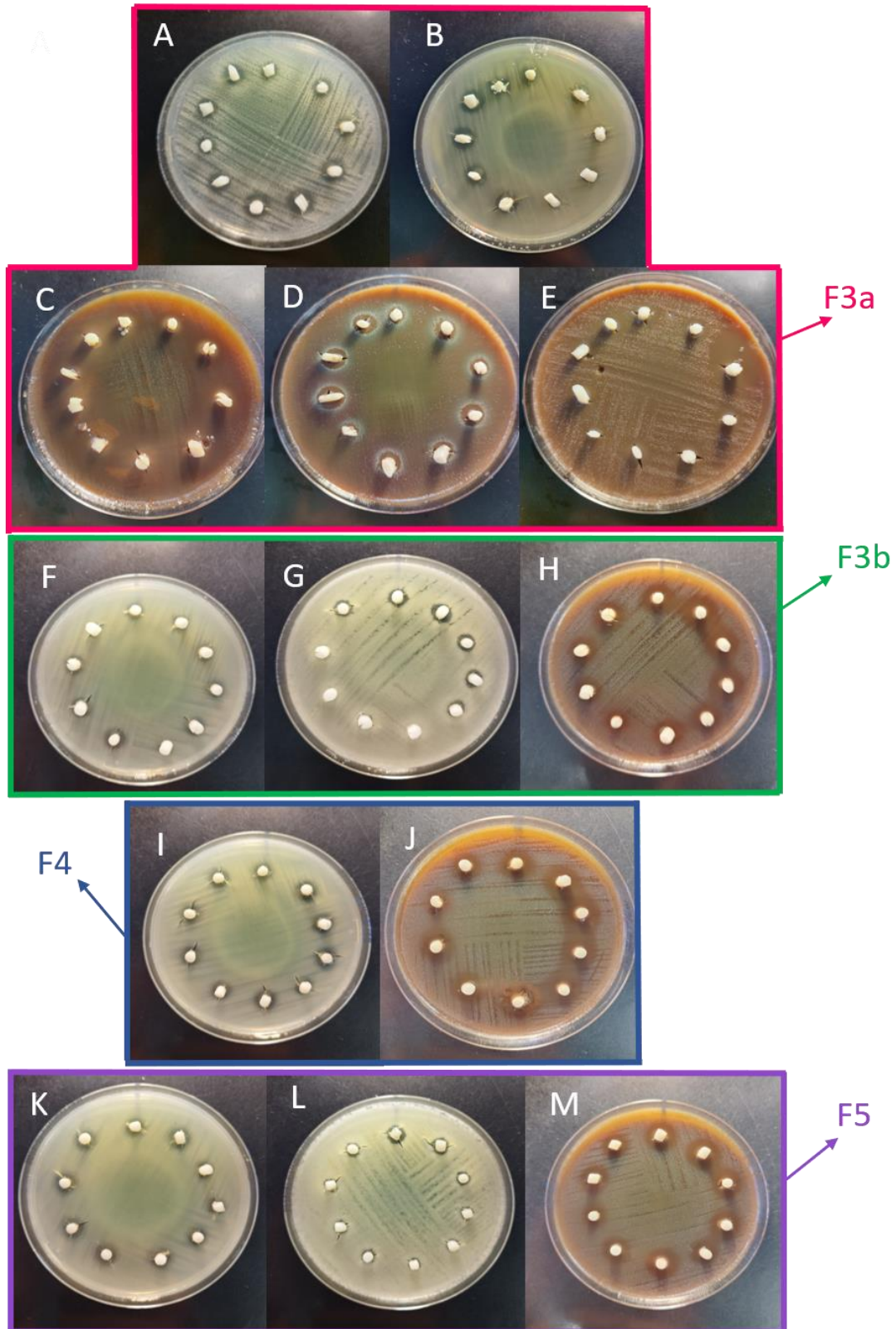


Figure 4.15. Inhibition halos for F3a (A) *S. epidermis* (B) *P. mirabilis* (C) *S. pyogenes* (D) *C. perfringens* (E) *P. acnes*; for F3b (F) *P. mirabilis* (G) *B. cereus* (H) *C. pyogenes*; for F4 (I) *P. mirabilis* (J) *S. pyogenes*; for F5 (K) *P. mirabilis* (L) *B. cereus* (M) *S. pyogenes*. 10 samples of the same filament were tested on each dish.

4. TPS filaments optimization suitable for FDM printing

4.4.3. Prototypes patches preparation

4.4.3.1. Selection of printing parameters and digital design

Circular patches designed (2 cm diameter) were printed with a $+45^{\circ}/-45^{\circ}$ orientation in order to obtain adequate mechanical properties and reduce syringe sudden changes of direction. Through empirical and literature-based results (198), the following printing parameters were optimized.

Nozzle diameter

Nozzle diameter influences some of the above mentioned properties (print resolution, interlayer adhesion). Nozzle diameter evaluated corresponded to standardized nozzle gauges of 24, 22 and 20. A 0.6 mm (22-gauge) nozzle was selected as it gave good results. However, using a 0.4 mm (24 gauge) nozzle, filament occluded the nozzle output, and using a 0.8 mm (20-gauge) nozzle, the melted filament was too thick to accurately print the suitable patch.

Printing temperature, build plate temperature

Printing and build plate temperature are considered critical parameters during printing process. Patch printed is compromised by temperature variations, leading to structural delamination and reducing mechanical strength (199). Printing temperature was optimized at 210°C and build plate temperature at 80°C , based on empirical results. Build plate temperature allowed an adequate adhesion of the patch to the surface of the plate, allowing uniform printing until a complete patch.

Top/bottom layer thickness

Top/bottom layer was selected at 0.3 mm. In general, more layers will result in a smoother patch surface.

Fan speed

It is an important parameter which influences the quality of the printed patches. It was optimized to 30% based on observed results.

Print speed

4. TPS filaments optimization suitable for FDM printing

It was optimized at 60 mm/s, as better results were obtained at higher print speed than at lower ones. It was possible to print patch prototypes in short printing times, thus allowing filament could be printed without degradation during printing process.

After optimizing the 3D printing parameters, prototype patches were fabricated using F3b and F4 filaments. The most suitable patches, with a more uniform and less brittle outcome, were obtained using the 3D printing parameters shown in **Table 4.7**.

Table 4.7. Setting parameters for FDM technique used F3b and F4 filaments.

Parameters	Values	Units
Nozzle diameter	0.6	mm
Printing temperature	210	°C
Build plate temperature	80	°C
Layer height	0.3	mm
Top/bottom layer thickness	0.3	mm
Flow rate	97	%
Fan speed	30	%
Print speed	60	mm/s
Infill density	100	%

By utilizing the F3b and F4 filaments, we were able to obtain some prototypes of patches using the FDM technique. These filaments were the most suitable for FDM 3D printing, as they contained different additives that enhanced their mechanical and thermal properties. It should be noted that the F4 filament showed greater thermal stability and less moisture absorption during the printing process than the F3b filament. This allowed to obtain a prototype patch (Patch B) that resulted more homogeneous than patch A. However, despite the results obtained, the humidity problem did not allow stable printing for the remaining filaments. This humidity affected the filament diameter, and in turn, these variations hindered filament printing process.

Visually, printed prototypes patches showed good uniformity. Fresh patches were observed, and both showed stiffness. Then, at R.T. during 24 h (storage conditions), patch A (**Figure 4.16**), obtained from F3b, still showed stiffness. However, patch B (**Figure 4.16**), obtained from F4, was more flexible after same conditions (24 h at R.T.), this could be due to the moisture absorbed by the patch. Patch B could be more suitable than patch A for application to the skin because of its adaptability. Further research will continue with these filaments and with F5, in order to overcome the problems found and to achieve suitable patches that adapt to the skin and have the ideal properties for a wound skin.

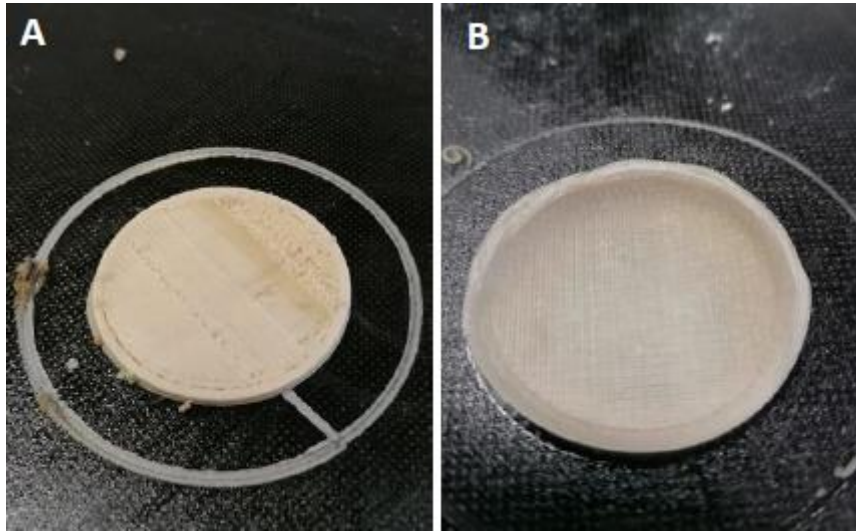


Figure 4.16. Patches prototypes by FDM technique.

5. CONCLUSIONS

The research activity performed during the PhD thesis was focused on the development of biosustainable CS-based patches for the wound treatment. For this purpose, appropriate formulations were produced by 3D printing using the extrusion-based 3D printing techniques pressure-assisted microsyringe (PAM) and fused deposition modeling (FDM).

Pressure Assisted Microsyringe (PAM) 3D Printing.

In this first study, two hydrogels (G4- β glu and NaHy-H2) were developed and optimized. They were based on ingredients useful for 3D printing processing such as corn starch, glycerol (Gly) and a water suspension of β glucan (β glu) as filler. In the second hydrogel, sodium hyaluronate (NaHy) was added to the formulation (NaHy-H2) in order to improve biological properties of the patch. Both hydrogels showed rheological properties suitable for PAM technique use. In addition the thorough study of each printing parameter was necessary in order to plan both an adequate 3D printing process and suitable wound dressing. Once these wound dressings were manufactured, the best drying conditions were evaluated (24 h at 37°C). In addition, the patches were reinforced with an Alg-based backing to achieve better structural properties. Finally, the obtained patches were characterized for both physicochemical and biological properties. The Alg_NaHy patch showed better properties in terms of compactness, tensile strength, elasticity, bio adhesiveness, ease of handling, and ease of application and removal than the patch without NaHy (Alg_ β glu). β glu soluble fraction released from the patch demonstrated to be able to stimulate keratinocytes growth and thus useful for wound healing Thus, the objectives of this study were achieved.

Future research will focus on increasing the NaHy concentration and/or changing active ingredient to obtain adequate antimicrobial activity and wound closure. Nevertheless, this study achieved the development biosustainable of formulations with minimum risk to the environment by using eco-friendly raw materials and production methods (PAM technique). In addition, this study has the potential to revolutionize the traditional wound dressing, as traditional wound dressings are often made of synthetic materials, increasing pollution. Finally, this study may have an impact on the patient's quality of life, as the developed patches can be easily applied (without the need of specialized personnel) and removed without pain.

TPS filaments optimization suitable for FDM 3D printing.

In the second part of the study, TPS filaments useful for FDM 3D printing were developed using corn starch and glycerol, as main components, combined to montmorillonite (MMT), citric acid (CA), and magnesium stearate (MgSt). In addition, methyl sulfonyl methane (MSM) was chosen as model drug to be incorporated in the TPS filament. These filaments were characterized in terms of their physicochemical and biological properties. The addition of MMT was the most suitable filler for the development of these filaments, as well as, the F2 filament (containing MMT) showed good results in terms of thermal properties, as it suffered less mass loss in key temperature zones during the 3D printing process. F3a (containing CA) showed more promising results than the rest of the filaments, in terms of its potential as antimicrobial, however, it was discarded as a printing filament due to its poor stability during the 3D printing process. Also, key printing parameters were optimized in order to manufacture prototype patches using FDM technique. Patches A and B were developed from the F3b and F4 filaments. It can be assumed that the F4 filament is the most promising combination for the development of prototype patches. This filament showed higher thermal stability properties during the printing process than the F3b filament. In addition, the F4 filament showed less change in diameter at the time of printing (capturing less moisture from the environment), allowing a more stable print, and obtaining a more homogeneous prototype patch than with the F3b filament. Patch B could be used as a wound dressing, although future studies will be necessary. It is possible to conclude that the planned objectives have been achieved. Future research will focus on the characterization of these patches and will continue with the production of patches from the F5 filament until the patch that possess the desired characteristics for wound treatment. Nonetheless, this study has succeeded in overcoming the development of biosustainable TPS filaments for use in 3D printing. Taking into account that filaments available on the market contain synthetic polymers, the filaments developed in this thesis have the potential to revolutionize the pharmaceutical sector, since they are filaments based on natural ingredients and have proven to be useful in printing dressings.

In addition to these specific considerations on the products obtained, other general conclusions can also be made regarding the contribution of this entire study. It is in fact important to underline that both PAM and FDM 3D printing technology is an innovative and useful tool in the field of personalized medicine, allowing the on-demand production

of dressings to meet the needs of each patient. Thanks to CAD design it is possible to prepare customizable patches having an effective response, achieving greater patient adherence, since it adapts to the characteristics of the patient's wound. Furthermore, the development of these dressings could help to improve the patient's quality of life, reducing pain and damage of newly formed tissues during their removal from wounds. The ease of application and removal of these patches on wounds makes them very easy to handle and self-manage. This allows the home treatment of even chronic wounds without the aid of specific personnel. It is therefore clear that this aspect also contributes to improving the patient's quality of life.

The formulations studied were produced using simple, cheap, safe and biodegradable materials from natural, renewable and biosustainable sources. Unlike the classic formulations mainly present on the market today, no synthetic products were used and all processing involves low energy consumption procedures and avoids the use of organic solvents and toxic materials. Since 3D printing is an additive and not subtractive technique, the patch production process does not produce production waste. All this minimizes pollution and allows industrial production that respects the environment and integrates industries and environment with the awareness that the human health is not separable from that of the environment and the animals, according to one health concept.

5.1. Conclusiones

El estudio de investigación realizado durante esta tesis doctoral se centró en el desarrollo de parches biosostenibles a base de almidón de maíz (CS) para el tratamiento de heridas. Para ello, se desarrollaron formulaciones adecuadas para ser procesadas mediante las técnicas de impresión 3D basadas en extrusión: microjeringa asistida por presión (PAM) y modelado por deposición fundida (FDM).

Impresión 3D con microjeringa asistida por presión (PAM).

En este primer estudio, se desarrollaron y optimizaron dos hidrogeles (G4- β glu y NaHy-H2). Se basaron en ingredientes útiles para el procesamiento de impresión 3D, como almidón de maíz, glicerol (Gly) y una suspensión acuosa de β glucano (β glu) como relleno. En el segundo hidrogel, se añadió hialuronato sódico (NaHy) a la formulación (NaHy-H2) para mejorar las propiedades biológicas del parche. Ambos hidrogeles mostraron propiedades reológicas adecuadas para su uso en la técnica PAM. Además, fue necesario estudiar minuciosamente cada parámetro de impresión para optimizar tanto el proceso de impresión 3D, como para desarrollar un apósito apropiado para heridas. Una vez fabricados estos apósitos para heridas, se evaluaron las condiciones óptimas de secado (24 h a 37°C). Además, los parches se reforzaron con un soporte a base de alginato de sodio (Alg) para mejorar sus propiedades estructurales. Por último, los parches obtenidos se caracterizaron en cuanto a sus propiedades fisicoquímicas y biológicas. El parche Alg_NaHy mostró mejores propiedades en cuanto a compacidad, resistencia a la tracción, elasticidad, bioadhesividad, facilidad de manipulación y facilidad de aplicación y retirada que el parche sin NaHy (Alg_ β glu). La fracción soluble de β glu liberada del parche demostró ser capaz de estimular el crecimiento de los queratinocitos y, por tanto, útil para la cicatrización de heridas. Así pues, se alcanzaron los objetivos de este estudio.

Los futuros estudios se centrarán en aumentar la concentración de NaHy y/o cambiar el ingrediente activo para obtener una actividad antimicrobiana y un cierre de heridas adecuados. No obstante, este estudio logró el desarrollo de formulaciones biosostenible, con el mínimo riesgo hacia el medio ambiente, mediante el uso de materias primas y métodos de producción ecológicos (técnica PAM). Además, este estudio tiene el potencial de revolucionar los apósitos tradicionales para heridas, ya que éstos suelen estar fabricados con materiales sintéticos, lo que aumenta la contaminación. Por último, este estudio puede repercutir en la calidad de vida del paciente, ya que los parches desarrollados pueden aplicarse fácilmente (sin necesidad de personal especializado) y

retirarse sin dolor.

Optimización de filamentos TPS adecuados para la impresión 3D FDM.

En la segunda parte del estudio, se desarrollaron filamentos de TPS útiles para la impresión 3D FDM a base de CS y Gly, como componentes principales, combinados con montmorillonita (MMT), ácido cítrico (CA) y estearato de magnesio (MgSt). Además, se eligió el metil sulfonil metano (MSM) como fármaco modelo para incorporarlo al filamento final de TPS. Estos filamentos se caracterizaron en cuanto a sus propiedades fisicoquímicas y biológicas. Se comprobó que la adición de MMT fue el relleno más adecuado para el desarrollo de estos filamentos. El filamento F2 (que contiene MMT), mostró mejores resultados en términos de propiedades térmicas, ya que sufría menos pérdida de masa en zonas clave de temperatura durante el proceso de impresión 3D que el resto de los filamentos. Por otro lado, el filamento F3a (que contiene CA) mostró resultados más prometedores en cuanto a su potencial antimicrobiano, pero fue descartado como filamento de impresión por su poca estabilidad durante el proceso de impresión 3D. Finalmente, los filamentos F3b y F4 fueron los más estables para ser utilizados con FDM. Además, se optimizaron los parámetros clave de impresión para fabricar prototipos de parches mediante la técnica FDM. Los parches A y B se desarrollaron a partir de los filamentos más estables para impresión (F3b y F4). Cabe suponer que el filamento F4 es la combinación más prometedora para el desarrollo de prototipos de parches. Este filamento mostró unas propiedades de estabilidad térmica durante el proceso de impresión superiores a las del filamento F3b. Además, el filamento F4 mostró un menor cambio de diámetro en el momento de impresión (captando menos humedad del ambiente), permitiendo una impresión más estable, y obteniendo un prototipo de parche más homogéneo que con el filamento F3b. El parche B podría utilizarse como apósito para heridas, aunque serán necesarios futuros estudios. Se puede concluir que se han alcanzado los objetivos previstos. La investigación futura se centrará en la caracterización de estos parches y se continuará con la producción de parches a partir del filamento F5 hasta conseguir el parche que posea las características deseadas para el tratamiento de heridas. No obstante, este estudio ha logrado superar el desarrollo de filamentos de TPS biosostenibles para su uso en impresión 3D. Teniendo en cuenta que los filamentos disponibles en el mercado contienen polímeros sintéticos, los filamentos desarrollados en esta tesis tienen el potencial de revolucionar el sector farmacéutico, ya que son filamentos basados en ingredientes naturales y han demostrado su utilidad en la impresión de

apósitos.

Además de estas consideraciones específicas sobre los productos obtenidos, también pueden extraerse otras conclusiones generales sobre la contribución de este estudio. De hecho, es importante subrayar que tanto la tecnología PAM como la FDM constituyen una herramienta innovadora y útil en el campo de la medicina personalizada, permitiendo la producción bajo demanda de apósitos que se ajusten a las necesidades de cada paciente. Gracias al diseño CAD es posible elaborar parches personalizables con una respuesta eficaz, y que conseguirían una mayor adherencia del paciente, ya que se adaptan a las características de la herida de cada paciente. Además, el desarrollo de estos apósitos podría ayudar a mejorar la calidad de vida del paciente, reduciendo el dolor y el daño de los tejidos recién formados durante su retirada de las heridas. La facilidad de aplicación y retirada de estos parches sobre las heridas hace que sean muy fáciles de manipular y autogestionar. Esto permitiría el tratamiento domiciliario incluso de heridas crónicas sin la ayuda del personal cualificado. Por lo tanto, es evidente que este aspecto también contribuiría a mejorar la calidad de vida del paciente.

Las formulaciones estudiadas se produjeron utilizando materiales sencillos, económicos, seguros y biodegradables procedentes de fuentes naturales, renovables y biosostenibles. A diferencia de la mayoría de las formulaciones tradicionales presentes en el mercado actual, no se utilizaron productos sintéticos y todo el proceso de elaboración implica procedimientos de bajo consumo energético y evita el uso de disolventes orgánicos y materiales tóxicos. Dado que la impresión 3D es una técnica aditiva y no sustractiva, el proceso de producción de los parches no genera residuos de producción. Todo ello minimiza la contaminación y permite una producción industrial respetuosa con el medio ambiente e integra industrias y medio ambiente con la conciencia de que la salud humana no es separable de la del medio ambiente y los animales, de acuerdo con “un mismo concepto de salud”.

References

1. Boateng JS, Matthews KH, *et al.* Wound Healing Dressings and Drug Delivery Systems: A Review. *J Pharm Sci.* **2008**, 97(8):2892–2923.
2. International Genetically Engineered Machine (iGEM) 2022. <https://2022.igem.wiki/aalto-helsinki/description>. Accessed on December 19, **2022**.
3. Morton LM, Phillips TJ. Wound healing and treating wounds: Differential diagnosis and evaluation of chronic wounds. *J Am Acad Dermatol.* **2016**, 74(4):589–605.
4. Serra R, Grande R, *et al.* Chronic wound infections: the role of *Pseudomonas aeruginosa* and *Staphylococcus aureus*. *Expert Rev Anti Infect Ther.* **2015**, 13(5):605–613.
5. Rosenbaum AJ, Banerjee S, *et al.* Advances in wound management. *JAAOS.* Lippincott Williams and Wilkins; **2018**, 26(23):833–843.
6. Ghatak S, Maytin EV, *et al.* Roles of Proteoglycans and Glycosaminoglycans in Wound Healing and Fibrosis. *Int J Cell Biol.* **2015**, 2015: 834-893.
7. Koehler J, Brandl FP, *et al.* Hydrogel wound dressings for bioactive treatment of acute and chronic wounds. *Eur Polym J.* **2018**, 100: 1-11.
8. Wilkinson HN, Hardman MJ. Wound healing: cellular mechanisms and pathological outcomes. *Open Biol.* **2020**, 10(9):200-223.
9. Da Silva LP, Reis RL, *et al.* Hydrogel-Based Strategies to Advance Therapies for Chronic Skin Wounds. *Annu Rev Biomed Eng.* **2019**, 21:145–169.
10. Long L, Liu W, *et al.* Construction of multifunctional wound dressings with their application in chronic wound treatment. *Biomater Sci.* **2022**, 10(15):4058–4076.
11. Menke NB, Ward KR, *et al.* Impaired wound healing. *Clin Dermatol.* **2007**, 25(1):19–25.
12. Schultz GS, Sibbald RG, *et al.* Wound bed preparation: a systematic approach to wound management. *Wound Repair Regen.* **2003**, 11(1): 1-28.
13. Siddiqui AR, Bernstein JM. Chronic wound infection: facts and controversies. *Clin Dermatol.* **2010**, 28(5):519–526.
14. Howell-Jones RS, Wilson MJ, *et al.* A review of the microbiology, antibiotic usage and resistance in chronic skin wounds. *J Antimicrob Chemother.* **2005**, 55(2):143–149.
15. Yao G, Mo X, *et al.* A programmable and skin temperature-activated electromechanical synergistic dressing for effective wound healing. *Sci Adv.* **2022**, 8(4): eabl8379.

16. Järbrink K, Ni G, *et al.* Prevalence and incidence of chronic wounds and related complications: a protocol for a systematic review. *Syst Rev.* **2016**, 5:e152.
17. Kapp S, Santamaria N. The financial and quality-of-life cost to patients living with a chronic wound in the community. *Int Wound J.* **2017**, 14(6):1108–1119.
18. Lindholm C, Searle R. Wound management for the 21st century: combining effectiveness and efficiency. *Int Wound J.* **2016**, 13(2):5–15.
19. Nussbaum SR, Carter MJ, *et al.* An Economic Evaluation of the Impact, Cost, and Medicare Policy Implications of Chronic Nonhealing Wounds. *Value in Health.* **2018**, 21(1):27–32.
20. Guest JF, Greener MJ, *et al.* Clinical and economic evidence supporting a transparent barrier film dressing in incontinence-associated dermatitis and periwound skin protection. *J Wound Care.* **2011**, 20(2):76–84.
21. Palo M, Rönkönharju S, *et al.* Bi-Layered polymer carriers with surface modification by electrospinning for potential wound care applications. *Pharmaceutics* **2019**, 11(12):e678.
22. Broussard KC, Powers JG. Wound dressings: selecting the most appropriate type. *Am J Clin Dermatol.* **2013**, 14(6):449–459.
23. Jones V, Grey JE, Harding KG. Wound dressings. *BMJ.* **2006**, 332(7544):777–780.
24. Hwang I, Kim HN, *et al.* Multifunctional Smart Skin Adhesive Patches for Advanced Health Care. *Adv. Health Mater.* **2018**, 7(15):e1800275.
25. Alven S, Nqoro X, *et al.* Polymer-based materials loaded with curcumin for wound healing applications. *Polymers.* **2020**, 12(10):1–25.
26. García-Villén F, Souza IMS, *et al.* Natural Inorganic Ingredients in Wound Healing. *Curr Pharm Des* **2020**, 26(6):621–641.
27. Viseras C, Aguzzi C, *et al.* Uses of clay minerals in semisolid health care and therapeutic products. *Appl Clay Sci.* **2007**, 36(1–3):37–50.
28. Choy J ho, Park M. Cationic and anionic clays for biological applications. *Interface Sci Technol* **2004**, 1:403–424.
29. Ghadiri M, Chrzanowski W, *et al.* Biomedical applications of cationic clay minerals. *RSC Adv.* **2015**, 5(37): 29467-29481.
30. Alemdar A, Güngör N, *et al.* The rheological properties and characterization of bentonite dispersions in the presence of non-ionic polymer PEG. *J Mater Sci.* **2005**, 40(1):171–177.
31. Clem AG, Doehler RW. Industrial Applications of Bentonite. *Clays and Clay Minerals.* **1961**, 10(1):272–283.

32. Viseras C, Meeten GH, *et al.* Pharmaceutical grade phyllosilicate dispersions: the influence of shear history on floc structure. *Int J Pharm.* **1999**, 182(1):7–20.
33. Alekseeva O V., Rodionova AN, *et al.* Effect of the bentonite filler on structure and properties of composites based on hydroxyethyl cellulose. *Arab J Chem.* **2019**, 12(3):398–404.
34. Devi N, Dutta J. Preparation and characterization of chitosan-bentonite nanocomposite films for wound healing application. *Int J Biol Macromol.* **2017**, 104:1897–1904.
35. Peñaloza DJrP. Review on the Preparation, Structure and Property Relation of Clay-Based Polymer Nanocomposites. *KIMIKA.* **2017**, 28(1):44–56.
36. Manson J, Dixon D. The influence of solvent processing on polyester bioabsorbable polymers. *J Biomater Appl.* **2012**, 26(5):623–634.
37. Huang ZM, Zhang YZ, *et al.* A review on polymer nanofibers by electrospinning and their applications in nanocomposites. *Compos Sci Technol.* **2003**, 63(15):2223–2253.
38. Bhardwaj N, Kundu SC. Electrospinning: a fascinating fiber fabrication technique. *Biotechnol Adv.* **2010**, 28(3):325–347.
39. Mohammed AA, Algahtani MS, *et al.* Optimization of semisolid extrusion (pressure-assisted microsyringe)-based 3D printing process for advanced drug delivery application. *Ann 3D Print Med.* **2021**, 2:e100008.
40. Buanz ABM, Belaunde CC, *et al.* Ink-jet printing versus solvent casting to prepare oral films: Effect on mechanical properties and physical stability. *Int J Pharm.* **2015**, 494(2):611–618.
41. Teo WE, Ramakrishna S. A review on electrospinning design and nanofibre assemblies. *Nanotechnology.* **2006**, 17(14): 89-106.
42. Zahedi P, Rezaeian I, *et al.* A review on wound dressings with an emphasis on electrospun nanofibrous polymeric bandages. *Polym Adv Technol.* **2010**, 21(2):77–95.
43. Rodríguez-Tobías H, Morales G, *et al.* Comprehensive review on electrospinning techniques as versatile approaches toward antimicrobial biopolymeric composite fibers. *Mater Sci Eng C Mater Biol Appl.* **2019**, 101:306–322.
44. Electrospinning Technique. <https://www.weistron.com/electrospinning-tech/>. Accessed on June 15, **2021**.
45. Yu C, Schimelman J, *et al.* Photopolymerizable Biomaterials and Light-Based 3D Printing Strategies for Biomedical Applications. *Chem Rev.* **2020**, 120(19):10695–10743.

46. Park BJ, Choi HJ, *et al.* Pharmaceutical applications of 3D printing technology: current understanding and future perspectives. *J Pharm Investig.* **2019**, 49(6):575–585.
47. Teoh JH, Tay SM, *et al.* Fabricating scalable, personalized wound dressings with customizable drug loadings via 3D printing. *J Control Release.* **2022**, 341:80–94.
48. Aguilar-De-leyva Á, Linares V, *et al.* 3D Printed Drug Delivery Systems Based on Natural Products. *Pharmaceutics.* **2020**, 12(7):1–20.
49. Govender R, Kissi EO, *et al.* Polymers in pharmaceutical additive manufacturing: A balancing act between printability and product performance. *Adv Drug Deliv Rev.* **2021**, 177:e113923.
50. Beg S, Almalki WH, *et al.* 3D printing for drug delivery and biomedical applications. *Drug Discov Today.* **2020**, 25(9):1668-1681.
51. Norman J, Madurawe RD, *et al.* A new chapter in pharmaceutical manufacturing: 3D-printed drug products. *Adv Drug Deliv Rev.* **2017**, 108:39–50.
52. Azad MA, Olawuni D, *et al.* Polymers for Extrusion-Based 3D Printing of Pharmaceuticals: A Holistic Materials-Process Perspective. *Pharmaceutics.* **2020**, 12(2):e124.
53. Vaz VM, Kumar L. 3D Printing as a Promising Tool in Personalized Medicine. *AAPS PharmSciTech.* **2021**, 22(1):e49.
54. Varghese R, Sood P, *et al.* 3D printing in the pharmaceutical sector: Advances and evidences. *Sens Int.* **2022**, 3:e100177.
55. Zidan A, Alayoubi A, *et al.* Extrudability analysis of drug loaded pastes for 3D printing of modified release tablets. *Int J Pharm.* **2019**, 554:292–301.
56. Seoane-Viaño I, Januskaite P, *et al.* Semi-solid extrusion 3D printing in drug delivery and biomedicine: Personalised solutions for healthcare challenges. *J Control Release.* **2021**, 332:367–89.
57. Vithani K, Goyanes A, *et al.* An Overview of 3D Printing Technologies for Soft Materials and Potential Opportunities for Lipid-based Drug Delivery Systems *Pharm Res.* **2019**, 36(1):1–20.
58. Khaled SA, Burley JC, *et al.* Desktop 3D printing of controlled release pharmaceutical bilayer tablets. *Int J Pharm.* **2014**, 461(1–2):105–111.
59. Khaled SA, Burley JC, *et al.* 3D printing of five-in-one dose combination polypill with defined immediate and sustained release profiles. *J Control Release.* **2015**, 217:308–314.
60. Conceição J, Farto-Vaamonde X, *et al.* Hydroxypropyl- β -cyclodextrin-based fast dissolving carbamazepine printlets prepared by semisolid extrusion 3D printing. *Carbohydr Polym.* **2019**, 221:55–62.

61. Kristiawan RB, Imaduddin F, *et al.* A review on the fused deposition modeling (FDM) 3D printing: Filament processing, materials, and printing parameters. *Open Eng.* **2021**, 11(1):639–649.
62. Valino AD, Dizon JRC, *et al.* Advances in 3D printing of thermoplastic polymer composites and nanocomposites. *Prog Polym Sci.* **2019**, 98:e101162.
63. Cano-Vicent A, Tambuwala MM, *et al.* Fused deposition modelling: Current status, methodology, applications and future prospects. *Addit Manuf.* **2021**, 47:2214–8604.
64. Patil H, Tiwari RV, *et al.* Hot-Melt Extrusion: from Theory to Application in Pharmaceutical Formulation. *AAPS PharmSciTech.* **2016**, 17(1):20–42.
65. Melocchi A, Parietti F, *et al.* 3D printing by fused deposition modeling (FDM) of a swellable/erodible capsular device for oral pulsatile release of drugs. *J Drug Deliv Sci Technol.* **2015**, 30:360–367.
66. Arafat B, Wojsz M, *et al.* Tablet fragmentation without a disintegrant: A novel design approach for accelerating disintegration and drug release from 3D printed cellulosic tablets. *Eur J Pharm Sci.* **2018**, 118:191–199.
67. Huanbutta K, Sangnim T. Design and development of zero-order drug release gastroretentive floating tablets fabricated by 3D printing technology. *J Drug Deliv Sci Technol.* **2019**, 52:831–837.
68. Zamboulis A, Michailidou G, *et al.* Polysaccharide 3D Printing for Drug Delivery Applications. *Pharmaceutics*, **2022**, 14(1):e145.
69. Khan FA, Narasimhan K, *et al.* 3D Printing Technology in Customized Drug Delivery System: Current State of the Art, Prospective and the Challenges. *Curr Pharm Des.* **2018**, 24(42):5049-5061.
70. El Aita I, Breitzkreutz J, *et al.* On-demand manufacturing of immediate release levetiracetam tablets using pressure-assisted microsyringe printing. *Eur J Pharm Biopharm.* **2019**, 134:29–36.
71. Lamichhane S, Bashyal S, *et al.* Complex formulations, simple techniques: Can 3D printing technology be the Midas touch in pharmaceutical industry? *Asian J Pharm Sci.* **2019**, 14(5):465-479.
72. Zema L, Melocchi A, *et al.* Three-Dimensional Printing of Medicinal Products and the Challenge of Personalized Therapy. *J Pharm Sci.* **2017**, 106(7):1697–1705.
73. Scoutaris N, Ross SA, *et al.* 3D Printed “Starmix” Drug Loaded Dosage Forms for Paediatric Applications. *Pharm Res.* **2018**, 35(2):e34.
74. PAT minimises regulatory concerns around 3D-printed medicines | DMA Europa. <https://news.dmaeuropa.com/press-releases/pat-minimises-regulatory-concerns-around-3d-printed-medicines/>. Accessed on January 5, **2021**.

75. Conformity assessment procedures for 3D printing and 3D printed products to be used in a medical context for COVID-19. European Commission. <https://ec.europa.eu/growth/single-market/ce-marking/>. Accessed on March 31, **2020**.
76. CDRH. Technical Considerations for Additive Manufactured Medical Devices Guidance for Industry and Food and Drug Administration Staff. <https://www.fda.gov/regulatory-information/search-fda-guidance-documents/technical-considerations-additive-manufactured-medical-devices>. Accessed on December 9, **2023**.
77. Gioumouxouzis CI, Karavasili C, *et al*. Recent advances in pharmaceutical dosage forms and devices using additive manufacturing technologies. *Drug Discov Today*. **2019**, 24(2):636–643.
78. Weaver E, O’Hagan C, *et al*. The sustainability of emerging technologies for use in pharmaceutical manufacturing. *Expert Opin Drug Deliv*. **2022**, 19(7):861–872.
79. Woodson TS. 3D printing for sustainable industrial transformation. *Development*. **2015**, 58(4):571–576.
80. Liu Z, Jiang Q, *et al*. Sustainability of 3D printing: A critical review and recommendations. ASME 2016 11th International Manufacturing Science and Engineering Conference, June 27-July 1. MSEC **2016**, 2. <https://asmedigitalcollection.asme.org/MSEC/proceedings-abstract/MSEC2016/49903/V002T05A004/269054>. Accessed on February 24, **2021**.
81. Tyagi N, Bhardwaj V, *et al*. 3D Printing Technology in the Pharmaceutical and Biomedical Applications: A Critical Review. *Biomed Mater & Dev*. **2023**, 1:3
82. Rett JP, Traore YL, *et al*. Sustainable Materials for Fused Deposition Modeling 3D Printing Applications. *Adv Eng Mater*. **2021**, 23(7):e2001472.
83. Liu J, Sun L, *et al*. Current advances and future perspectives of 3D printing natural-derived biopolymers. *Carbohydr Polym*. **2019**, 207:297–316.
84. 3D-printed medical devices. Report on promising KETs-based products nr. 6. <https://monitor-industrial-ecosystems.ec.europa.eu/reports/other-reports/3d-printed-medical-devices-report-promising-kets-based-product-nr-6>. August 2017. Accessed on April 17, **2021**.
85. 3D Printed Medical Devices Market Size & Share (2023 to 2033) | FMI. <https://www.futuremarketinsights.com/reports/3d-printed-medical-devices-market>. Accessed on January 11, **2023**.
86. Garcia MAVT, Garcia CF, *et al*. Pharmaceutical and Biomedical Applications of Native and Modified Starch: A Review. *Starch/Staerke*. **2020**, 72:7–8.

87. Torres FG, Commeaux S, *et al.* Starch-based biomaterials for wound-dressing applications. *Starch/Staerke*. **2013**, 65(7–8):543–551.
88. Visakh PM, Aji P Mathew, *et al.* Starch-Based bionanocomposites: processing and properties. *Polysaccharide Building Blocks: A Sustainable Approach to the Development of Renewable Biomaterials*, First Edition, edited by Wiley. **2012**, 11:289-308.
89. Alcázar-Alay SC, Meireles MAA. Physicochemical properties, modifications and applications of starches from different botanical sources. *Food Sci Technol Int*. **2015**, 35(2):215–236.
90. Bangar SP, Purewal SS, *et al.* Functionality and Applicability of Starch-Based Films: An Eco-Friendly Approach. *Foods*. **2021**, 10(9):e2181.
91. Choulis NH. Miscellaneous drugs, materials, medical devices, and techniques. *Side Effects of Drugs Annual*. **2014**, 35(49):899–924.
92. Di Michele A, Pérez Gutiérrez CL, *et al.* Formulation and characterization of sustainable bioadhesive films for wound treatment based on barley β -glucan extract obtained using the high power ultrasonic technique. *Int J Pharm*. **2023**, 638:e122925.
93. Majtan J, Jesenak M. β -Glucans: Multi-Functional Modulator of Wound Healing. *Molecules*. **2018**, 23(4):e806.
94. Du B, Bian Z, *et al.* Skin health promotion effects of natural beta-glucan derived from cereals and microorganisms: a review. *Phytother Res*. **2014**, 28(2):159–166.
95. 20+ Free Hordeum Vulgare & Barley Images – Pixabay. <https://pixabay.com/images/search/hordeum%2520vulgare/?cat=val>. Accessed on July 5, **2023**.
96. Du B, Meenu M, *et al.* A Concise Review on the Molecular Structure and Function Relationship of β -Glucan. *Int J Mol Sci*. **2019**, 20(16):e4032.
97. Trombino S, Servidio C, *et al.* CStrategies for Hyaluronic Acid-Based Hydrogel Design in Drug Delivery. *Pharmaceutics*. **2019**, 11(8):e407.
98. Burdick JA, Prestwich GD. Hyaluronic acid hydrogels for biomedical applications. *Adv Mater*. **2011**, 23(12):41-56.
99. Fallacara A, Baldini E, *et al.* Hyaluronic Acid in the Third Millennium. *Polymers*. **2018**, 10(7):e701.
100. Girish KS, Kemparaju K. The magic glue hyaluronan and its eraser hyaluronidase: a biological overview. *Life Sci*. **2007**, 80(21):1921–1943.
101. Snetkov P, Zakharova K, *et al.* Hyaluronic Acid: The Influence of Molecular Weight on Structural, Physical, Physico-Chemical, and Degradable Properties of Biopolymer. *Polymers*. **2020**, 12(8):e1800.

102. Wu X, Luan M, *et al.* The impact of different concentrations of hyaluronic acid on the pasting and microstructural properties of corn starch. *Int J Biol Macromol.* **2024**, 254:e127555.
103. Zerbinati N, Esposito C, *et al.* Chemical and mechanical characterization of hyaluronic acid hydrogel cross-linked with polyethylen glycol and its use in dermatology. *Dermatol Ther.* **2020**, 33(4):e13747.
104. Hossain Rakin R, Kumar H, *et al.* Tunable metacrylated hyaluronic acid-based hybrid bioinks for stereolithography 3D bioprinting. *Biofabrication.* **2021**, 13(4):e044109.
105. Hauptstein J, Forster L, *et al.* Bioink Platform Utilizing Dual-Stage Crosslinking of Hyaluronic Acid Tailored for Chondrogenic Differentiation of Mesenchymal Stromal Cells. *Macromol Biosci.* **2021**, 22(2):e2100331.
106. Petta D, D'Amora U, *et al.* Hyaluronic acid as a bioink for extrusion-based 3D printing. *Biofabrication.* **2020**, 12(3):e032001.
107. Pérez Gutiérrez CL, Cottone F, *et al.* The Optimization of Pressure-Assisted Microsyringe (PAM) 3D Printing Parameters for the Development of Sustainable Starch-Based Patches. *Polymers.* **2023**, 15(18):e3792.
108. Benito-Román Ó, Alonso E, *et al.* Ultrasound-assisted extraction of β -glucans from barley. *LWT - Food Sci Technol.* **2013**, 50(1):57–63.
109. Câmara GBM, Barbosa R de M, *et al.* Nanocomposite gels of poloxamine and Laponite for β -Lapachone release in anticancer therapy. *Eur J Pharm Sci.* **2021**, 163:e105861.
110. Valencia GA, Luciano CG, *et al.* Microstructure and physical properties of nano-biocomposite films based on cassava starch and laponite. *Int J Biol Macromol.* **2018**, 107:1576–1583.
111. Perotti GF, Tronto J, *et al.* Biopolymer-clay nanocomposites: Cassava starch and synthetic clay cast films. *J Braz Chem Soc.* **2014**, 25(2):320–30.
112. Díaz-Torres E, Rodríguez-Pombo L, *et al.* Integrating pressure sensor control into semi-solid extrusion 3D printing to optimize medicine manufacturing. *Int J Pharm X.* **2022**, 4:e100133.
113. Pagano C, Puglia D, *et al.* Development and Characterization of Xanthan Gum and Alginate Based Bioadhesive Film for Pycnogenol Topical Use in Wound Treatment. *Pharmaceutics.* **2021**, 13(3):e324.
114. Pagano C, Ceccarini MR, *et al.* Bioadhesive polymeric films based on usnic acid for burn wound treatment: Antibacterial and cytotoxicity studies. *Colloids Surf B: Biointerfaces.* **2019**, 178:488–499.

115. Ceccarini MR, Vannini S, *et al.* In Vitro Protective Effects of Lycium barbarum Berries Cultivated in Umbria (Italy) on Human Hepatocellular Carcinoma Cells. *Biomed Res Int.* **2016**, 2016:e7529521
116. Pagano C, Perioli L, *et al.* Folic acid-layered double hydroxides hybrids in skin formulations: Technological, photochemical and in vitro cytotoxicity on human keratinocytes and fibroblasts. *Appl Clay Sci.* **2019**, 168:382–395.
117. Hostanska K, Rostock M, *et al.* A homeopathic remedy from arnica, marigold, St. John's wort and comfrey accelerates in vitro wound scratch closure of NIH 3T3 fibroblasts. *BMC Complement Altern Med.* **2012**, 12:e100.
118. Pagano C, Luzi F, *et al.* Wound Dressing: Combination of Acacia Gum/PVP/Cyclic Dextrin in Bioadhesive Patches Loaded with Grape Seed Extract. *Pharmaceutics* **2022**, 14(3):e485.
119. Pérez Gutiérrez CL, Dominici F, *et al.* Thermoplastic corn starch reinforced with different additives for 3D printed application. In Proceeding of the XXXVIII Interregional Meeting of the Italian Chemical Society- Sections of Toscana, Umbria, Marche, and Abruzzo, Perugia Italy, 1-2 September **2022**.
120. Tagami T, Ito E, *et al.* 3D printing of gummy drug formulations composed of gelatin and an HPMC-based hydrogel for pediatric use. *Int J Pharm.* **2021**, 594:e120118.
121. Chatzitaki AT, Eleftheriadis G, *et al.* Fabrication of 3D-printed octreotide acetate-loaded oral solid dosage forms by means of semi-solid extrusion printing. *Int J Pharm.* **2023**, 632:e122569.
122. Kumar P, Rajak DK, *et al.* 3D Printing Technology for Biomedical Practice: A Review. *J Mater Eng Perform.* **2021**, 30(7):5342–5355.
123. Biggerstaff A, Fuller G, *et al.* Determining the yield stress of a Biopolymer-bound Soil Composite for extrusion-based 3D printing applications. *Constr Build Mater.* **2021**, 305:e124730.
124. Di Michele A, Fredi G, *et al.* Bioadhesive patches based on carboxymethyl cellulose/polyvinylpyrrolidone/bentonite composites and Soluplus® for skin administration of poorly soluble molecules. *Appl Clay Sci.* **2022**, 216:e106377.
125. Pathak TS, Kim JS, *et al.* Preparation of alginic acid and metal alginate from algae and their comparative study. *J Polym Environ.* **2008**, 16(3):198–204.
126. Olivas GI, Barbosa-Cánovas G V. Alginate–calcium films: Water vapor permeability and mechanical properties as affected by plasticizer and relative humidity. *LWT - Food Sci Technol.* **2008**, 41(2):359–366.
127. Ibrahim MIJ, Sapuan SM, *et al.* Potential of using multiscale corn husk fiber as reinforcing filler in cornstarch-based biocomposites. *Int J Biol Macromol.* **2019**, 139:596–604.

128. Lopez KM, Ravula S, *et al.* Hyaluronic Acid-Cellulose Composites as Patches for Minimizing Bacterial Infections. *ACS Omega*. **2020**, 5(8):4125–4132.
129. Khaliq T, Sohail M, *et al.* Hyaluronic acid/alginate-based biomimetic hydrogel membranes for accelerated diabetic wound repair. *Int J Pharm*. **2023**, 643:e123244.
130. Pang Q, Wu K, *et al.* A Polyaniline Nanoparticles Crosslinked Hydrogel with Excellent Photothermal Antibacterial and Mechanical Properties for Wound Dressing. *Macromol Biosci*. **2022**, 22(3):e2100386.
131. Greenspan L. Humidity Fixed Points of Binary Saturated Aqueous Solutions. *J Res Natl Bur Stand A Phys Chem*. **1977**, 81(1):89-96.
132. Hansen B, Jemec GBE. The mechanical properties of skin in osteogenesis imperfecta. *Arch Dermatol*. **2002**, 138(7):909–911.
133. Basiak E, Lenart A, *et al.* How Glycerol and Water Contents Affect the Structural and Functional Properties of Starch-Based Edible Films. *Polymers*. **2018**, 10(4):e412.
134. Eskandarinia A, Kefayat A, *et al.* Cornstarch-based wound dressing incorporated with hyaluronic acid and propolis: In vitro and in vivo studies. *Carbohydr Polym*. **2019**, 216:25–35.
135. Yang M, Shi J, *et al.* Effect of SiO₂, PVA and glycerol concentrations on chemical and mechanical properties of alginate-based films. *Int J Biol Macromol*. **2018**, 107:2686–94.
136. de S. M. de Freitas A, Rodrigues JS, *et al.* Improvements in thermal and mechanical properties of composites based on thermoplastic starch and Kraft Lignin. *Int J Biol Macromol*. **2021**, 184:863–873.
137. Sithole MN, Choonara YE, *et al.* Development of a Novel Polymeric Nanocomposite Complex for Drugs with Low Bioavailability. *AAPS PharmSciTech*. **2018**, 19(1):303–314.
138. Dumpa NR, Sarabu S, *et al.* Chronotherapeutic Drug Delivery of Ketoprofen and Ibuprofen for Improved Treatment of Early Morning Stiffness in Arthritis Using Hot-Melt Extrusion Technology. *AAPS Pharm Sci Tech*. **2018**, 19(6):2700–2709.
139. Goyanes A, Buanz ABM, *et al.* 3D printing of modified-release aminosaliclylate (4-ASA and 5-ASA) tablets. *Eur J Pharm Biopharm*. **2015**, 89:157–162.
140. Buyuksungur S, Endogan Tanir T, *et al.* 3D printed poly(ϵ -caprolactone) scaffolds modified with hydroxyapatite and poly(propylene fumarate) and their effects on the healing of rabbit femur defects. *Biomater Sci*. **2017**, 5(10):2144–2158.
141. Kim J, McBride S, *et al.* Rapid-prototyped PLGA/ β -TCP/hydroxyapatite nanocomposite scaffolds in a rabbit femoral defect model. *Biofabrication*. **2012**, 4(2):e025003.

142. Prata JC, da Costa JP, *et al.* Environmental exposure to microplastics: An overview on possible human health effects. *Sci Total Environ.* **2020**, 702:e134455.
143. Haryńska A, Janik H, *et al.* PLA-Potato Thermoplastic Starch Filament as a Sustainable Alternative to the Conventional PLA Filament: Processing, Characterization, and FFF 3D Printing. *ACS Sustain Chem Eng.* **2021**, 9(20):6923–38.
144. Larraza I, Vadillo J, *et al.* Cellulose and Graphene Based Polyurethane Nanocomposites for FDM 3D Printing: Filament Properties and Printability. *Polymers.* **2021**, 13(5):e839.
145. De S. M. de Freitas A, Da Silva APB, *et al.* Thermoplastic starch nanocomposites: sources, production and applications – a review. *J Biomater Sci Polym Ed.* **2022**, 33(7):900–945.
146. Jiang T, Duan Q, *et al.* Starch-based biodegradable materials: Challenges and opportunities. *Adv Ind Eng Polym Res.* **2020**, 3(1):8–18.
147. Wang B, Yu B, *et al.* An overview on plasticized biodegradable corn starch-based films: the physicochemical properties and gelatinization process. *Crit Rev Food Sci Nutr.* **2022**, 62(10):2569–2579.
148. Lara SC, Salcedo F. Gelatinization and retrogradation phenomena in starch/montmorillonite nanocomposites plasticized with different glycerol/water ratios. *Carbohydr Polym.* **2016**, 151:206–212.
149. Fishman ML, Coffin DR, *et al.* Extrusion of pectin/starch blends plasticized with glycerol. *Carbohydr Polym.* **2000**, 41(4):317–325.
150. Martin O, Schwach E, *et al.* Properties of Biodegradable Multilayer Films Based on Plasticized Wheat Starch. *Starch.* **2001**, 53(8):372-380.
151. Ghanbari A, Tabarsa T, *et al.* Preparation and characterization of thermoplastic starch and cellulose nanofibers as green nanocomposites: Extrusion processing. *Int J Biol Macromol.* **2018**, 112:442–447.
152. Sandri G, Faccendini A, *et al.* Halloysite- and Montmorillonite-Loaded Scaffolds as Enhancers of Chronic Wound Healing. *Pharm.* **2020**, 12(2):e179.
153. Park JH, Shin HJ, *et al.* Application of montmorillonite in -bentonite as a pharmaceutical excipient in drug delivery systems. *J Pharm Investig.* **2016**, 46(4):363–375.
154. Hossain SI, Kukushkina EA, *et al.* A Review on Montmorillonite-Based Nanoantimicrobials: State of the Art. *Nanomaterials (Basel).* **2023**, 13(5):e848.
155. Biddeci G, Spinelli G, *et al.* Nanomaterials: A Review about Halloysite Nanotubes, Properties, and Application in the Biological Field. *Int J Mol Sci.* **2022**, 23(19):e11518.

156. Biddeci G, Spinelli G, *et al.* Halloysite Nanotubes and Sepiolite for Health Applications. *Int J Mol Sci.* **2023**, 24(5):e4801
157. García-Villén F, Ruiz-Alonso S, *et al.* Clay Minerals as Bioink Ingredients for 3D Printing and 3D Bioprinting: Application in Tissue Engineering and Regenerative Medicine. *Pharm.* **2021**, 13(11):e1806.
158. Jiugao Y, Ning W, *et al.* The Effects of Citric Acid on the Properties of Thermoplastic Starch Plasticized by Glycerol. *Starch.* **2005**, 57(10):494–504.
159. Lulek J, Voelkel A, *et al.* Citric Acid: A Multifunctional Pharmaceutical Excipient. *Pharm.* **2022**, 14(5):e972.
160. Berovic M, Legisa M. Citric acid production. *Biotechnol Annu Rev.* **2007**, 13:303–343.
161. Ma X, Chang PR, *et al.* Properties of biodegradable citric acid-modified granular starch/thermoplastic pea starch composites. *Carbohydr Polym.* **2009**, 75(1):1–8.
162. Fernández Cervera M, Heinämäki J, *et al.* Determination of tackiness of chitosan film-coated pellets exploiting minimum fluidization velocity. *Int J Pharm.* **2004**, 281(1–2):119–27.
163. Butawan M, Benjamin RL, *et al.* Methylsulfonylmethane: Applications and Safety of a Novel Dietary Supplement. *Nutrients.* **2017**, 9(3):e290.
164. Young RJ, Lovell PA. Introduction to polymers. Third Edition. Edited by Taylor&Fracis Group. **2011**, 1–653.
165. Fu ZQ, Wang LJ, *et al.* The effect of partial gelatinization of corn starch on its retrogradation. *Carbohydr Polym.* **2013**, 97(2):512–517.
166. Balouiri M, Sadiki M, *et al.* Methods for in vitro evaluating antimicrobial activity: A review. *J Pharm Anal.* **2016**, 6(2):71–79.
167. Primavilla S, Pagano C, *et al.* Antibacterial Activity of Crocus sativus L. Petals Extracts against Foodborne Pathogenic and Spoilage Microorganisms, with a Special Focus on Clostridia. *Life.* **2022**, 13(1):e60.
168. Dumpa N, Butreddy A, *et al.* 3D printing in personalized drug delivery: An overview of hot-melt extrusion-based fused deposition modeling. *Int J Pharm.* **2021**, 600:e120501.
169. Alhijjaj M, Nasereddin J, *et al.* Impact of Processing Parameters on the Quality of Pharmaceutical Solid Dosage Forms Produced by Fused Deposition Modeling (FDM). *Pharm.* **2019**, 11(12):e633.
170. Ahmad MN, Ishak MR, *et al.* A Review of Natural Fiber-Based Filaments for 3D Printing: Filament Fabrication and Characterization. *Materials.* **2023**, 16(11):e4052.

171. Zdanowicz M, Sałasińska K. Characterization of Thermoplastic Starch Plasticized with Ternary Urea-Polyols Deep Eutectic Solvent with Two Selected Fillers: Microcrystalline Cellulose and Montmorillonite. *Polymers*. **2023**, 15(4):e972.
172. Ning W, Jiugao Y, *et al.* The influence of citric acid on the properties of thermoplastic starch/linear low-density polyethylene blends. *Carbohydr Polym*. **2007**, 67(3):446–453.
173. Effect of Magnesium Stearate On Processability and Properties of Thermoplastic Starch. AIChE Annual Meeting. Poster session: materials engineering & sciences. Hilton San Francisco Union Square, San Francisco, CA. November 3-8, **2013**.
174. Shi R, Zhang Z, *et al.* Characterization of citric acid/glycerol co-plasticized thermoplastic starch prepared by melt blending. *Carbohydr Polym*. **2007**, 69(4):748-755.
175. Ma X, Yu J. Formamide as the plasticizer for thermoplastic starch. *J Appl Polym Sci*. **2004**, 93(4):1769–1773.
176. Kizil R, Irudayaraj J, *et al.* Characterization of Irradiated Starches by Using FT-Raman and FTIR Spectroscopy. *J Agric Food Chem*. **2002**, 50(14):3912–3918.
177. Paluch M, Ostrowska J, *et al.* Structural and Thermal Properties of Starch Plasticized with Glycerol/Urea Mixture. *J Polym Environ*. **2022**, 30(2):728–740.
178. Diyana ZN, Jumaidin R, *et al.* Thermoplastic starch/beeswax blend: Characterization on thermal mechanical and moisture absorption properties. *Int J Biol Macromol*. **2021**, 190:224–232.
179. Hulleman SHD, Kalisvaart MG, *et al.* Origins of B-type crystallinity in glycerol-plasticised, compression-moulded potato starches. *Carbohydr Polym*. **1999**, 39(4):351–360.
180. Van Soest JJG, Hulleman SHD, *et al.* Crystallinity in starch bioplastics. *Ind Crops Prod*. **1996**, 5(1):11–22.
181. Combrzyński M, Oniszczyk T, *et al.* Physical Properties, Spectroscopic, Microscopic, X-ray, and Chemometric Analysis of Starch Films Enriched with Selected Functional Additives. *Materials*. **2021**, 14(10):e2673.
182. Chen X, Guo L, *et al.* Investigation of glycerol concentration on corn starch morphologies and gelatinization behaviours during heat treatment. *Carbohydr Polym*. **2017**, 176:56–64.
183. Willfahrt A, Steiner E, *et al.* Printable acid-modified corn starch as non-toxic, disposable hydrogel-polymer electrolyte in supercapacitors. *Appl Phys A Mater Sci Process*. **2019**, 125(7):1–10.
184. Handbook of Pharmaceutical Excipients Fifth Edition. Edited by Raymon C Rowe, Paul J Shwskey, *et al.* Published by the Pharmaceutical Press. **2006**.

185. Mutis González N, Pineda Gómez P, *et al.* Effect of the addition of potassium and magnesium ions on the thermal, pasting, and functional properties of plantain starch (*Musa paradisiaca*). *Int J Biol Macromol.* **2019**, 124:41–49.
186. Carazo E, Borrego-Sánchez A, *et al.* Assessment of halloysite nanotubes as vehicles of isoniazid. *Colloids Surf B: Biointerfaces.* **2017**, 160:337–344.
187. García-Villén F, Faccendini A, *et al.* Montmorillonite-norfloxacin nanocomposite intended for healing of infected wounds. *Int J Nanomedicine.* **2019**, 14:5051–5060.
188. Zhang M, Chen H. Development and characterization of starch-sodium alginate-montmorillonite biodegradable antibacterial films. *Int J Biol Macromol.* **2023**, 233:e123462.
189. González Seligra P, Medina Jaramillo C, *et al.* Data of thermal degradation and dynamic mechanical properties of starch–glycerol based films with citric acid as crosslinking agent. *Data Brief.* **2016**, 7:1331–4191.
190. Devi N, Dutta J. Development and in vitro characterization of chitosan/starch/halloysite nanotubes ternary nanocomposite films. *Int J Biol Macromol.* **2019**, 127:222–231.
191. Seligra PG, Medina Jaramillo C, *et al.* Biodegradable and non-retrogradable eco-films based on starch-glycerol with citric acid as crosslinking agent. *Carbohydr Polym.* **2016**, 138:66–74.
192. Das A, Uppaluri R, *et al.* Feasibility of poly-vinyl alcohol/starch/glycerol/citric acid composite films for wound dressing applications. *Int J Biol Macromol.* **2019**, 131:998-1007.
193. Desai DS, Rubitski BA, *et al.* Physical interactions of magnesium stearate with starch-derived disintegrants and their effects on capsule and tablet dissolution. *Int J Pharm.* **1993**, 91(2–3):217–26.
194. Bolhuis GK, Smallenbroek AJ, *et al.* Interaction of tablet disintegrants and magnesium stearate during mixing I: Effect on tablet disintegration. *J Pharm Sci.* **1981**, 70(12):1328–1330.
195. Grozdanova T, Trusheva B, *et al.* Extracts of medicinal plants with natural deep eutectic solvents: enhanced antimicrobial activity and low genotoxicity. *BMC Chem.* **2020**, 14(1):e73.
196. Sabah JR, Thippareddi H, *et al.* Use of Organic Acids for the Control of *Clostridium perfringens* in Cooked Vacuum-Packaged Restructured Roast Beef during an Alternative Cooling Procedure. *J Food Prot.* **2003**, 66(8):1408–1412.
197. Boukraâ L, Bouchegrane S. Additive action of honey and starch against *Candida albicans* and *Aspergillus niger*. *Rev Iberoam Micol.* **2007**, 24(4):309–311.

198. Ni Z, Shi J, *et al.* FDM 3D Printing and Soil-Burial-Degradation Behaviors of Residue of Astragalus Particles/Thermoplastic Starch/Poly(lactic acid) Biocomposites. *Polymers*. **2023**, 15(10):e2382.
199. Acierno D, Patti A. Fused Deposition Modelling (FDM) of Thermoplastic-Based Filaments: Process and Rheological Properties—An Overview. *Materials*. **2023**, 16(24):e7664.

Acknowledgments

I would like to thank the people who were by my side from the beginning, those I met along the way, and those who joined me at the end. First, I would like to thank my tutors, Proff. Luana Perioli and César Antonio Viseras for giving me this opportunity. To my research group at the University of Perugia, among them, Prof. Cinzia Pagano for her support during the thesis, Dott. Franco Dominici for teaching me so much about materials and for welcoming me from the first moment with so much affection, Proff. Debora Puglia and Francesca Luzi for their great professionalism and approach, Prof. Francesco Cottone and Alessandro Di Michele for their enthusiasm to teach me, and Dott. Maria Rachele Ceccarini and Sara Primavilla for their good work. To my department at the University of Granada, to Proff. Raquel de Melo Barbosa, Carola Aguzzi, and my colleague Tomas for giving me the best advice and listening to us in the most critical moments.

I am grateful to my family, who was always there, to my mother, who supported me in every moment of weakness, to my father for trusting me from the first moment, to my sisters Ana and Marta, how lucky to have them and that they never let go of my hand, to my grandmother Carmela, my psychologist and who gives the best advice in the world. To Alejandra and Alma for being light rays on this road. To those who left us but are still present in every step of my life, thank you, Carlos, Lolo, Ina and Pepe. To my other sisters Miriam and Teresa, I am so proud to have you in my life. To my friends from Fuente Vaqueros, those who are always there to celebrate any occasion, for every laugh. To my colleagues in Perugia, especially to Matteo, for being such an incredible person, to Paulina for the endless talks about anything, to Pilar and Javier for helping and supporting me, to Elena, Rossella and Jacopo my thesis students with whom we could learn and grow together professionally, to Elisapeç, Michela and Nicoleta for being more than those coworkers and being able to have fun outside the lab. Grateful to the beautiful family we formed in Perugia, especially to Iurie, my Moldavian friend, my great support in my day-to-day life, Musetta for being so crazy and having that overwhelming personality, very grateful to share this way with you, Simeng for that love-hate of my *chinito* that led us to be great friends, you are a character of those who should be close, and the last incorporation Gianmarco, what a great discovery. To the Erasmus friends of the first year in Perugia, especially to Irene for continuing to build this so beautiful thing that Perugia gave us, Blanca, and her wonderful hippie world in which she lives, and Pablo and Andres to all those people who made my first year incredible. To my roommates Martina and Elena, who made an apartment a home, and of course, to the latest addition Gessica. Grateful to the beautiful city that I had to live, to the most beautiful street of all *Corso Garibaldi, 53*, to the *Fortebraccio* bar and its people, to *Via della Viola* that hid magic in every corner, to *Piazza IV Novembre*, to *Olympic* gym with the best boxing friends, Michi, Carmela and Viola.

To finish I would like to say that it was a very hard experience, which pushed me to the limit on many occasions and in many of them I wanted to give up on many of them, but I think it was worth it thanks in part to all the wonderful people I met and all that I learned.